Structure and dynamics of hydrogen-bonded liquids

a study of supra-molecular structures and crystallisation

Jensen, Mikkel Hartmann

Publication date:
2016

Document Version
Publisher's PDF, also known as Version of record

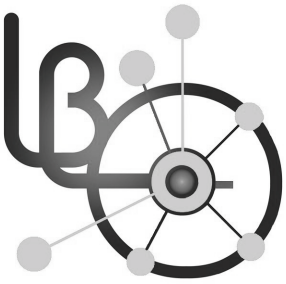

Structure and Dynamics of Hydrogen-Bonded Liquids

A Study of Supra-Molecular Structures and Crystallisation

Author:
Mikkel Hartmann Jensen

Supervisors:
Kristine Niss
Tina Hecksher
Christiane Alba-Simionesco

Department of Science and Environment
IMFUFA
Roskilde University

Abstract

This PhD thesis deals with the relastionship between structure and dynamics of hydrogen-bonded liquids, focusing on the effect of crystallisation on the dynamics, as well as the dynamics of supra-molecular hydrogen-bonded structures, that are believed to exist in these liquids. n-butanol and a series of glycerol-water mixtures were used, because they are hydrogen-bonded and can crystallise slowly, if the right temperature protocol is followed.

Two different sample cells were used to study the crystallisation of n-butanol with dielectric spectroscopy. The dielectric spectrum changed differently during crystallisation for the two cells. By modelling the Maxwell-Wagner effect, the differences could be explained by the sample cells giving rise to different morphologies of the crystal growth.

Neutron diffraction and small-angle scattering were used to study the proposed liquid-liquid transition in a glycerol-water mixture. The water in the mixture crystallised and no signs of a liquid-liquid transition were seen.

The dynamics of n-butanol was studied in the 120 K to 280 K range, using dielectric spectroscopy and neutron spin eco. The fitting procedure commonly used when analysing results from dielectric spectroscopy was shown to deliver unreliable results above 195 K for n-butanol.

Shear mechanical spectroscopy on glycerol revealed a slow relaxation process, which disappears gradually when water is added. This suggests that the slow relaxation process is connected to the hydrogen-bonded network between the glycerol molecules.

The above results stresses the need for combining different techniques when studying the dynamics of hydrogen-bonded systems. This is especially the case when studying crystallisation, where experiments should be done simultaneously to avoid influences from different sample cells.

Resume

I denne PhD afhandling undersøges forholdet mellem struktur og dynamik af hydrogenbundne væsker, herunder krystalliserings påvirkning af væskens dynamik, samt dynamikken af supramoleklære hydrogenbundne strukturer, der formodes at eksistere i hydrogenbunde væsker. n-Butanol og en række glycerol-vand blandinger blev anvendt, da de er hydrogenbundne og kan krystallisere langsomt ved en særlig temperature protokol.

To forskellige prøveholdere blev anvendt til at studere krystalliseringen af n-butanol med dielektrisk spektroskopi. Det dielektriske spektrum ændres under krystalliseringsprocessen, på en måde, der var forskellig for de to prøveholdere. Ved at modellere Maxwell-Wagner effekten kunne forskellen forklares ved at prøveholderne giver anledning til krystalvækst med forskellig morfologi.

Ved brug af neutron diffraktion og småvinkelspredning til at studere den formodede væske-væske faseovergang i en glycerol-vand blanding, synes vandet i blanding at krystallisere. Der var ingen tegn på en væske-væske faseovergang.

Ved undersøgelse af dynamikken af n-butanol fra 120 K til 280 K blev dielektrisk spektroskopi kombineret med neutron spin echo. Resultaterne viser at den fitteprocedure, der alment anvendes til at analysere resultater fra dielektrisk spektroskopi, giver upålidelige resultater allerede omkring 195 K for n-butanol.

Ved shear mekanisk spektroskopi ses der i glycerol en langsom relaxationsprocess, der forsvinder gradvist, når vand tilsættes. Dette kan tyde på, at den langsomme relaxationsprocess er et resultat af et hydrogenbundent netværk mellem glycerol molekylerne.

Af ovenstående resultater kan det sammenfattes, at det er fordelagtigt at kombinere forskellige eksperimentelle teknikker, når dynamikken af hydrogenbundne væsker studeres. Dette er specielt tilfældet når dynamikken studeres under krystallisering, hvor eksperimenterne desuden bør udføres simultant, for at undgå indflydelse fra forskellige prøveholdere.

Foreword

My ambition for the PhD was to get a broad overview of the different neutron scattering techniques. In this I believe that I have succeeded. I have been to more than ten beam times, covering four different techniques (diffraction, small angle scattering, neutron spin echo – from both a spallation source and a reactor – and back scattering). But my broad focus is also partly because I like learning about new experimental techniques. However, this broad focus also means that I have not been able to study the details of the different experimental techniques as much as I would have liked. For this reason I do not consider myself an expert in any of the experimental techniques I have used in my thesis work.

The founding for my thesis was split equally between Roskilde University (RUC) in Denmark and Laboratoire Léon Brillouin (LLB) in France. For this reason I have spent half of my time at RUC and the other half in LLB, changing place every semester.

A few word about my writing style. I have chosen a informal way of writing because I believe it makes the thesis more readable. When I write "we" it can mean one of two things: Either it means that I am addressing the reader in which case "We" covers you and I. Or it means my supervisors and myself. An example of the first would be: "In the next section we will cover the transient chain model". An example of the latter is: "We tried to quench the sample outside the cryostat, but till it crystallised on cooling." I use "I" when describing some action I have done: "In fig. 1 I show the relaxation time as a function of temperature". I hope the distinctions will not cause confusion.

Finally I would like to thank the people and institutions who have made this thesis possible.

This includes all the beam-line scientists and technicians who made the beam-times possible: Florence Porcher and Xavier Guillou (G4.1 LLB); Stephane Longeville (MUSE, LLB); Anni Brület (PAXY, LLB); Bernhard Frick and Markus Appel (IN16B, ILL); Michael Ohl and Piotr A. Zolnierczuk (ORNL).

Then I would like to thank the people I have shared beam-time with: Frédéric Caupin, Dmitry Nikolaevich Voylov, Alexei P. Sokolov and Alexande Kisliuk.

I would also like to thank the people in the labs and workshops who have helped me with my work: Bukhard Annighöefer (LLB), Benoit Homatter (LLB), José Teixeira (LLB), Marianne Bombled (LLB), Preben Olsen (RUC), Ebbe Hyldahl Larsen (RUC), Torben Rasmussen (RUC), Per Jakobsen (RUC) and Bo Jakobsen (RUC).

The secretaries Aurore Verdier (LLB) and Mette C. Nielsen (RUC) for helping me navigate the bureaucracy.

My office mates Alejandro Sanz (RUC) and Nancy Linder (LLB) for the

excellent company.

The institutes who have been my basis for the three years: IMFUFA at RUC and LLB. This includes The Glass and Time group for discussions during the weekly meetings.

My supervisors Kristine Niss, Tina Hecksher and Christiane Alba-Simionesco for showing me around in the strange and frustrating world of experimental physics.

And last but not least my girlfriend, Lise, for putting up with my absence and keeping me sane throughout the three long years. I love you.

Contents

Part I

Background

1 | Introduction

1.1 Thesis aim and scope

This thesis deals with the relationship between structure and dynamics of hydrogen-bonded liquids. Two different aspects of this relationship are studied. The first aspect is crystallisation where the emergence of local structure in the liquid may influences the dynamics of the liquid state. The second aspect is the the dynamics of the hydrogen-bonded supra-molecular structures that are believed to form in the liquid state of hydrogen-bonded liquids.

To narrow down the scope of this thesis the focus is on n-butanol and a series of glycerol-water mixtures. n-butanol is a mono-hydroxyl alcohol. Many mono-hydroxyl alcohols show a low-frequency dielectric signal – the so-called Debye-process – which is believed to be connected to supra-molecular hydrogen-bonded structures in the liquids [15]. It also crystallises very slowly if quenched to temperature within 20-30 K of the glass transition temperature. Therefore it is a excellent candidate for studying both the dynamics of supra-molecular hydrogen-bonded structures as well as dynamics during crystallisation, since the slow crystallisation processes leaves plenty of time for measurements.

Glycerol-water mixtures have attracted a great deal of attention over the past couple of years. Glycerol is a poly-alcohol and the archetypical glass former. It has been the subject of considerable and long-standing scientific interest because of its glass forming ability[69]. Water is a prime example of a hydrogen-bonded liquid, with it's hydrogen bonded network giving rise to a series of anomalous behaviours. The motivation for studying glycerol-water mixtures ranges from industrial application, such as improving cryoprotectants, to fundamental science, such as uncovering new states of matter[56]. There is general consensus that the hydrogen-bonded network in glycerol plays a crucial role both for its dynamics and structure. The interaction of water with this network is likewise of great interest, both from a fundamental point of view, and in terms of understanding the mechanisms behind the antifreeze effect of glycerol. These mixture also crystallises slowly in the high glycerol concentration range, if the right temperature protocol is followed.

Thus, both n-butanol and the glycerol-water mixtures are well suited for studying dynamics during crystallisation as well as the dynamics of supra-molecular hydrogen-bonded structures.

Liquid-liquid transition have been suggested to exist in both n-butanol [44] and a glycerol-water mixtures (with a molar concentration of glycerol at 0.178) [43, 56, 81]. In a liquid-liquid transition the structure of the liquid changes. Thus, structure is at the heart of this debate. However, the liquid-liquid trans-

ition has been disputed for both n-Butanol [21, 30, 44, 73, 91] and the glycerol-water mixtures[64].

1.2 Thesis structure and reading guide

Chapters 2-3 introduce the background for understanding the experimental results presented in this thesis. Since half of the work presented here deals with crystallisation, the basic concepts of crystallisation will be introduced in chapter 2. Chapter 3 gives a brief introduction to the various experimental techniques used in the thesis work, with a special emphasis on dielectric spectroscopy and how the dielectric permittivity of inhomogeneous media, such as a liquid-solid mixture, can be modelled.

Chapters 4-7 present the analysis and interpretation of the experimental results.

Chapter 4 examines the crystallisation of n-butanol, focusing on the emergence of local structure and how it influence the dynamics of the system. This is done by studying the isothermal crystallisation of n-Butanol using dielectric spectroscopy and neutron scattering. The focus is on how the changes to the dielectric signal that are observed with dielectric spectroscopy during crystallisation should be understood. We propose that the observed changes can at least partially be explained by modelling the inhomogeneity of the liquid-solid mixtures, which lead to a Maxwell-Wagner interface polarisation effect. The chapter also contains preliminary results from simultaneous dielectric spectroscopy and neutron scattering, intended to test the Maxwell-Wagner polarisation model.

Chapter 5 deals with the crystallisation of a glycerol-water mixture as studied by neutron scattering. Diffraction and small-angle scattering are used to study the structural changes that take place in the sample during crystallisation. The work in this chapter was partly motivated by the proposed liquid-liquid transition.

Chapter 6 focuses on the dynamics of n-butanol from 120 K to 280 K, combining neutron spin echo and dielectric spectroscopy. The fitting procedure often used when analysing data from dielectric spectroscopy can become difficult to interpret in the high temperature range. This especially the case for n-butanol because the relaxation processes get close to the end of accessible the frequency-window. Dielectric spectroscopy and neutron spin echo compliment each other and makes it possible to evaluate the limits of this fitting procedure.

Chapter 7 focuses on the shear-mechanical properties of neat glycerol as well as glycerol-water mixtures. The shear-mechanical spectrum of neat glycerol exhibits a slow mode which gradually disappears when water is mixed in. The

results are compared with data from the literature to give a coherent picture of the experimental findings, which points towards the slow mode being a signature of the hydrogen-bonded network of the glycerol molecules.

Finally in chapter 8 I reflect on the thesis as a whole and suggest research projects for the future.

2 | Phase transitions

In this chapter I introduce the main concepts necessary for understanding my work on the crystallisation of n-butanol and the glycerol-water mixtures.

2.1 Introduction

I start by introducing the concept of a phase diagram for single component systems as well as mixtures. I then move on to the mechanisms driving phase transition in such systems. In sec. 2.4 I briefly outline some of the main results of classical nucleation theory with a focus on how this can help us plan the temperature protocols to use when studying crystallisation. For mixtures an extra layer of complication is added to the phase diagram, as fluctuations in concentrations may lead to demixion. Depending on the temperature and concentration of the mixture, the demixion may proceed by nucleation and growth or spinodal decomposition. Therefore the concept spinodal decomposition is introduced in sec. 2.6. The standard equation for analysing phase transition kinetics is introduced in sec. 2.5.

2.2 The phase diagram

This presentation follows [41]. Depending on the physical conditions a material can be in different phases, that is, depending on the temperature and pressure of the system it may be in the solid, liquid or gas state. This information is usually summarised in a phase diagram where the distinct phases are separated by lines as is show schematically in fig. 2.1. On the lines the phases coexist.

When moving from one region of the phase diagram to another the new phase will have a lower free energy than the old and therefore a phase transition will take place. The free energy is the Gibb's free energy, which is defined as:

$$G = U + PV - TS \tag{2.1}$$

Where U is the total energy of the system. P and V are pressure and volume and T and S are temperature and entropy. When a system is held at constant pressure and temperature the Gibb's free energy must be minimised. By definition, G will be zero when system is in phase equilibrium. If the Gibb's free energy difference between two phases is negative a phase transformation will occur. When discussing phase transitions is convenient to define *the chemical potential*, μ, as the Gibb's free energy per particle. If a phase transition is favoured $\Delta\mu$ will be negative. The chemical potential is sometimes referred to as

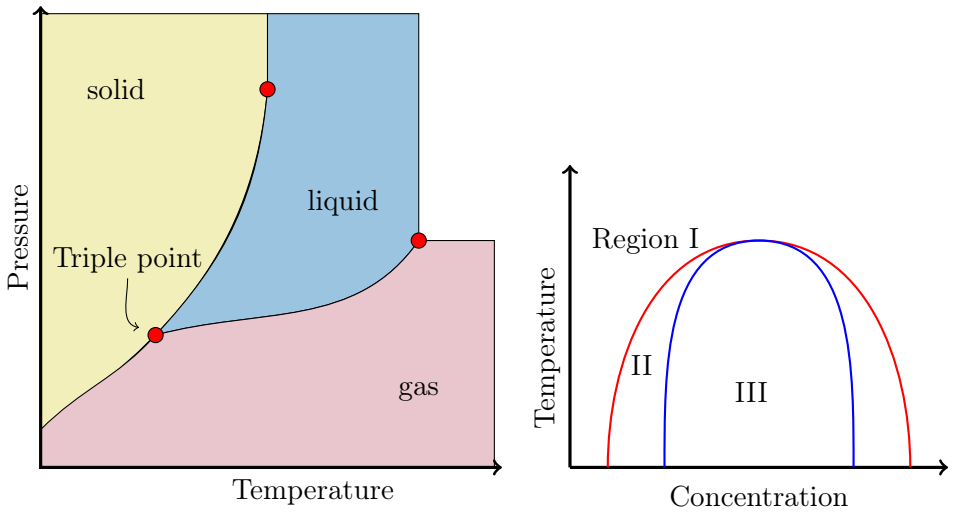

Figure 2.1: Left: The (T, P) phase diagram of a typical system. It contains three phases, two critical points and a triple point. Right: The concept of the spinodal and coexcistence line.

the thermodynamic driving force since this is what drives the transformation from one phase to another.

In the case of liquid mixtures the phase diagram become more complicated. In the right hand side of figure 2.1 I give an example of a concentration and temperature, (c,T), phase diagram. Depending on the concentration and temperature the mixture is either stable (region I), meta-stable (II) or completely unstable (III) with respect to fluctuations in the concentration. In the meta-stable region the transformation will proceed by nucleation and growth whereas the transformation will proceed by spinodal decomposition in region III.

2.3 The glass transition

A glass is an amorphous solid system, meaning that the atoms or molecules of the system are disordered, like in a liquid, but the system does not flow on timescales accessible to humans. Thus, a glass has the structure close to that of a liquid but the dynamics closer to that of a solid.

A glass is generally produced by cooling a liquid. At low cooling rates the system will begin to crystallise when it passes the melting temperature. If the liquid is cooled at a high cooling rate the liquid can be cooled below the melting temperature without crystallising, in which case the liquid is said to be super cooled, see fig. 2.2. As the liquid is being cooled the dynamics of the liquid will start to slow down because kinetic energy is being removed from the system.

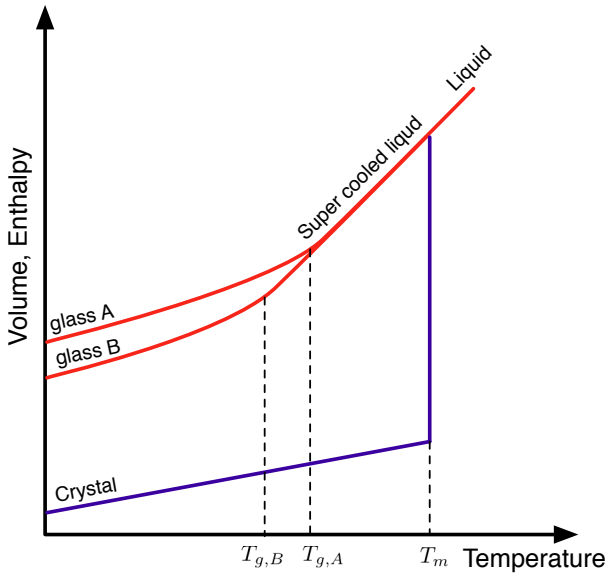

Figure 2.2: Illustration of the liquid to crystal and liquid to glass transition shown as volume or enthalpy as a function of temperature. At low cooling rates the system will begin to crystallise at T_m. If the liquid is cooled fast it will not crystallise but instead continue on the liquid state curve until it reaches a temperature T_g where it can no longer reach equilibrium and becomes a glass. The glass transition temperature depends not only on the liquid but also on the cooling rate.

Eventually, the dynamics will be so slow, that the system is no longer able to equilibrate to the temperature changes. When this happens, the system is said to be in the glassy state. The temperature where this happens is called the glass transition temperature, T_g. The exact value of T_g depends on the cooling rate. So the glass is not an equilibrium state, even though it may be extremely stable. The crystal is the eventual inevitable fate of all super cooled liquids and glasses.

2.4 Phase transitions: Classical nucleation theory

This section introduces the classical theory for describing how the new phase forms from the old – classical nucleation theory. For convenience, I will focus on the transition from liquid to solid, commonly known as crystallisation, but the results are general. I will follow the presentation given in [41].

In classical nucleation theory, crystallisation is treated as a two stage processes: The stage of nucleation and the stage of growth. The general idea is the following: Since the new phase has a lower Gibb's free energy than the original phase, it is energetically favourably to be in the new face. However, the form-

ation of a cluster comes at the cost of surface tension at the interface between the cluster and the remaining liquid. If we assume that the cluster is spherical, then the energy gained by having the cluster of the new phase depends on the volume of the cluster (as r^3) while the surface tension depends on the area (r^2). Thus, when some critical radius r^* is reached it will be energetically favourable for the cluster to grow, and therefore it will tend to do so. Below this critical size the cluster will tend to dissolve. This competition between the chemical driving force and the cost of added surface tension is summarised in fig. 2.3.

Small clusters of atoms or molecules arise spontaneously from density fluctuations. The work required to form a cluster of size n is given by:

$$W(n) = \sigma A + n\Delta\mu \tag{2.2}$$

Where $\Delta\mu$ is the difference in chemical potential between the two phases. It is negative. n is the number of molecules forming the cluster and σ is the surface free energy, that is, the energy required to produce more surface. Using the number density of the molecules, $\bar{n}$, we can express $n = \bar{n}V$. Assuming a spherical cluster eq. (2.2) can be specified further:

$$W(r) = 4\pi r^2\sigma + \frac{4\pi r^3\bar{n}}{3}\Delta\mu \tag{2.3}$$

This expression will have a maximum, which is the work, W^*, required to form a cluster of the critical size (radius r^*). The critical cluster radius can be found by finding the extremum or eq. 2.3:

$$\frac{\delta\Delta W}{dr} = 8\pi\sigma r + 4\Delta\mu\bar{n}r^2 = 0 \Rightarrow \tag{2.4}$$

$$r^* = \frac{-2\sigma}{\Delta\mu\bar{n}} \tag{2.5}$$

Remember that $\Delta\mu$ is negative. r^* depends on σ and $\Delta\mu$. Generally $\Delta\mu$ depends on pressure and temperature, so one can make the critical nucleus radius small by changing temperature and pressure.

Using the critical radius we can in turn calculate the total amount of work needed to reach the critical size:

$$W(r^*) = \frac{16\pi}{3}\frac{\sigma^3}{|\Delta\mu\bar{n}|^2} \tag{2.6}$$

Below r^* the cluster will, on average, shrink while above r^* the cluster will, on average, grow. Once the cluster has reached a radius of r^* the growth of the cluster is no longer limited by nucleation but other physical limitations such as diffusion from the surrounding medium.

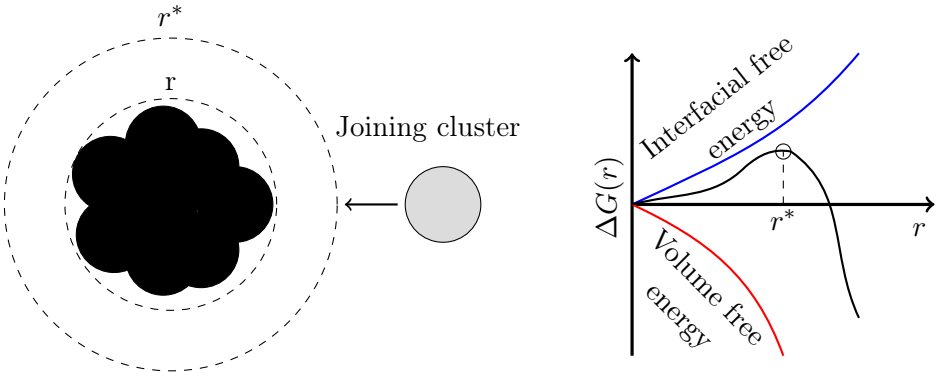

Figure 2.3: Schematic drawing of classical nucleation theory. The grey atom will join the cluster since the cluster has a lower $\Delta\mu$ but this comes at the cast of an increased surface tension for the cluster. The energy gained by having the bulk of the new phase goes as r^3 whereas the cost of interface foes at r^2, so $\Delta G(r)$ must go through a maximum. This idea is sketched in the graph on the right where the competition between interfacial free energy and volume free energy leads to a maximum. Clusters with a radius that exceeds r^* will tend to grow.

I show this result because it summarises the key idea of nucleation and growth as a competition between the chemical driving force and the impeding cost of surface. It also has practical implications in so far as nucleation is a necessary step for crystallisation – you can avoid crystallisation by avoiding the formation of critical nuclei in your sample.

In the end classical nucleation theory boils down to two rates: the nucleation rate, I, and the growth rate, U. The nucleation rate is taken to be proportional to the Boltzmann weighted probabilities of have critical fluctuations[41]:

$$I = A_0 \exp\left(-\frac{W(r^*)}{k_B T}\right), \tag{2.7}$$

where k_B is Boltzmann's constant and A_0 is a pre-factor that contains kinetic factors that describe the rate of atoms joining the cluster. The crystal growth rate is given by [72]:

$$U = a_0 \nu \exp\left(\frac{-\Delta E}{kT}\right)\left(1 - \exp\left[\frac{\Delta G}{kT}\right]\right), \tag{2.8}$$

where a_0 is the interatomic separation distance, ν is the vibrational frequency, and ΔE is the kinetic driving force and ΔG thermodynamic driving force, as earlier.

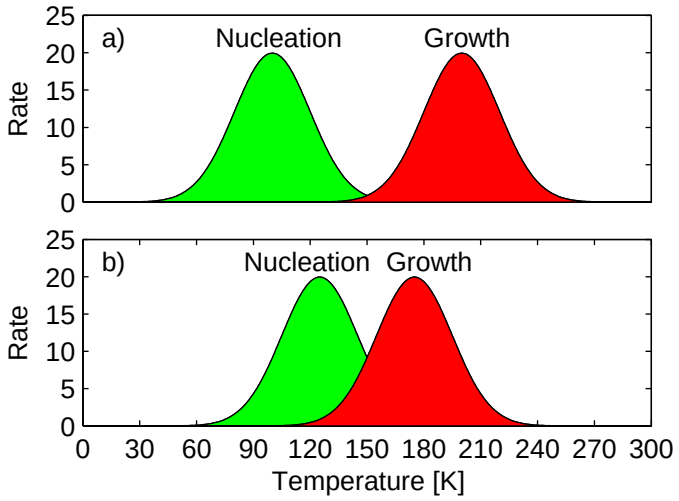

Figure 2.4: Schematic drawing of nucleation and growth rate. The separation between the nucleation region and growth region controls how easily the sample crystallises during cooling or heating

Both the nucleation and growth rate depend on the temperature and the separation in temperature of the maximal nucleation and growth rate can help us understand why some systems crystallise easily during cooling while other crystallise mainly on heating. To exemplify this fig. 2.4 show a schematic drawing of two scenarios. Imagine a liquid cooled from 300 K down to 70 K and heated back up to 300 K. In a) the nucleation and growth regions are well separated which means that crystallisation is unlikely to take place upon cooling, since no crystal nuclei are available in the growth region. However, upon heating the nuclei will have had time to form and they will grow when the growth region is entered. In b) the nucleation and growth regions overlap and crystallisation will be able to take place upon cooling, as the nuclei can form and grow at the same temperature. This means that in scenario a) a slow cooling will not lead to crystallisation while in case b) a quench would be necessary to avoid crystallisation on cooling. In both scenarios the exact temperature protocol is important since how long one spends in the nucleation or growth regions dictates what will happen. This is why we take great care to use the same temperature protocol when studying crystallisation kinetics.

2.5 Transformation kinetics of nucleation and growth

A common way of analysing phase transition kinetics is by using the Avrami equation first put forward in the late 1930s and early 1940s [6–8]. The equation related the degree of crystallinity, X_c, to the crystallisation rate, k, and the

Avrami parameter, n, that represents the morphology of the crystal growth as well as some circumstantial information:

$$X_c(t) = 1 - \exp\left[-kt^n\right] \tag{2.9}$$

This is the original version proposed by Avrami, but another commonly used version introduced a characteristic crystallisation time and an induction time [9]:

$$X_c(t) = 1 - \exp\left(-\left[\frac{t - t_0}{t_c}\right]^n\right) \tag{2.10}$$

Here t_0 is the induction time, t_c is the characteristic crystallization time and n is again the Avrami parameter. In figure 2.5 I show two examples of equation (2.10) and (4.6).

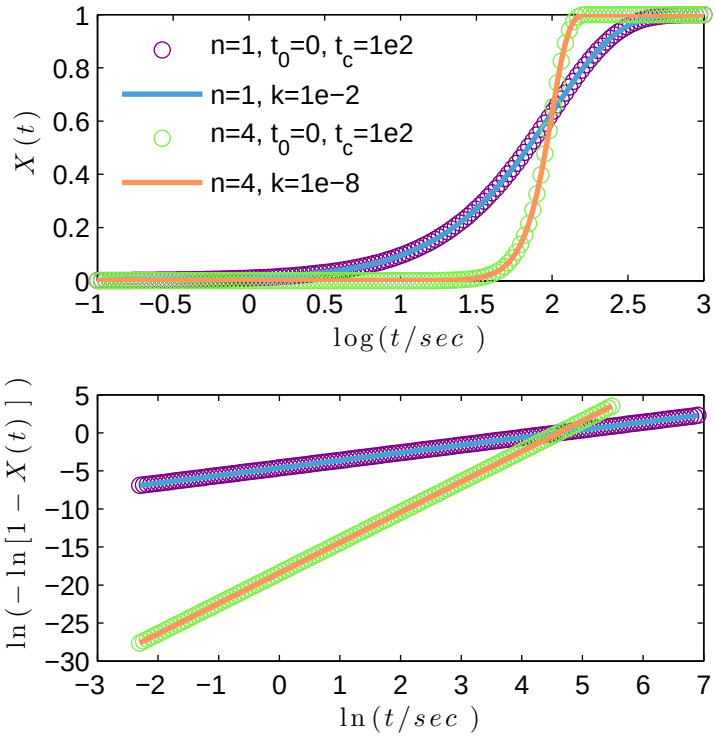

Figure 2.5: Comparing eq. (4.6) to (2.10) and showing alternative ways of estimating n.

The Avrami parameter can be split into two contributing factors: the dimensionality of the growth, d, and nuclei availability r:

$$n = d + r \tag{2.11}$$

d is between 1 and 3, depending on how many dimension the crystals grows in. r is 1 if nucleation is constant during crystallisation or 0 if nucleation stops as soon as the crystallisation starts. Thinking back to the two scenarios proposed in the previous section this would mean that n could at most be 3 in scenario a), since no nucleation takes place in the growth region, while it could reach 4 in scenario b). But eq. (2.11) also show the inherent problem with using the Avrami parameter to infer the dimensionality of the crystal growth: unless you know r there is no way of tell the exact dimensionality of the growth. n is usually established by fitting eq. (4.6) or (2.10); or by plotting $\ln(-\ln[1-X(t)])$ vs. $ln(t)$ as shown in fig. 2.5.

2.6 Phase transition: Spinodal decomposition

When working with mixtures of liquids the phase transformation can become more complicated since demixion can take place.

The spinodal is the line in the (c,T) phase diagram at which the nucleation barrier vanishes and the rate of generation of the new phase is only limited by the kinetics of growth of its clusters. The spinodal is defined by the condition that the second derivative of Gibbs free energy with respect to concentration is zero [27]. This defines the limit of local stability against fluctuations. For compositions within the spinodal region, infinitesimally small fluctuations in concentration will lead to phase separation via spinodal decomposition.

In spinodal decomposition an (infinitely) small fluctuation in the concentration will lead to a transformation of the entire sample. Whereas, in nucleation and growth the initial step – the formation of the nuclei – results from a large fluctuation, since the nuclei has to reach the critical size, but the extent is small, since the change is only local initially. This is sometime summarised as saying that spinodal decomposition is small in degree but large in extent where as nucleation is large in degree but small in extent.[27, 41]

2.7 Summary

In this chapter I have introduced two mechanism that drive phase transitions, as well as the standard theoretical framework for discussion the kinetics of such transitions. Classical nucleation theory treats crystallisation as a two tage transformation process: nucleation and growth. Nucleation in controlled by the competition between free energy and surface energy. For mixtures of liquids the phase diagram becomes more complicated as some temperature and concentration ranges will lead to an demixing of the liquids via spinodal decomposition. The differences and similarities between nucleation and growth and spinodal decomposition were discussed. The limitations of using the Avrami equation to

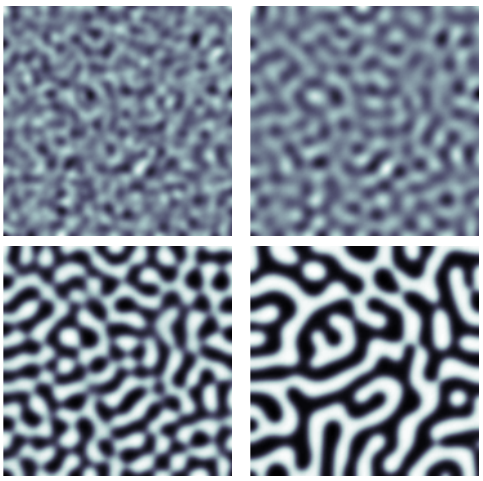

Figure 2.6: A simulation of a spinodal decomposition process. Two liquids unmix to form two domains of liquid one and liquid two. The images were created using the MatLab script downloadable at: `https://www.math.utah.edu/~eyre/computing/matlab-intro/ch.txt`

get information about the morphology of the growing crystal was discussed as well.

3 | Experimental techniques

In this chapter I give a brief introduction to the experimental techniques used to produce the results presented in this thesis. The techniques covered are: Dielectric spectroscopy, shear-mechanical spectroscopy and neutron scattering. Within neutron scatter I cover techniques for studying structure (diffraction and small-angle scattering) and dynamics (quasi-elastic neutron scattering and neutron-spin-echo).

3.1 Introduction

Since this chapter is quite long, I will start it off with a quick overview. The first method covered is dielectric spectroscopy. This is followed by a section on the dielectric properties of in-homogenous materials, since this is relevant when studying liquids during crystallisation. The next technique covered is shear-mechanical spectroscopy. The final technique – neutron scattering – is divided into four subsections, each covering different neutron scattering techniques.

3.2 Dielectric spectroscopy

Dielectric spectroscopy measurements gives access to the complex dielectric permittivity ϵ. The aim of this section is to introduce the main physical concepts that allows one to connect ϵ to dynamics of the molecules in the sample. The presentation vaguely follows [42].

When an electric field is applied over a material, the material becomes polarised. This polarisation does not happen instantaneously, but as a response to the electric field. The time dependent polarisation is then given by[42]:

$$\mathbf{P}(t) = \mathbf{P}_\infty + \epsilon_0 \int_{-\infty}^{t} \epsilon(t-t') \frac{\mathbf{E}(t')}{dt'} dt'. \tag{3.1}$$

where $\mathbf{P}_\infty$ covers all contributions arising from induced polarisation, such as the redistribution of the electrons in the atom or molecules. ϵ_0 is the the dielectric permittivity of vacuum, and $\mathbf{E}$ is the electric field being applied over the material.

If the electric field being applied is oscillatory, that is, $\mathbf{E}(t,\omega) = \mathbf{E}_0 \exp(-i\omega t)$, where ω is the angular frequency, then the time-dependent polarisation becomes[42]:

$$\mathbf{P}(t) = \epsilon_0 \left(\epsilon(\omega) - 1\right) \mathbf{E}(t) \tag{3.2}$$

The polarisation stems from two different processes: One is the redistribution of the electrons in the atom or molecules, called the *induced polarisation*. The other process is the reorientation of the permanent dipoles, called *rotational polarisation*. The rotational polarisation arises from the dipole changing its direction according to the direction of the external field. Dielectric spectroscopy probes the dynamics of the system by rotating the permanent dipoles with an oscillating electric field.

3.2.1 Practical considerations

In dielectric spectroscopy $\mathbf{P}$ is not measured directly. The sample is put inside a capacitor and then the complex capacitance, C, is measured. If it is a parallel plate capacitor, then the capacitance will be given by:

$$C(\omega) = \frac{\epsilon_0 \epsilon(\omega) A}{d}, \tag{3.3}$$

where A is the area of the capacitor places and d is the distance between the plates. This way, by measuring the capacitance of the filled and empty capacitor, the dielectric permittivity of the dielectric material can be obtained by dividing through with the capacitance of the empty capacitor, C_0:

$$\epsilon(\omega) = \frac{C(\omega)}{C_0} \tag{3.4}$$

In summary: It is possible to use a material's dielectric response to an external electric field to gain information about the dynamics of the permanent dipoles. In this section we have focused on going from a macroscopic property to information on a molecular level. It is important not to get too fixated on the molecular reorientation – interpreting any change in the measured complex capacitance as arising from changes to the bulk dynamics of the system. The next section examines what happens if the sample becomes heterogeneous on a macroscopic level, and that analysis treats the sample as a continuum rather than focusing on the dynamics.

3.3 Maxwell-Wagner Polarisation

3.3.1 Introduction

Maxwell-Wagner polarisation arises at interfaces between substances of different dielectric permittivity. One way to get this effect is to have a compound material made up of materials with different dielectric permittivities.

The goal of this section is to be able to calculate the dielectric permittivity of a compound, knowing the structure of the compound, as well as the dielectric permittivities of the materials making up the compound. Maxwell treated the

problem in the case of a inhomogeneous dielectric consisting of layers of materials having different dielectric permittivities. Later the case of a spherical domains embedded in a matrix was analysed by Wagner[90]. Later still the case of ellipsoidal domains was treated by Sillars[74]. Therefore, the effect is sometimes called Maxwell-Wagner-Sillars polarisation. However, I will continue calling it Maxwell-Wagner polarisation.

The effect is relevant to this thesis because of it's implications for dielectric measurements made on materials while they crystallise. As the crystallisation proceeds the sample will go from being a pure liquid to a mixture of liquid and crystallites. Since the crystalline form has a different dielectric permittivity than the liquid, the sample will be a compound material. Therefore a Maxwell-Wagner polarisation effect should arise.

It is important to point out that these models are macroscopic models. That is, the dynamics of the molecules is not considered in these models. The liquid is simply treated as a continuum of dielectric permittivity ϵ^*. The whole point of modelling the interface polarisation is, in some way, to account for the macroscopic effect. The end goal is to know how the dynamics of the liquid state influences the crystallisation process and vice versa. But before this is possible, it is necessary to know if and how the macroscopic changes influence the dielectric spectrum being measured. Otherwise one might attribute molecular (bulk) significance to an effect that is not molecular in nature.

Three crystallisation scenarios will be presented in this chapter. The first is heterogenous crystallisation from one or both of of the electrodes of the capacitor. This will be modelled by a layer of crystal growing from one of the capacitors. This model I call the *layer model*. The second is homogenous crystallisation in the bulk of the sample. This is modelled by a collection of spherical crystallites growing in the bulk of the sample. I call this model the *sphere model*. The third is a mixture of the two – a layer of crystallites growing from one of the capacitors while the bulk of the sample experiences homogenous crystallisation. The models are sketched in fig. 3.1.

3.3.2 The layer model

Consider a capacitor filled with two layers of material with dielectric permittivities ϵ_l and ϵ_c, as sketched in fig. 3.2. The height of the layers are d_l and d_c respectively with $d_l + d_c = 1$.

This scenario can be modelled as two capacitors in series, if one assumes a perfect interface between the materials and that there is no boundary effects

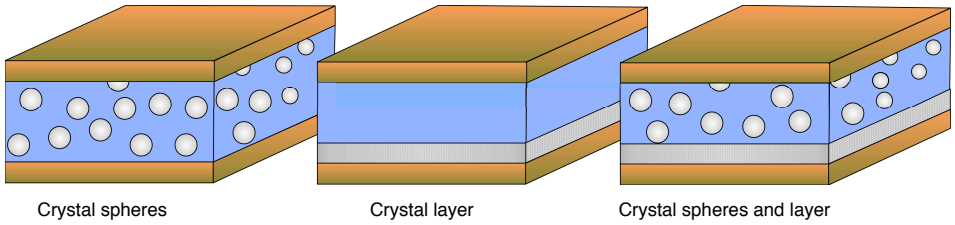

Figure 3.1: A schematic representation of three scenarios of heterogeneous dielectric material. The question to be answered in this chapter is the following: How does the dielectric permittivity of the entire sample depend on the specifics of the materials making up the compound and their arrangement.

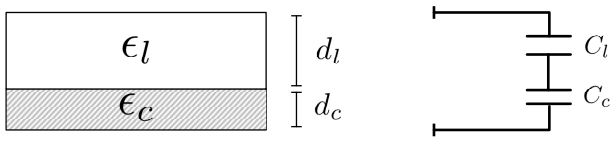

Figure 3.2: A sketch of a two layered compound material and the corresponding electric circuit.

from the edges of the capacitor. The capacitance of the compound then becomes:

$$\frac{1}{C_{comp}} = \frac{1}{C_l} + \frac{1}{C_c} = \frac{C_l + C_c}{C_l C_c}. \tag{3.5}$$

Here C_l and C_c are the capacitances corresponding to the two layers. Using the relationship between the capacitance of a parallel plate capacitor filled with a material of dielectric permittivity, ϵ, one can express the capacitance of the entire electric network in terms of the properties of the layered sample:

$$C_{comp} = \frac{\epsilon_0 \epsilon_{comp} A}{d_l + d_c} \quad , \quad C_l = \frac{\epsilon_0 \epsilon_l A}{d_l} \quad , \quad C_c = \frac{\epsilon_0 \epsilon_c A}{d_c}, \tag{3.6}$$

with A and d being the area of the area of the capacitor plates and the distance between them, respectively. Inverting equation (3.5) and inserting equation (3.6) yields:

$$\frac{\epsilon_{comp}}{d_l + d_c} = \frac{\dfrac{\epsilon_l \epsilon_c}{d_l d_c}}{\dfrac{\epsilon_l}{d_l} + \dfrac{\epsilon_c}{d_c}}. \tag{3.7}$$

By defining the relative height of the two layers as $\phi_{\text{layer}} \equiv d_c/(d_l + d_c)$, we can simplify the final expression:

$$\epsilon_{comp} = \frac{\epsilon_l \epsilon_c}{\phi_{\text{layer}} \epsilon_l + (1 - \phi_{\text{layer}}) \epsilon_c}. \tag{3.8}$$

It relates the dielectric permittivity of the compound material to the two dielectric permittivities and the volume fraction taken up by the layer.

Trying out the model

Assuming that the liquid has a single relaxation process described by a Cole-Cole function and that the crystal has a frequency independent dielectric permittivity, such that:

$$\epsilon_l = \epsilon_\infty + \frac{\Delta\epsilon}{1 + (i\omega\tau)^\beta} \quad , \quad \epsilon_c = 2 + 0.01i, \tag{3.9}$$

with $\Delta\epsilon = 20$, $\epsilon_\infty = 2$, $\beta = 1$, $\tau = 1/2\pi$ for the liquid. Using eq. (3.8) together with eq. (3.9) and $\phi = 0.1$ gives the red curve in fig. 3.3.

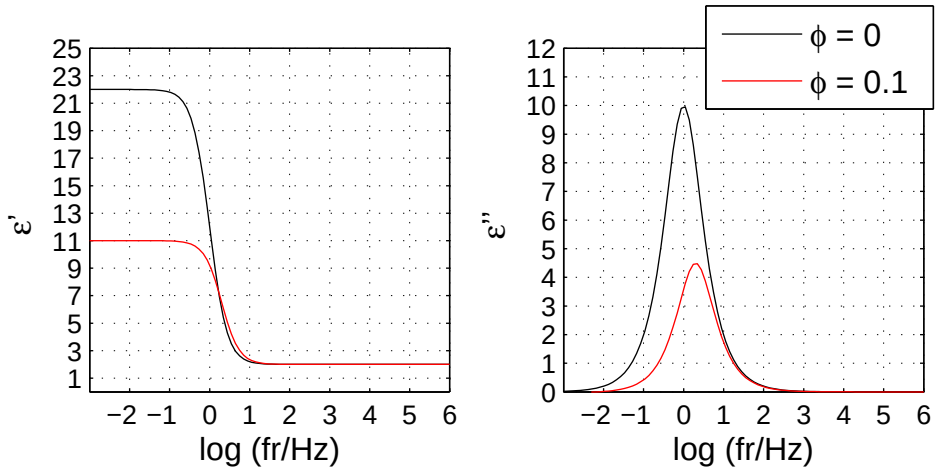

Figure 3.3: Using eq. (3.8) together with eq. (3.9) and the parameters describes below eq. (3.9) we see that having just 10% of the sample taken up by a crystal layer will dramatically reduce the strength of the signal, as well as shift the apparent relaxation time to a shorter time scale.

The effect of having just 10% of the capacitor filled with a layer gives rise to profound changes in the spectrum. The relaxation strength drops by approximately 50% and the relaxation time is shifted by half a decade.

3.3.3 Spheres imbedded in a matrix

The level of detail is higher in this sub-section because the information is not readily available. The presentation is loosely based on [90], but using modern notation.

The approach to the problem

The first step is to find the electric potential outside a sphere placed in a uniform electric field. The next step is to compare two scenarios. The first scenario is a collection of spheres of dielectric permittivity ϵ_c imbedded in an infinite medium of dielectric permittivity ϵ_l. The second scenario is a sphere of dielectric permittivity ϵ_{comp} imbedded in an infinite medium of dielectric permittivity ϵ_l. See fig. 3.4 for a sketch of the two scenarios. The trick is then to set the electric potentials far away from the spheres to be equal. This way one can express ϵ_{comp} in terms of ϵ_l and ϵ_c. This approach only works if each of the spheres in the first scenario are far enough from each other such that the electric field each sphere is exposed to is uniform, otherwise the expression for the electric potential becomes invalid. This is what is referred to as a mean-field approximation. Supposedly this approximation only works for volume fractions up to 20% [42], but I have not been able to find an argument to support this claim. Surely the mean-field approximation breaks down at soe point, but I do not know exactly when.

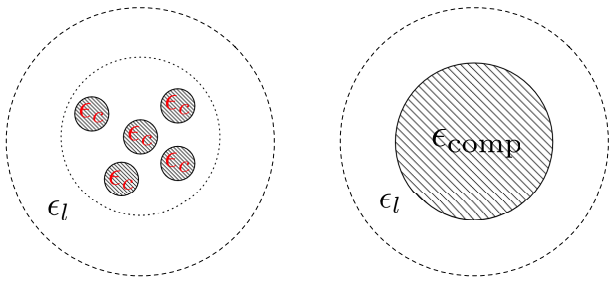

Figure 3.4: Schematic drawing of the two scenarios used in the approach. The electric potential far away from each scenario should be indistinguishable.

Equating the two scenarios

Consider a sphere of dielectric material of dielectric permittivity, ϵ_c, placed in an infinite dielectric material of dielectric permittivity, ϵ_l, with a uniform electric field. The potential outside the sphere will the be given by (see appendix A):

$$V_{out}(r,\theta) = \left(\frac{\epsilon_c - \epsilon_l}{\epsilon_c + 2\epsilon_l} \frac{R^3}{r^2} - r \right) E_0 \cos\theta, \tag{3.10}$$

where R is the radius of the sphere.

Far away from either of the scenarios, the electric potential should be indistinguishable, so we can set $V_{\text{out}}^{\text{sphere}} = V_{\text{out}}^{\text{comp}}$.

$$\left(\frac{\epsilon_c - \epsilon_l}{\epsilon_c + 2\epsilon_l} \frac{NR^3}{r^2} - r \right) E_0 \cos(\theta) = \left(\frac{\epsilon_c - \epsilon_l}{\epsilon_c + 2\epsilon_l} \frac{R_c^3}{r^2} - r \right) E_0 \cos(\theta) \tag{3.11}$$

By cancelling terms and defining the volume fraction taken up by the spheres to be $\phi_{\text{sphere}} \equiv NR^3/R_c^3$ we get:

$$\phi_{\text{sphere}} \left(\frac{\epsilon_c - \epsilon_l}{\epsilon_c + 2\epsilon_l} \right) = \frac{\epsilon_{\text{comp}} - \epsilon_l}{\epsilon_{\text{comp}} + 2\epsilon_l} \tag{3.12}$$

Finally rearranging gives:

$$\epsilon_{\text{comp}} = \epsilon_l \left(\frac{2\epsilon_l + \epsilon_c + 2\phi_{\text{sphere}}(\epsilon_c - \epsilon_l)}{2\epsilon_l + \epsilon_c - \phi_{\text{sphere}}(\epsilon_c - \epsilon_l)} \right), \tag{3.13}$$

relating the dielectric permittivity of of the compound material to the two dielectric permittivities and the volume fraction taken up by the spheres.

Trying out the model

Using the same example as in section 3.3.2 yields the results shown in fig. 3.5.

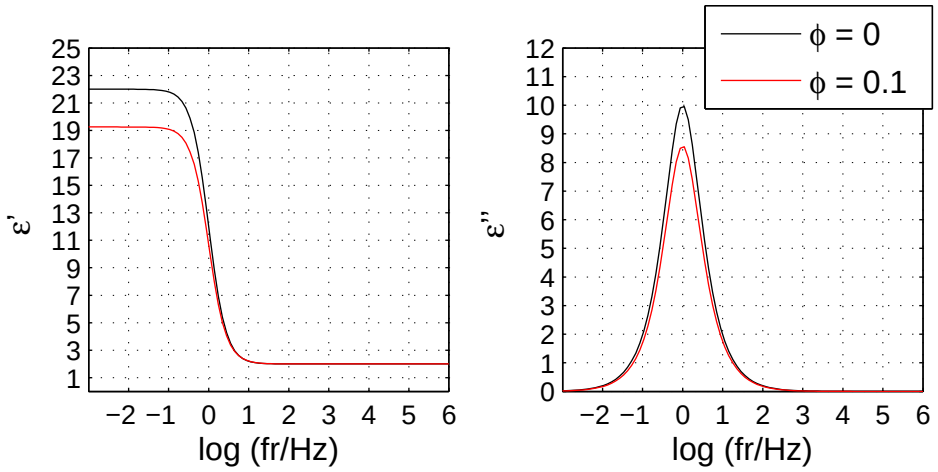

Figure 3.5: Using the same example as in section 3.3.2 we see only a minor effect compared to when we used the slab model.

The effect is less pronounced than in the case of the slab. The relaxation time doesn't change at all and the relaxation strength drops by roughly 10%.

3.3.4 Comparing the two models

Modelling a liquid with a Cole-Cole we have investigated the effect of filling this model liquid with crystallites. We have investigated two nucleation and growth scenarios: that of a layer growing from the capacitor plate and that of spherical crystallites growing in the liquid.

To check if the relaxation strength of the liquid is important for the changes to the apparent relaxation strength, $\Delta\epsilon(\phi)$, and relaxation time, $\tau(\phi)$, I have used the same scenario of a Cole-Cole liquid, but with different relaxation strengths ($\Delta\epsilon = 0.1, 1, 10,$ and 50 were used). The results of carrying out these calculations are shown in fig. 3.6.

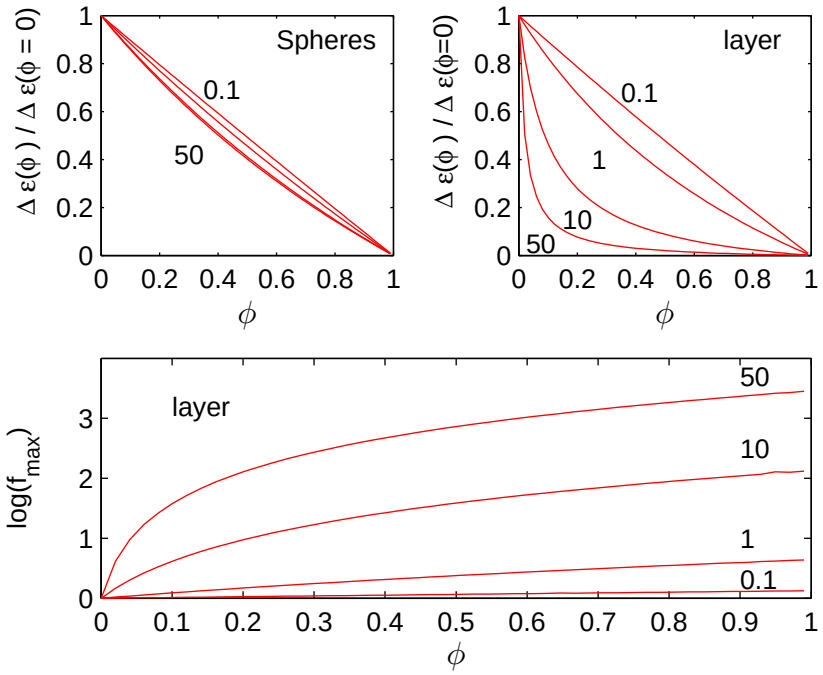

Figure 3.6: Top: Showing how the normalised relaxation strength depends on the volume fraction parameters, ϕ, in the two models. Bottom: The relaxation frequency as a function of ϕ for the slab model.

The two top panels show how the normalised relaxation strength varies as a function of ϕ. What we see is that, in both cases, the deviation from a straight line is increased by increasing the relaxation strength. But the deviation is much stronger for the slab model.

Defining the relaxation frequency, $f_{\max}$ as $f_{\max} \equiv 1/\tau_{\max}$ we can look at how the relaxation frequency changes as a function of ϕ depending on the relaxation

strength. Based on the example shown in fig. 3.5 it seems that the spherical model does not produce any changes to the apparent relaxation time, so they have been left out here. The bottom panel of fig. 3.6 shows that the magnitude of the change in the apparent relaxation time depends strongly on the relaxation strength of our model liquid.

These results already have implications for studying crystallisation with dielectric spectroscopy, since it tells us that the observed changes depend on the morphology of the crystal domains formed in the liquid. However, it is rather unlikely that the crystallisation process will be well described by either of the two models presented above. Therefore, I will present a combination of the two models in the next section.

3.3.5 The combined layer and spheres model

The next model is simply a combination of the two models already presented. However, the combination of the models as well as the application to crystallisation is a novel idea.

Imagine a scenario where we have a layered structure, but with spherical crystallites growing in the liquid layer. This can be modeled by combining the two model from section 3.3.2 and 3.3.3. Doing so brings four permittivities in play: 1) the liquid, ϵ_l, 2) the solid ϵ_c 3) the composite of the liquid with spherical crystallites, $\epsilon_{\text{spheres}}$; and 4) that of the entire compound, ϵ_{comp}. It also brings two volume fraction parameters. The first is the volume fraction taken up by the crystal layer ϕ_{layer}. The second is the volume fraction taken up by the spheres in the remaining liquid ϕ_{spheres}. Both volume fractions are between 0 and 1, but it is not the case that the total crystal volume, $\phi_{\text{cryst}} = \phi_{\text{layer}} + \phi_{\text{spheres}}$, but rather that $\phi_{\text{cryst}} = \phi_{\text{layer}} + (1 - \phi_{\text{layer}})\phi_{\text{spheres}}$.

The composite permittivity of the entire sample is given by eq. (4.2):

$$\epsilon_{\text{comp}} = \frac{\epsilon_{\text{spheres}}\epsilon_c}{\phi_{\text{layer}}\epsilon_{\text{spheres}} + (1 - \phi_{\text{layer}})\epsilon_c} \tag{3.14}$$

with $\epsilon_{\text{spheres}}$ defined by eq. (3.13) being given by:

$$\epsilon_{\text{spheres}} = \epsilon_l \left(\frac{2\epsilon_l + \epsilon_c + 2\phi(\epsilon_c + \epsilon_l)}{2\epsilon_l + \epsilon_c - \phi(\epsilon_c - \epsilon_l)} \right) \tag{3.15}$$

Even though four permittivities are in play, ϵ_l and ϵ_c can be measured and $\epsilon_{\text{spheres}}$ and ϵ_{comp} can be calculated leaving only the parameters ϕ_{layer} and ϕ_{spheres}.

Trying out the model

Using the same model liquid as in the previous sections, fig. 3.7 shows how the relaxation strength and relaxation time are affected by the parameters ϕ_{spheres} and ϕ_{layer}. The left panel shows relaxation strength $\Delta\epsilon(\phi_{\text{spheres}}, \phi_{\text{layer}})$, normalised to the initial value. The right panel shows the relaxation frequency $f_{\max}(\phi_{\text{spheres}}, \phi_{\text{layer}})$ on a log scale. Notice that the direction of the ϕ_{layer} and ϕ_{spheres} axes are different in the two panels.

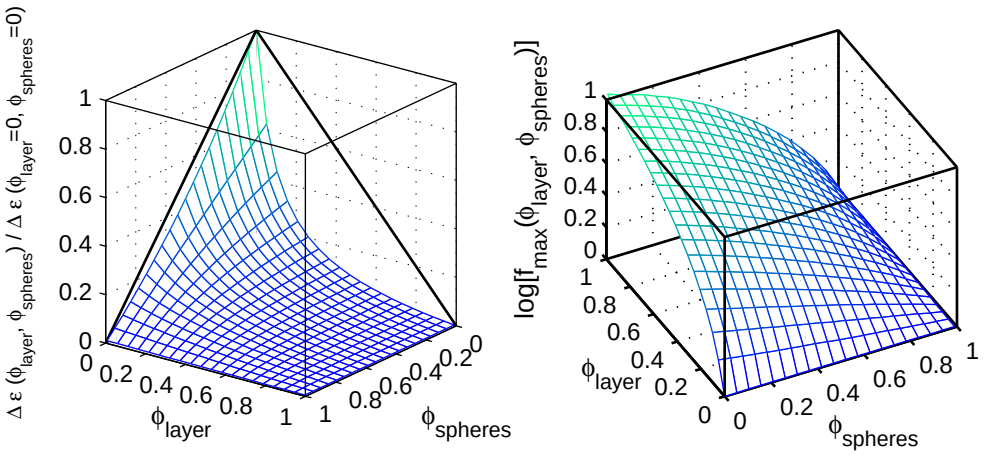

Figure 3.7: Showing how the normalised relaxation strength and relaxation frequency depends of on two volume fraction parameters.

Focusing first on the relaxation strength we can confirm that the edge cases work as expected, that is, keeping $\phi_{\text{layer}} = 0$ and varying ϕ_{spheres} follows quite closely $\Delta\epsilon(\phi_{\text{spheres}}, \phi_{\text{layer}} = 0)/\Delta\epsilon(\phi_{\text{spheres}} = 0, \phi_{\text{layer}} = 0) \approx 1 - \phi_{\text{spheres}}$. On the other hand, layer model deviates dramatically from this behaviour, that is, the relaxations strength decays much faster as a function of ϕ_{layer}. This was already shown in sections 3.3.2 and 3.3.3. But we see now that we can get some quite complicated behaviour out of the combined model.

Looking now a the relaxation frequency, we see that ϕ_{spheres} has no effect as long at $\phi_{\text{layer}} = 0$. However, for any other value of ϕ_{layer} and increase in ϕ_{spheres} will tend to push to relaxation frequency to higher frequencies.

3.3.6 Implications for studying crystallisation using dielectric spectroscopy

The models presented above have implication for what to expect when studying crystallisation with dielectric spectroscopy. In this section I will describe what I believe to be the main points to take away from the Maxwell-Wagner models

described here.

The relaxation strength of the liquid sample matters. A greater difference between the dielectric permittivity of the liquid and solid leads to a more drastic decrease in the relaxation strength during the crystallisation process.

The morphology of the crystal domains matters. This is important because the specifics of the sample cell may influence the morphology of the crystal domains formed during crystallisation. A cell that tends to start the crystallisation on the surface of the sample cell you give a different results than a cell that tends to crystallise from the bulk.

3.4 Shear mechanical spectroscopy

In shear mechanical spectroscopy one measures the complex shear modulus, G. G is a measure of how difficult is it to make a shear deformation of a substance and it is defined as the ratio between the shear stress and shear strain. At RUC $G(\omega)$ is measured using the piezoelectric shear modulus gauge (PSG) as described in [17].

The system I have studied during my Thesis work are viscoelastic. This means that their mechanical response to an external force will be viscous or elastic depending on the timescale being studied. If the system is characterised by a relaxation time τ then on timescales much shorter than τ the response will be elastic whereas on timescales much larger than τ the response will be viscous.

For viscoelastic substance the complex shear modulus can be related to the complex viscosity, assuming a harmonic stress and strain[59]:

$$\eta(\omega) = \frac{1}{i\omega} G(\omega), \tag{3.16}$$

which is the relation between the complex viscosity and complex shear modulus.

This method is used in this thesis because the dynamics of the system being studied should leave a signature in the frequency dependent shear moduli. For example, the Debye process in mono-alcohols as seen using dielectric spectroscopy has a counterpart in the shear modulus [29]. In chapter 7 I have used this technique to study the dynamics of glycerol-water mixtures.

3.5 Neutron scattering techniques

Neutron scattering can be used to study structure as well as dynamics. In this section I will introduce the main concepts necessary for understanding the work presented in the remainder of the thesis. I will start off by giving a brief introduction to neutron scattering. I will follow the presentation given in [46]. Then I will describe the specific neutron scattering techniques used in my thesis

work. This includes diffraction, small-angle scattering on the structural side as well as neutron spin echo and back scattering on the dynamic site.

Generally speaking, neutron scattering experiments measure the number of neutron scattering into a solid angle element $d\Omega$ with a an energy interval of $d(\hbar\omega)$. This is proportional to the double-differential scattering cross-section which reads[46]:

$$\frac{d^2\sigma}{d\Omega dE} = \frac{k}{k_0}\frac{\sigma}{4\pi}S(\mathbf{q},\omega) \tag{3.17}$$

Here k_0 and k are the wave number before and after the scattering event, respectively. The dynamic and structural properties of the sample are described by the dynamic structure factor $S(\mathbf{q},\omega)$. σ is the scattering length, defined as $\sigma \equiv 4\pi b^2$, where b is the scattering length of the nucleus. In real physical systems the atoms have different isotopes and spin, which lead to varying scattering lengths, so σ will vary from atom to atom randomly in the sample. This destroys part of the interference one would otherwise observe for a system where all nuclei had the same scatting length [46].

The the double-differential scattering cross-section can be separated into a coherent part and an incoherent part such that the double-differential cross-section reads[46]:

$$\frac{d^2\sigma}{d\Omega dE} = \frac{k}{k_0}\left[\frac{\sigma_{coh}}{4\pi}S_{coh}(\mathbf{q},\omega) + \frac{\sigma_{inc}}{4\pi}S_{inc}(\mathbf{q},\omega)\right] \tag{3.18}$$

where σ_{coh} and σ_{inc} are the coherent and incoherent scattering cross section respectively. The coherent part contains information about different atoms at different times – it contains information about *collectives* of atoms. The incoherent part contains information about the same atom at different times – it contains information about *individual* atoms.

One of the things that make neutron scattering useful is the fact that different atoms and isotopes have different scattering lengths. For example Hydrogen has a large incoherent scattering cross section, but the isotope ^2H (or Deuterium D) has a large coherent scattering cross section. This makes it possible to change weight between the two terms in eq. (3.18) by selective changing the Hydrogen in the sample to Deuterium.

The dynamic structure factor can be related to the intermediate scatting function, $I(\mathbf{q},t)$, through a temporal Fourier transform:

$$S(\mathbf{q},\omega) = \frac{1}{2\pi}\int_{-\infty}^{\infty} I(\mathbf{q},t)\exp\left(-i\omega t\right)dt. \tag{3.19}$$

The intermediate scatting function is what is measure in neutron spin echo, as will be explained in sec. 3.5.4. The intermediate scatting function is in turn connected to the time-dependent pair correlation function, $G(\mathbf{r}, t)$, through a spatial Fourier transform:

$$G(\mathbf{r}, t) = \frac{1}{(2\pi)^3} \int_{-\infty}^{\infty} I(\mathbf{q}, t) \exp\left(-i\mathbf{q} \cdot \mathbf{r}\right) d\mathbf{q}. \tag{3.20}$$

$G(\mathbf{r_i} - \mathbf{r_j}, t)$ is the conditional probability of finding an nuclie at a position $\mathbf{r_j}$ at time t, if this or another nuclie was at position $\mathbf{r_i}$, with distance $\mathbf{r} = \mathbf{r_j} - \mathbf{r_i}$ at previous time 0. The dynamic structure factor is the temporal and spatial Fourier transform of this correlation function. This is useful because it gives us a way of thinking about the functions.

If one is only interested in the structure of the sample one can integrate over all energies to get the static structure factor, $S(\mathbf{q})$:

$$S(\mathbf{q}) = \int_{-\infty}^{\infty} S(\mathbf{q}, \omega) d\omega = I(\mathbf{q}, t = 0) \tag{3.21}$$

Experimentally this is a lot easier, since you avoid having to keep track of the energies of the neutrons.

Depending on what you are interested in about your sample you will have different requirement about the range and resolution of $\mathbf{q}$ and ω. For this reason several different neutron scattering techniques have been developed. In this next four subsection I will briefly introduce the neutron scattering techniques used in this thesis, with a focus on the particular instruments used.

3.5.1 Diffraction

For lack of a better word I call neutron scatting that probes the local structure for diffraction. This is to distinguish it from other techniques that cover different q-ranges, such as small-angle scattering or wide-angle scattering. Diffraction covers roughly the $0.1 - 5$ Å^{-1} range. In this range we see the local structure of crystals and liquids of the systems studied in this thesis. Diffraction spectrometers comes in many varieties, depending on the needed $q-$range and resolution as well as neutron flux.

In our case we wanted to study the crystallisation of n-butanol. This meant that we would like to cover the $0.1 - 2$ Å^{-1} range with a high flux, since time is of the essence when studying crystallisation. We did not have high demands on the $q-$resolution since we were mostly interested in the over-all changes in the diffraction pattern when going from liquid to crystal. For this the instrument G 6.1 at LLB suited our needs. The results are presented in chapter 4.

3.5.2 Small-angle scattering

Small angle scattering requires a high $q-$resolution in the low $q-$range. Since small-angle scattering probes longer length scales than diffraction the community have come up with a formalism that incorporates this into the equations.

$$I(\mathbf{q}) = |F(\mathbf{q})|^2 S(\mathbf{q}) \tag{3.22}$$

Where $I(\mathbf{q})$ is the scattered intensity and $F(\mathbf{q}$ is the form factor. The form factor contains information about the structures in the sample on a lengths scale that is longer than the local structure contained in $S(\mathbf{q})$, typically probed by diffraction. The aim of small-angle scattering is usually to determine $F(\mathbf{q})$.

The instrument used for the work presented in this thesis was PAXY at LLB. It cover a q-range of $\approx 1-10^{-3}$ Å^{-1} range. When studying crystallisation, diffraction gives you information about the emergence of the lattice structure of the crystal while small-angle scattering gives you information about the shape of the crystal domains that form in the sample. We used this technique to study the crystallisation of a glycerol-water mixture. The results are presented in chapter 5.

3.5.3 Backscattering

With backscattering one measures $S(q, \omega)$. This technique generally covers low energies, corresponding to short relaxation times. The instrument used for the work presented in this was IN16B at ILL. The instrument covers the ΔE up to $30 \mu eV$.[28]

Measuring $S(q, \omega)$ in the entire energy range takes about three hours, depending on how much the sample scatters. This is too slow to study crystallisation in the temperature range we are interested in, but IN16B gives the possibility of measuring at a fixed ΔE, rather than doing a complete scan[28]. This way a measurement takes minutes rather than hours, allowing us to study crystallisation in real time. Of course this gives us much less information than a complete scan would.

This technique was used to study the crystallisation of a glycerol-water mixture. The results are presented in appendix E.

3.5.4 Neutron spin echo

Neutron spin echo is a time-of-flight technique that measures the intermediate scattering function $I(\mathbf{q}, t)$. The technique involves manipulation of the spin state of the neutrons with the purpose of determining the flight time of each scattered neutron. The technique was developed by Mezei and described in [53]. I will follow the presentation given in [46].

The main components of the neutron-spin-echo experiment are two magnetic coils, two $\pi/2$ spin flippers, a spin analyser, and a detector. The neutron will encounter the components in the following order: Spin flipper, coil, sample, coil, spin flipper, analyser, and detector.

A neutron submitted to a magnetic field will start to precess around the direction of the magnetic field with a Larmor frequency, ω_l, given by $\omega_l = |\gamma|B$ with γ being the gyromagnetic ratio of the neutron and B is the strength of the magnetic field. The accumulated precession angle of a neutron traveling a distance, l, with velocity, v, in a magnetic field of strength B will be:

$$\Phi = |\gamma|\frac{l}{v}B \tag{3.23}$$

The first flipper aligns the spin of the neutron to be perpendicular to the magnetic field, B_1, in the first coil of length l. The neutron then interacts with the sample. After the sample the second coil with field $B_2 = -B_1$ and length l, is located. Then final spin flipper stops the precession of the neutron. After this there is a polarisation analyser that measures the polarisation of the incoming neutron and finally a detector.

If the scattering from the sample is elastic the accumulated phase angle from traveling in the two coils will be zero since the same amount of time is spend in either of the coils. But if the scattering is in-elastic the neutron will spend a shorter or longer time in the second coil, leading to a accumulated phase angle.

The polarisation analyser measures the polarisation which is the cosine of the accumulates phase angle of the neutron

$$P = \langle \cos(\Phi) \rangle \tag{3.24}$$

which in turn in related to the intermediate scattering function [53]

$$\langle P \rangle \approx \int_{-\infty}^{\infty} S(\mathbf{q}, \omega) \cos(\omega \tau_{NSE}) d\omega \approx I(\mathbf{q}, t) \tag{3.25}$$

Where $\langle P \rangle$ is the average polarisation of the scattered neutrons. τ_{NSE} is the spin-echo time, which approximated the Fourier time, t[46]. τ_{NSE} can be changed by changing the strength of the magnetic fields in the coils, or by changing the incoming wavelength. This is what determines the time-range of the instrument.

In the above presentation we assumed perfect working conditions of the spectrometer. We assumed no beam divergence, no field inhomogeneities, perfect analyser etc. In practice this will not be the case. The time-range that can be

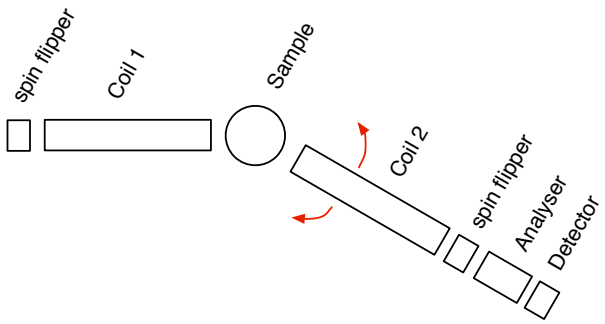

Figure 3.8: Schematic drawing of a typical neutron spin echo experiment. The neutron enters from the right and goes through the components. The right hand side of the sample can be rotated to cover different scattering angles.

covered by the spectrometer is determined by the resolution function, $R(\mathbf{q},t)$, which depends on all these factors. So to get the final result[46]:

$$I(\mathbf{q},t) = \frac{I_m(\mathbf{q},t)}{I_m(\mathbf{q},0)} \frac{R(\mathbf{q},0)}{R(\mathbf{q},t)} \tag{3.26}$$

where $I_m(Q,t)$ is the measured, uncorrected, intermediate scattering function.

Neutron-spin-eco was used to study the dynamics at $q = 1.5\text{Å}^{-1}$ of n-butanol in the 175 K to 280 K temperature range. It was also used to study the $q-$dependence of the dynamics $q = 1\text{Å}^{-1}$ to $q = 1.6\text{Å}^{-1}$ range. The results are presented in chapter 6.

Part II

Results

4 | Crystallisation of n-butanol

This chapter in an extension of Paper A. It contains a more thorough analysis of the data as well as results from simultaneous dielectric and neutron scattering experiments. Some repetition of the results presented in Paper A was necessary to make the reading of this chapter easier.

4.1 Introduction

The question we are interested in answering is: "How does the dielectric spectrum change during crystallisation, and what does that tell us about dynamics in a system undergoing a phase transition". The first part of the question requires that we fit the spectrum during crystallisation. Section 4.2 describes the fitting procedure. The results of this fitting procedure are presented and discussed in sections 4.3-4.5. That covers the first part of the question. For the second part we rely on the Avrami analysis and Maxwell-Wagner analysis as described in chapters 2 and 3. Section 4.6 and 4.7 present the results of applying these analyses to the crystallisation of n-Butanol. In section 4.8 the reproducibility of crystallisation experiments is discussed. This leads to sections 4.9-4.9.2 which present data from two simultaneous dielectric and neutron scattering experiments. Finally section 4.10 give concluding remarks.

4.2 Fitting the dielectric spectra

In the measured frequency window n-Butanol has three visible processes: The Debye, alpha, and beta process. They are seen clearly in fig. 4.1 (a) which show the dielectric loss vs. frequency on a log-log scale.

During crystallisation the relation strength decreases and the peak position shifts for the three processes. This is shown in fig. 4.1 (b) for a crystallisation run made at 130 K. The beta relaxation process, however, remains active by the termination of the crystallisation process. The inset in fig. 4.1(b) shows the last scan at 130 K together with a measurement of the full crystal at the same temperature, clearly demonstrating that the crystallisation process stops before the sample is fully crystallised and that there is still some molecular mobility left. The results from the fitting routine establish the general behaviour of the spectra during the crystallisation.

To quantify how the crystallisation influences each of these processes, we fitted the spectra to a sum of three relaxation processes. Since the processes are not well separated, we aimed at limiting the number of free fitting parameters

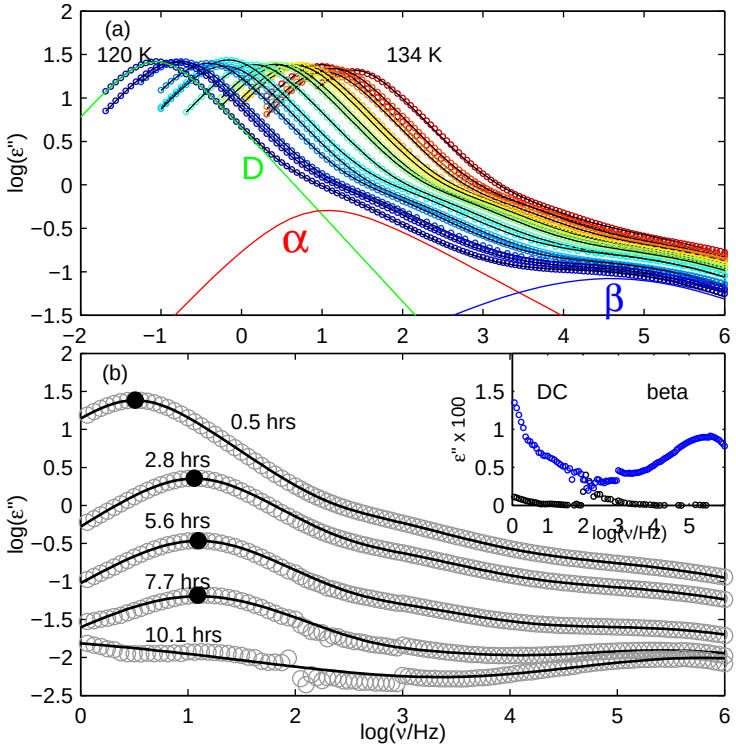

Figure 4.1: The fitting procedure yields convincing fits in the entire temperature range, going from 120 K to 134 K, see (a). The individual relaxation processes are shown for the 120 K measurement. The same fitting procedure applied to the isothermal crystallisation likewise yields fits that are in good agreement with the data, up to a point, as (b) show for crystallisation at 130 K. The inset show the last measurement at 130 K (blue) together with the measurement of the full crystal at the same temperature. Clearly the the β process survives the crystallisation process.

by the following procedure: First the Debye process is fitted by a Cole-Cole function. The Debye process broadens during the crystallisation and thus a pure exponential function would not give a good fit. The result of the Debye fit is then subtracted from the data and the alpha and beta processes are fitted simultaneously as a sum. The beta process is fitted to a Cole-Cole function with a fixed shape parameter, $\beta = 0.45$. The alpha process is fitted to a dielectric version of the Extended Bell model. The entire expression for the complex dielectric permittivity becomes:

$$\epsilon^*(\omega) = \epsilon_\infty + \frac{\Delta\epsilon_D}{(+(i\omega\tau_D)^s} + \frac{\Delta\epsilon_\alpha}{1 + \frac{1}{(1+\omega\tau_\alpha)^{-1} + k_\alpha\,(i\omega\tau_\alpha)^{-\alpha}}} + \frac{\Delta\epsilon_\beta}{1+(i\omega\tau_\beta)^\beta}. \quad (4.1)$$

Here each relaxation process has a relaxation time, τ_x, and a relaxation strength, $\Delta\epsilon_x$ (x denoting Debye, alpha, or beta). The expression contains four shape parameters: s, k_α, α and β. k_α controls the width of the alpha peak, and α gives the high-frequency power law behaviour of the alpha peak. The slope parameter was fixed to $\alpha = 0.5$ and $k_\alpha = 1$. Thus, the imaginary part was fitted to a total of seven parameters: a relaxation time and a relaxation strength for each process and a broadening parameter, s, for the Debye process.

The procedure gives excellent fits of over the frequency range explored as shown in fig. 4.1(a), where the first are shown in black. The individual relaxation processes are shown for the 120 K measurement. The same fitting procedure was applied to the isothermal crystallisation spectra. The results are shown in fig. 4.1 (b) for crystallisation at 130 K using cell B. The fits capture the changes in the spectra quite well.

In the following three section the changes in relaxation strength, relaxation frequency and stretching will be described and discussed.

4.3 The decrease in relaxation strength

The changes in relaxation strength taking place during the crystallisation are summarised in fig. 4.2 where we show the normalised relaxation strength as a function of the time. The colours of the curves indicate the temperature with blue being the lowest (120 K) and red being the highest (134 K). In both cells, lower temperatures lead to longer crystallisation times.

For cell A (fig. 4.2 left panels) the fitted relaxation strengths for each of the three processes appear similar, except at long times, where the beta relaxation strength levels off at roughly 0.08 instead of decaying all the way to zero. For cell B (fig. 4.2 right panels), the Debye and alpha relaxation strengths follow each other until roughly halfway through the crystallisation, where a shoulder emerges in the alpha relaxation strength curve, which then proceeds like a two-step process. As in cell A, the beta relaxation strength does not decay to zero and levels off at the same value as for cell A. Comparing the left and right panels of fig. 4.2, it becomes clear that the curves for cell B are significantly more stretched than the corresponding curves for cell A. Consequently, our definition of crystallisation time may give roughly the same for the two cells, however total crystallisation time is much longer in cell B.

The normalised relaxation strength is shown on a log-log scale in fig. 4.3. The Debye decay curve is more evidently different between the two cells in this plot. With the log scale it becomes clear that the beta process survives the crystallisation at all temperatures. Furthermore, it appears that the beta relaxation strength levels off at higher values for lower temperatures.

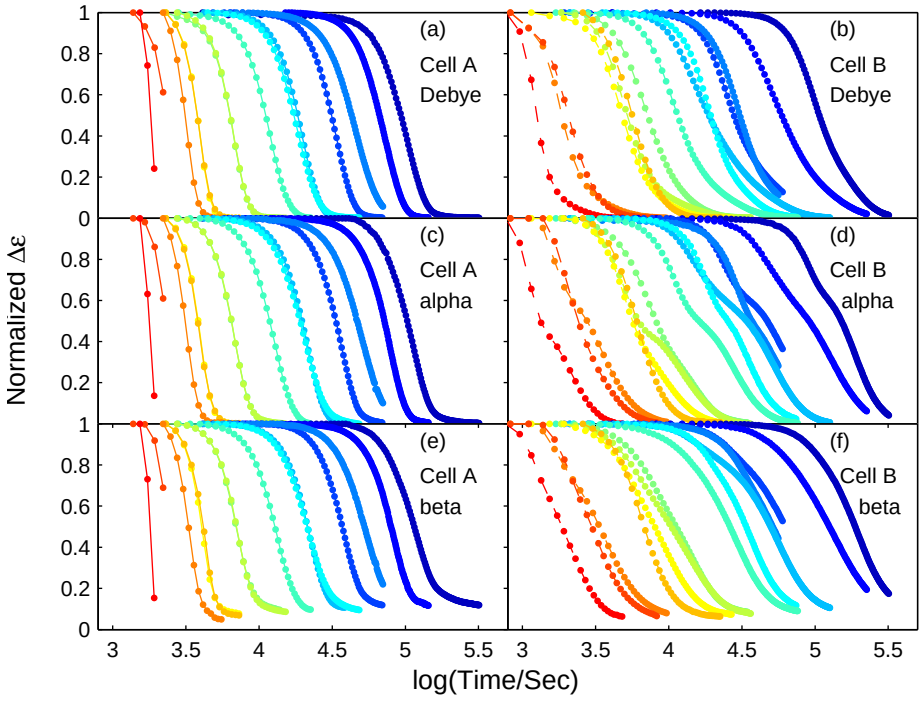

Figure 4.2: Comparing the normalised relaxation strength of the three processes for both cells. Generally speaking the decay of the relaxation processes proceeds differently for the two cells. For the Debye process, this is seen as a long-time tail, suggesting that the crystallisation process slows down after the normalized $\Delta\epsilon$ has reached 0.5. For the alpha relaxation strength we see a bump occurring normalized $\Delta\epsilon = 0.6$, making the decay curve look like a two-step process. The beta decay curve generally look more stretched for cell B than A. Taken together, it suggests that the crystallisation proceeds differently in the two cells.

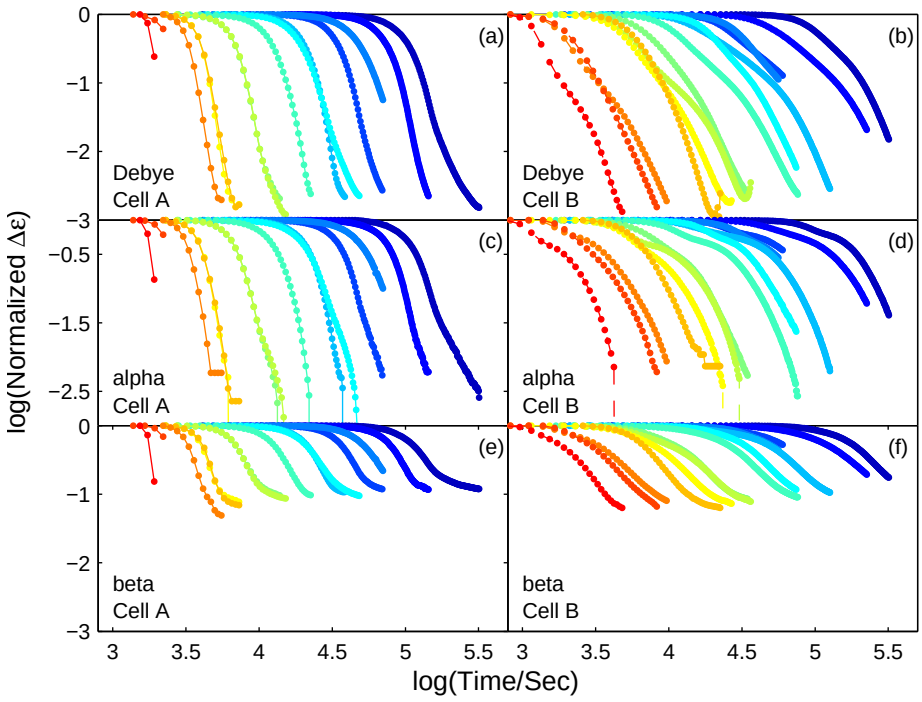

Figure 4.3: The Debye decay curve is more evidently different between the two cells in this plot. With the log scale it becomes clear that the beta process survives the crystallisation at all temperatures. Furthermore, it appears that the that the beta relaxation strength levels off at higher values for lower temperatures.

4.4 The changes in relaxation frequency

The relaxation frequency changes during the crystallisation process, as is shown in fig. 4.4. Once again a differences between the two cells are observed. For Cell A the relaxation frequency increases slightly at the beginning of the crystallisation process, but remains more or less constant until the normalised $\Delta\epsilon$ reaches 0.1. For cell B there is no initial increase, but rather a more gradual change from beginning to end. The behaviour for the Debye and alpha processes appear to be consistent for all temperatures. In the case of the beta relaxation, the changes are much more chaotic, especially at higher temperatures.

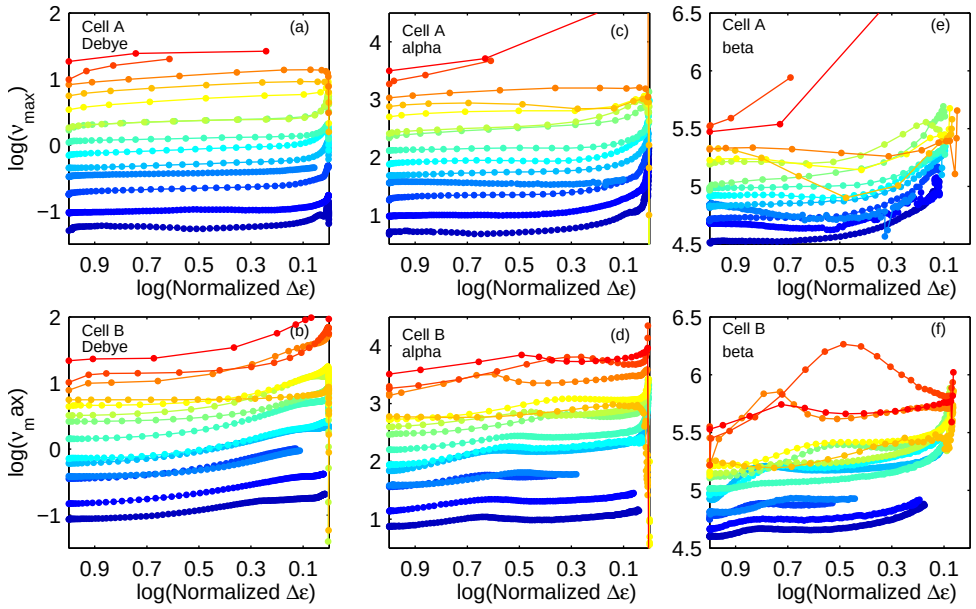

Figure 4.4: As the crystallisation proceeds the relaxation frequencies of all three processes change. Once again there are differences between the two cells. In cell A we see an initial increase followed by little to no change until late in the crystallisation process ($\Delta\epsilon \leqq 0.1$) after which an increase takes place. For cell B the increase is more gradual during the entire crystallisation process. The beta relaxation times behave less systematic for both cells, especially at higher temperatures where the relaxation time changes frantically.

4.5 The stretching parameter

We now turn to the last of the fitting parameters, the Debye stretching. During the crystallisation process the Debye relaxation broadens. Again beta behaves differently between the two cells, as shown in figure 4.5 where we show the broadening as a function of time.

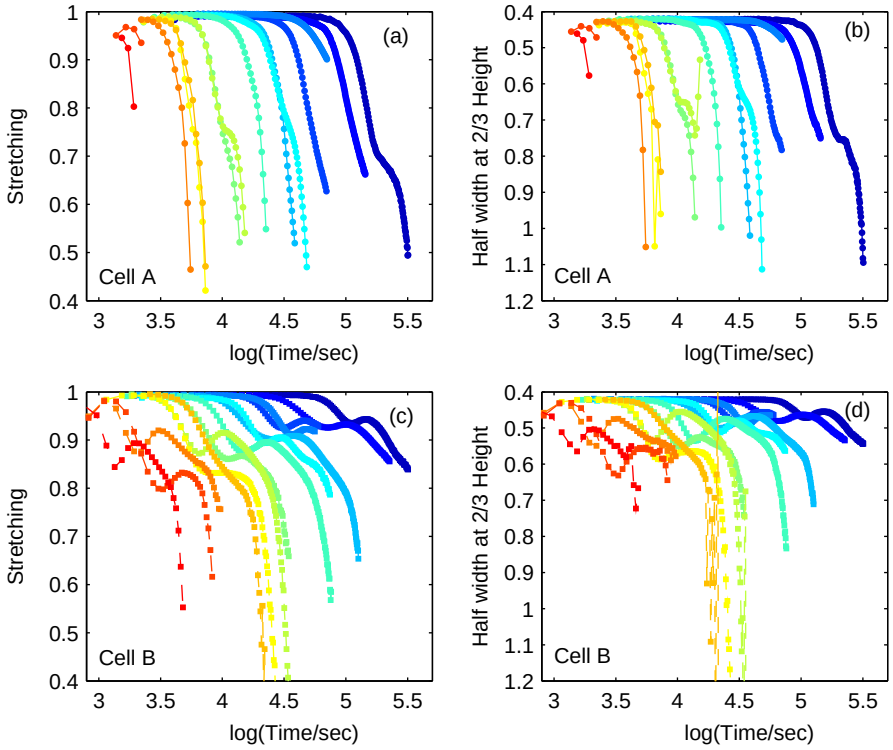

Figure 4.5: During the crystallisation the the Debye process broadens from 1 to 0.4 during the crystallisation. The evolution is different for the two cells. In cell A it decreases monotonously, with a slight bump. In cell B the broadening is not monotonous, which is surprising. Comparing the stretching parameter to a model-free measure of the stretching, we see that the two are practically identical. The model free measure is the half width at 2/3 height.

In cell A it decreases monotonously as the crystallisation progresses, albeit with a bump. The same can not be said for cell B. where the bump is so pronounced that beta actually increases slightly at a point during the crystallisation. This behaviour is odd and unexpected.

To make sure that it is not merely an artefact of the fitting procedure we defined a measure of the broadness of the Debye process: The half width (meas-

ured in decades of Hz) at 2/3 height. The 2/3 are chosen rather arbitrarily. The results are shown in fig. 4.5 (b) and (d). The resemblance between our measure and the beta stretching parameter is striking.

Rather than looking at the stretching as a function of time we can use the degree of crystallinity. We have tried with both the normalised relaxation strength and the degree of crystallinity, as found with the Maxwell Wagner analysis (will be explained in sec. 4.6). The results are shown in fig. 4.6. Within each cell the behaviour is qualitatively similar, but between the cells it is quite different.

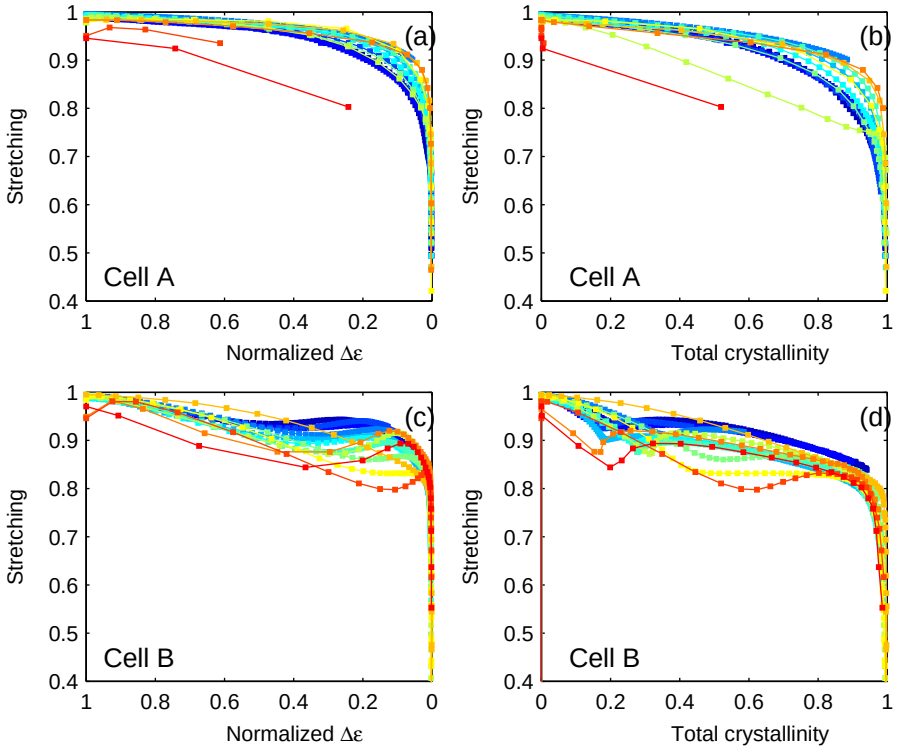

Figure 4.6: By plotting the stretching agains the normalized $\Delta\epsilon$ we can better compare the stretching across the temperatures. Within each cell the behaviour is qualatively similar, but between the cells it is quite different. In cell A there is a tendency for the stretching to decrease more slowly with increases temperature. The opposite is true for cell B.

The question posed in the introduction of this chapter: "How does the dielectric spectrum change during crystallisation" has now been answered. I have shown that the changes in the spectrum depends on the sample cell, but both cells give consistent results across a broad temperature range. The fact that

the changes depend on the cell used is not promising for answering the: "and does that tell us about the dynamics in a system undergoing phase transition" part of the question. Therefore, it is necessary to explain why the cells give consistently different results before speculating on how the dynamics change during crystallisation. The next couple of section will be devoted to explaining the difference between the cells.

4.6 Physical interpretation: Maxwell-Wagner polarisation

It is common to use the normalised relaxation strength as a measure of the degree of crystallinity of a sample. The reasoning behind this is the following: We know that $\Delta\epsilon \propto \rho\mu^2$, with ρ being the density of dipoles taking part in the crystallisation process and μ being the dipole moment of a single molecule. If we assume that μ does not change during the crystallisation process, and that that molecules in the crystal phase do not contribute to the relaxation, then the relaxation strength should be proportional to the amount of liquid left in the sample. Thus $\Delta\epsilon(t)/\Delta\epsilon(t=0) \approx 1 - X_c$, with X_c being the crystalline volume fraction. However, as the crystallisation proceeds, the sample becomes a mixture of crystal and liquid which have different dielectric permittivities. The sample becomes heterogenous and we must account for the Maxwell-Wagner polarisation as described in sec. 3.3.

The two simplest cases of crystal domains growing in the liquid are that of a crystal layer growing from one (or both) of the electrodes and the case of crystal spheres in a liquid matrix. The first represents a heterogeneous nucleation picture while the second represents a homogeneous nucleation picture. I have given both results in sec. 3.3, but I will rewrite them here for convenience. For the layer model, the composite dielectric constant is given by:

$$\epsilon_{\text{comp}} = \frac{\epsilon_c \epsilon_l}{(1-\phi_{\text{layer}})\epsilon_c + \phi_{\text{layer}}\epsilon_l} \tag{4.2}$$

where $\phi_{\text{layer}} = d_c/d$ is the relative thickness of the crystal layer. Since ϵ_l and ϵ_c can be measured independently this model has one free parameter (assuming the distance between the electrodes is fixed, or equivalently that total thickness of crystal and liquid layer is unchanged during crystallisation). In the case of spherical crystal domains dispersed in a liquid the composite dielectric constant is given by:

$$\epsilon_{\text{comp}} = \epsilon_l \frac{2\epsilon_l + \epsilon_c - 2\phi_{\text{spheres}}(\epsilon_l - \epsilon_c)}{2\epsilon_l + \epsilon_c + \phi_{\text{spheres}}(\epsilon_l - \epsilon_c)}. \tag{4.3}$$

where ϕ_{spheres} is the concentration of the crystal domains. This model also contains a single fitting parameter, ϕ_{spheres}. We combine the two models such

that a crystal layer is growing from the electrodes, while spherical crystallites are forming in the remaining liquid. This is modelled by combining eq. 4.2 and eq. 4.3 such that ϵ_l in eq. 4.2 is given by the composite dielectric constant from eq. 4.3. This model has two parameters: The relative thickness of the crystal layer, ϕ_{slab}, and the concentration of crystal spheres in the liquid, ϕ_{spheres}. The total crystallised volume fraction according to the model can be calculated as:

$$X_c = X_{\text{spheres}} + X_{\text{layer}} = (1 - \phi_{\text{layer}})\phi_{\text{spheres}} + \phi_{\text{layer}}, \tag{4.4}$$

and the volume fraction taken up by the spheres alone as

$$X_{\text{sphere}} = (1 - \phi_{\text{layer}})\phi_{\text{spheres}}. \tag{4.5}$$

To put an emphasis on the behaviour of the Debye relaxation process we fit the combined Maxwell-Wagner model to the points around the maximum of the Debye process. In fig. 4.7 (a) and (d) a selection of Maxwell-Wagner fits to measurements made at 127.5 K for both cells are shown. In (b)-(c) I show the fitting parameters and in (e)-(f) the calculated volume fractions are shown. The colours are consistent across the panels.

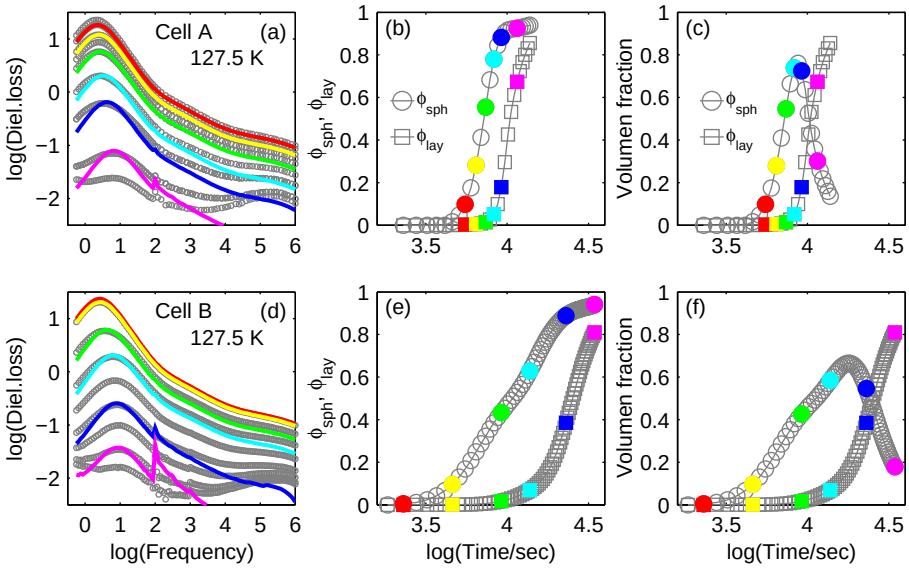

Figure 4.7: Knowing that the mean-field approximation is pushed well above the $\phi_{\text{spheres}} \approx 0.2$ limit, it is only fair to show the fits together with the values of ϕ_{spheres} and ϕ_{layer}. The failure of the fits to take into account the beta relaxation begins to be apparent around $\phi_{\text{spheres}} \approx 0.6$ (green).

In sec. 3.3 we stated that the MW model with the spheres was based on a mean-field approximation that could only be expected to be valid to $\phi_{\text{spheres}} \approx$

0.2, and yet, in the numerical calculation we allowed for the parameter to each 1. As ϕ_{spheres} approaches 1, not only does the idea of a mean-field approximation break down, the idea of spherical crystallites submerged in a liquid also become nonsense. Nevertheless we do not restrict ϕ_{spheres} in the coming analysis. Were we to adhere to the limitation of the mean-field approximation, everything after and including the yellow curve should be neglected. However, the yellow curves still agrees well with the data. For the cyan (light blue) curve the fit stats to deviate at the alpha process and does not fit the beta process at all, but the position and height of the Debye process is still captured by the fit. In fact the fits continue to catch the height and position of the Debye process for the blue and magenta curves, but neither the stretching of the Debye nor the strength of the α and β processes are captured. However, at this point $\phi_{\text{Spheres}} \approx 0.9$. Not bad for a mean-field approximation.

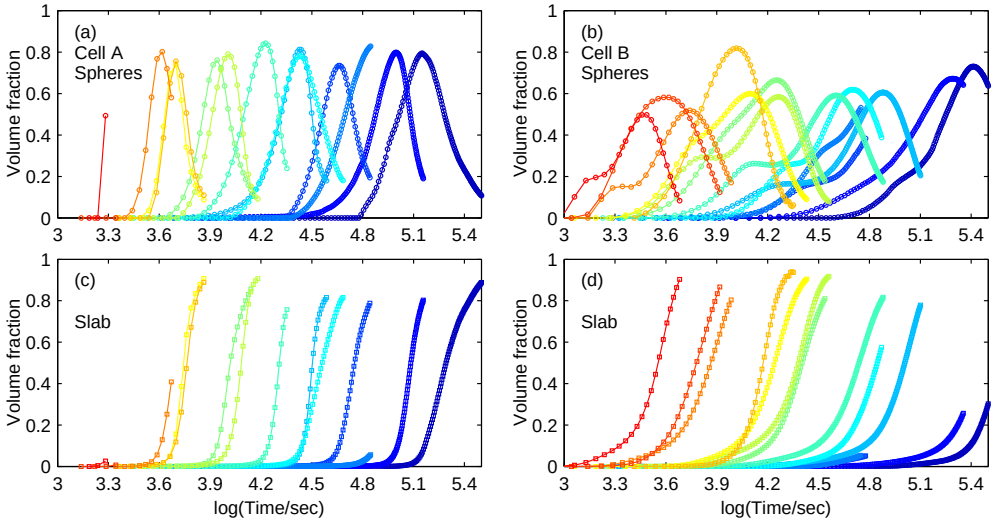

Figure 4.8: The volume fraction taken up by spherical and layer crystal domains as a function of time on a log scale. The results are clearly different between the two cells.

In fig. 4.8 the results of applying the analysis described above to all temperatures are shown. The physical picture that arises from the results is the following: For both cells the onset of crystallisation is dominated by nucleation and growth of crystal spheres, and when a large fraction of the sample has crystallised ($X_c \approx 80 - 90\%$), the layer growth takes over. However, the growth of crystal spheres starts earlier but proceeds at a slower rate in cell B compared to cell A. This difference in crystallisation behaviour in the two cells is seen for

all temperatures, as fig. 4.8 clearly shows.

Rather than plotting the volume fractions as a function of time, we can plot them as a function of the total crystallinity, X_c. This is done in fig. 4.9. In cell A the crystal growth is dominated by spheres until a crystallinity close to 80%. In cell B the layer stats to grow already around 20% crystallinity, resulting in a mixed growth that lasts until a crystallinity close to 80%, after which the layer growth dominates. Generally there is more variability in cell B than in cell A.

From fig. 4.2 in section 4.3 we know that the different relaxation processes react differently to the crystallisation process. In this section we have focused on the Debye process, but this was partly a matter of convenience since fitting to the alpha or beta process would be very difficult. So which, if any, of the relaxation strengths correlates with the crystallinity from the Maxwell-Wagner analysis? In fig. 4.10 I show the normalised relaxation strength for each of the processes as a function of the total crystallinity from the MW analysis. Generally speaking the correlation is better in cell A than in Cell B and the alpha and beta processes seem to correlate better with the crystallinity than the Debye process does.

In this section I have presented a possible explanation of the difference in the dielectric spectra produced by the two cells. In the next section I will use a more standard analysis and compare the results with the Maxwell-Wagner analysis.

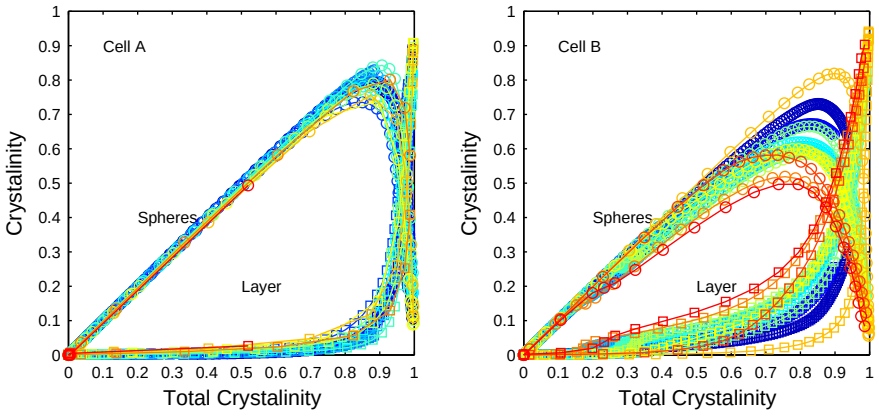

Figure 4.9: To compare the growth of the spheres and the layer across temperatures and both cells, we plot the volume fraction taken up by the spheres and slab as a function of the total crystallinity of the sample. This shows nicely the difference between the two cells. In cell A the crystal growth is dominated by spheres until a crystallinity close to 80%. In cell B the layer stats to grow already around 20% crystallinity, resulting is a mixed growth that lasts until a crystallinity close to 80%, after which the layer growth dominates.

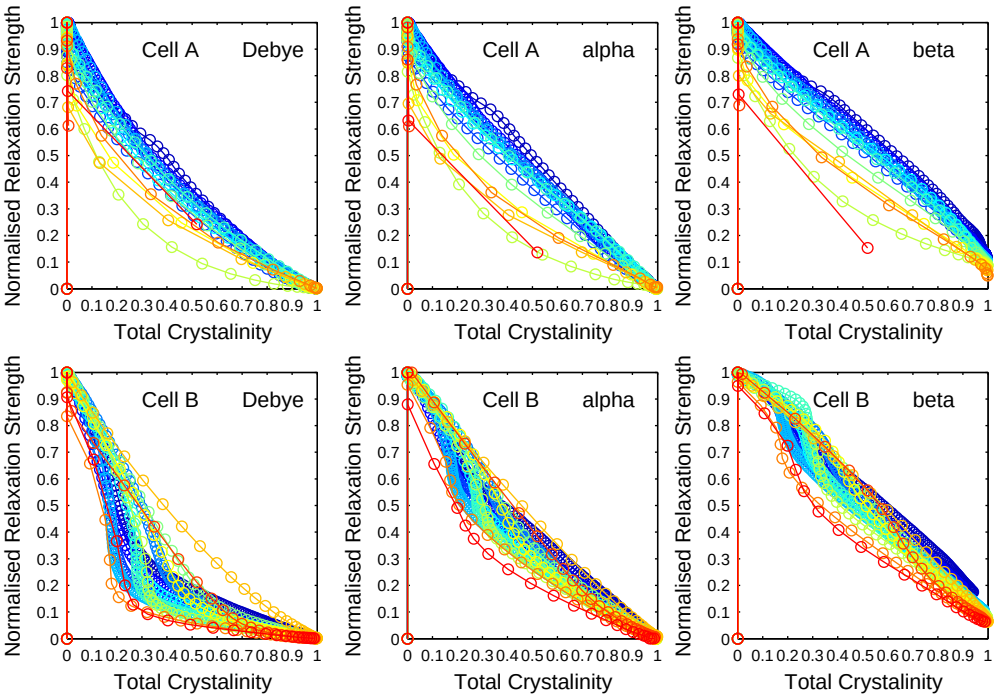

Figure 4.10: The normalised relaxation strength as a function of the total crystallinity for the Debye and alpha process for each cell. Generally speaking the correlation is better in cell A than in Cell B and the alpha and beta processes seem to correlate better with the crystallinity than the Debye process does.

4.7 Avrami analysis

As explained in chapter 2 one way to analyse crystallisation kinetics is to use the Avrami equation to get information about the morphology of the crystal growth. In the Maxwell-Wagner analysis the morphology enters the analysis explicitly, so how does the two kinds of analysis compare?

As stated in chapter 2 the Avrami equation give the crystallinity of the sample as a function of time given the growth rate, k and Avrami parameter n are known, that is:

$$X_c(t) = 1 - \exp\left[-kt^n\right] \tag{4.6}$$

We can get n as the slope in a plot of $\ln(-\ln(X_c)$ against $\ln(t)$. A change in slope indicates a change in n, which contain the information about the morphology. This still leaves us with the problem of getting X_c. As I stated in the beginning of last chapter it is common to use $X_c \approx \Delta\epsilon(t)/\Delta\epsilon(0)$, but then we still have to decide on which relaxation strength to use. But instead of deciding on any of them I simply used all of them.

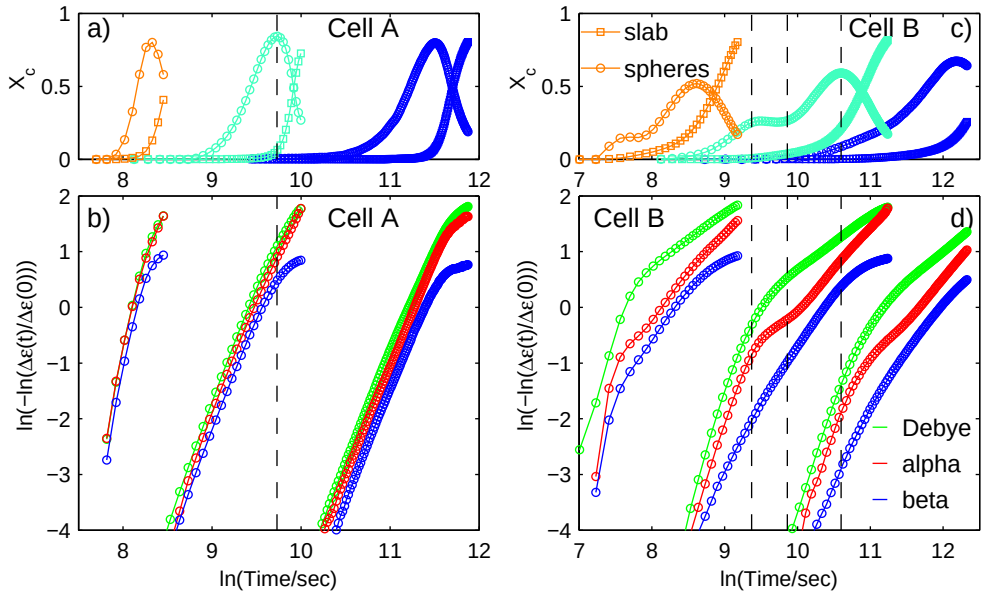

Figure 4.11: Comparing the Maxwell-Wagner and Avrami analysis. There is some resemblance between the results form the two kinds of analysis. The conclusion to be drawn from both kinds of analysis the the same: In both cells there is change in the morphology of the crystal growth, and this change occurs earlier in cell A then cell B.

In fig. 4.11 the results of the Maxwell-Wagner and Avrami analysis are

compared. (a) and (c) show the same as fig. 4.8, but this time on a $\ln(t)$ axis so it can be compared directly with the Avrami analysis. (b) and (d) show the results of the Avrami analysis. I show the results for each of the relaxation processes for the sake of completeness. To keep the figure readable only three temperatures are shown for each cell.

We are looking to see if a change in slope in (b) and (d) occur at the same time as the change from spherical to slab growth. Looking first at cell A in (a)-(b), it seem that the slope changes at the same time as the onset of the layer growth. In cell B the situation is more complicated. The change in slope occur at different times for the different relaxation processes. However, there is resemblance between the changes in the Avrami plot and the Maxwell-Wagner results.

The conclusion to be drawn from both kinds of analysis is the same: In both cells we see a change in the morphology of the crystal growth from a 3D growth to a 2D growth, and this change occurs earlier in cell A than in cell B.

4.8 Reproducibility

Even though the different temperatures appear to yield qualitatively similar results, one might worry about the reproducibility of the results for any given temperature. It is the aim of this section to investigate just how reproducible these experimental are.

Fig. 4.12 shows the result of doing ten experiments at 127.5 K. The cell was emptied and cleaned between each run. In (a)-(c) the normalised relaxation strength for each of the relaxation processes are shown together with a measurement done at 129 K and 126 K. While the shape of the decay is different for each run, the crystallisation time is quite similar. In (d)-(f) I show the relaxation frequency for each process. The behaviour is qualitatively the same for each run. It is a bit surprising that the initial frequency is different between runs. It suggests that the cryostat does not stabilise at the same temperature for each run. The broadening of the Debye process is spread out, but the overall shape is similar between the runs.

Fig. 4.13 shows the results of applying the Maxwell-Wagner analysis to the ten crystallisation runs. The time evolution of the volume fraction taken up by spheres (a) and layer (b) look shifted for the different measurements. However, the overall tendency of spheres growing before the layer is observed for all measurements. Furthermore, the shifting might simply be due to a difference in the induction time. Plotting the volume fraction taken up by spheres and layer against the total crystallinity, we see that the curves collapse quite nicely, see (c) and (d). (e) and (f) show a similar plot, but using the normalised

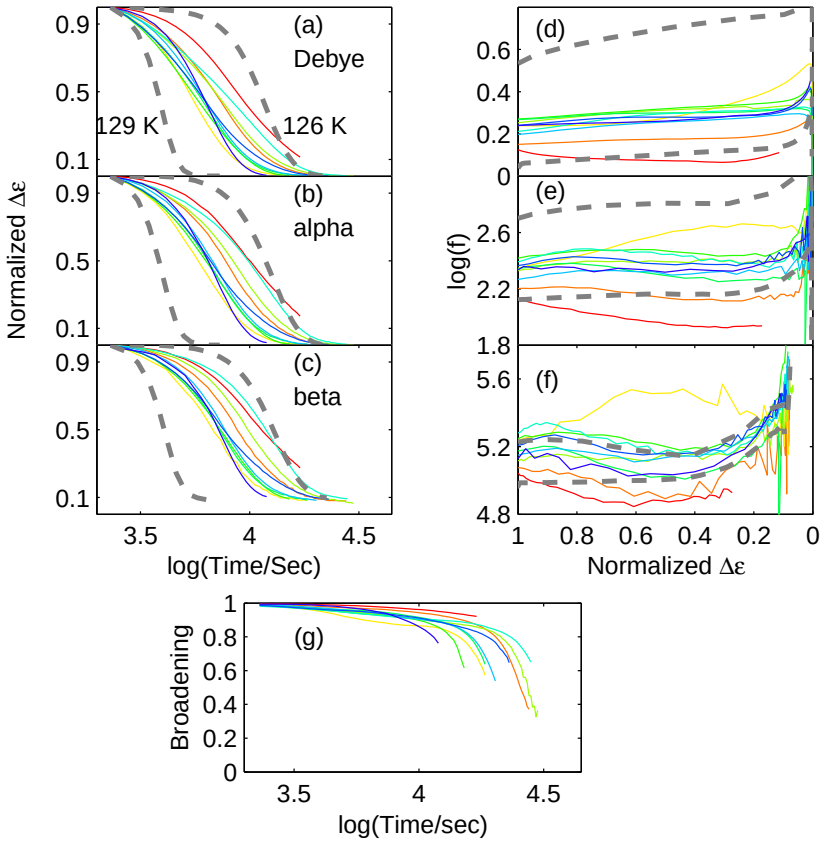

Figure 4.12: The results on the fitting routine for 10 measurements done at 127.5 K. The evolution of the Debye (a) alpha (c) and beta (e) processes vary between the different measurements. For the relaxation frequency the qualitative behaviour is consistent between the measurements. It is a bit surprising that, for some of the measurements, the initial frequency appears to differ between the runs.

relaxation strength rather than the total crystallinity.

The conclusion to be taken away from this section is the following: If we want to test the Maxwell-Wagner model the experiments need to be done simultaneously.

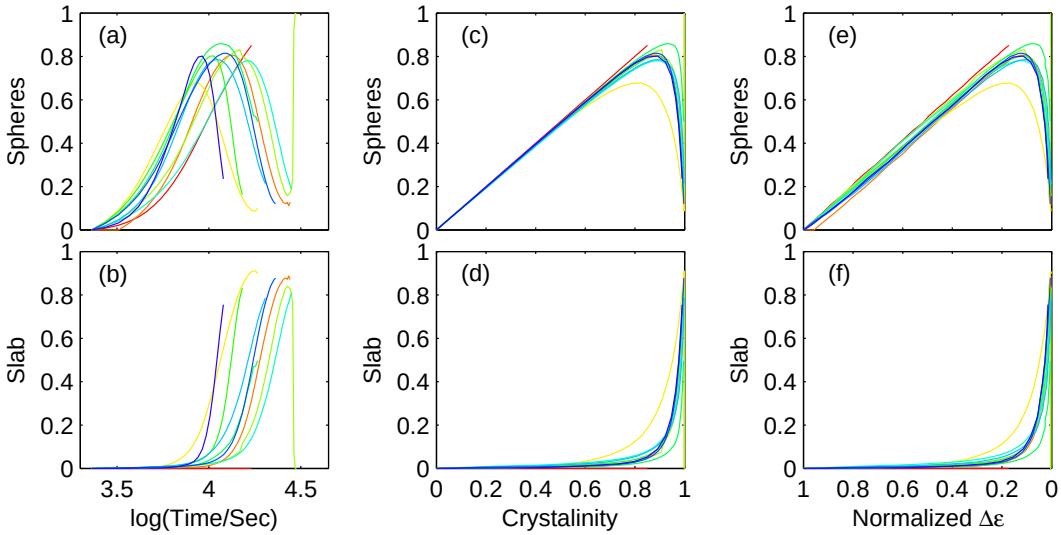

Figure 4.13: The results of the Maxwell-Wagner analysis for 10 measurements at 127.5 K. The time evolution of the volume fraction taken up by spheres (a) and layer (b) looks shifted for the different measurements, but the overall tendency of spheres growing before the layer is observed in all the measurements. Furthermore, the shifting might simply be due to a difference in the induction time. Plotting the fraction taken up by spheres and slab against the total crystallinity we see that the curves collapse quite nicely, see (c) and (d). (e) and (f) show a similar plot, but using the normalised relaxation strength rather than the total crystallinity.

4.9 Simultaneous dielectric spectroscopy and neutron diffraction

The main conclusion to take away from the results stated above is that minor differences in the design of the sample cell can lead to major differences in the observed quantity. This makes comparison between cells difficult. This is especially the case the comparison is across different experimental techniques, where the differences in the cell design can be substantial. Never the less it is often necessary to combine the results of different experimental techniques to fully understand the changes that a sample undergoes during a phase transition – this is exactly what we need if we want to test the Maxwell-Wagner analysis described above. This leaves us with a problem: We know that comparison between different experimental techniques can be risky, but we need to do it in order to understand our samples. An obvious, but difficult, solution to this problem is to design experiments that allow for the simultaneous measurement of the relevant quantities. I have put a great deal of work into doing just that – to develop a dielectric cell for simultaneous neutron scattering and dielectric spectroscopy.

Designing and testing a cell is a iterative process. During my Ph.d. I tested two version of the cell – one in 2013 and one in 2016. Results from both tests are included in the following sections. For a more detailed description of the development of the two cell, please see appendix C.

4.9.1 The results from 2013

We did two crystallisation runs, one at 130 K and another at 133 K. In both cases the cell was quenched outside the cryostat to liquid nitrogen temperature before being placed in the cryostat which was set at 90 K. The sample was then heated inside the cryostat to the annealing temperature. In all cases the temperature given is the set-point of the cryostat. The actual temperature of the cell was one or two kelvins above the set-point because the regulating thermocouple was placed further up the sample-holder stick to avoid inference with the neutrons.

The simultaneous neutron diffraction and dielectric spectroscopy was successful in the sense that we were able to see changes occurring simultaneously. The results are shown in fig. 4.14. Several minor difficulties makes a thorough analysis practically impossible. See appendix C for the details of the problems.

Qualitatively we can say that the strength of the Debye process decays faster than the crystallinity grows which is what we would expect from the Maxwell-Wagner analysis.

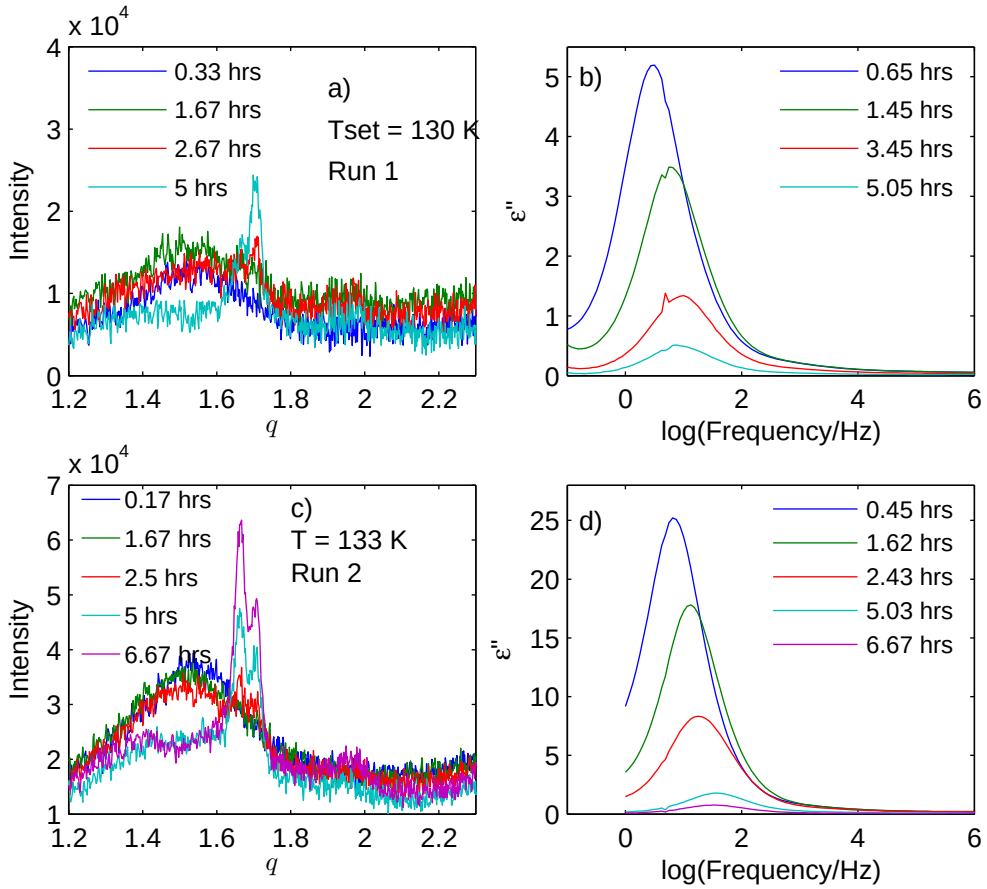

Figure 4.14: Results from the two simultaneous dielectric spectroscopy and neutron scattering experiments. Several minor difficulties makes a thorough analysis practically impossible, but the dielectric relaxation strength drops by more than 50% before strong signs of crystallisation appear in the diffraction pattern.

4.9.2 The results from 2016

In 2016 we had six crystallisation runs, two of which include simultaneous neutron and dielectric measurements.

The dielectric measurements covered the range from 0.1 Hz to 1 MHz. Such a measurement takes approximately 12 minutes. The neutron measurement were carried out with a fixed accusation time of 12 minutes to match the time it take to carry out a dielectric measurement. The q-range covered was 0.7-2.1 Å^{-1}.

The temperature protocol is sketched in fig. 4.15. The sample was put into the cryostat set to 220 K. From here the sample was cooled directly to the annealing temperature, T_a, at which we waited for the crystallisation. This temperature is the one given on all the coming figures. The sample was then heated to 165 K after having stayed at the annealing temperature for several hours. This was done to make sure that the sample was fully crystallised and to enable comparisons between the final crystal structure of the different crystallisation runs. After this the sample was then heated to 175 K so it melts. After this the sample was heated back to 220 K.

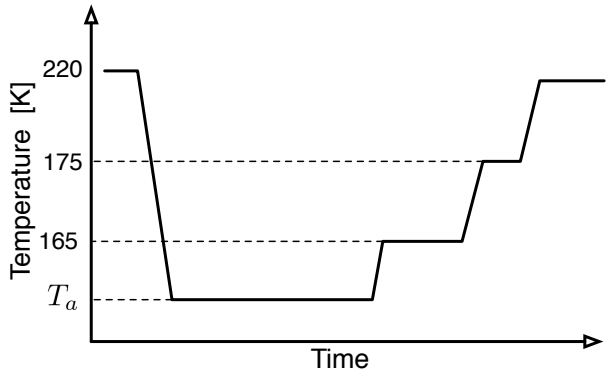

Figure 4.15: Sketch of the temperature protocol used in the experiments.

Out of the six crystallisation runs four were at 155K, one was at 160K and one was at 128K. However, the temperature given are the set-points of the cryostat. We know that the melting temperature of n-Butanol is 183.3K. So the fact that the sample melts at a set-point of 175K tells us that there is difference of at least 8.3K between the set-point and the actual temperature of the sample.

I will go through the six data sets. First I will analyse the neutron, then I will analyse the dielectric data. Finally the results from the simultaneous experiments will be analysed.

The neutron scattering results

While the main purpose of the experiments was to gain structural and dynamic information simultaneously, there are some interesting things to look at from a purely structural point of view. For example, one of the interesting aspects of the crystallisation of n-Butanol is the existence of an aborted crystallisation process, that leads to meta stable state[21, 36, 73]. This state has only been reported for a quench to low temperature followed by crystallisation at low temperatures. By looking at the differences between crystallising at 128K, 155K and 160K we can see how the temperature influence the final crystal state.

First let us get an overview of the differences between crystallising at 128K and 155K. Fig. 4.16 show a contour plot of the scattered intensity as a function of q and t for these two runs. The red lines mark the change in temperature. In both cases the measurements were started as soon as the temperature was changed from 220 K. This is why a shift to higher q-values of the broad liquid peak is seen in the beginning of the run.

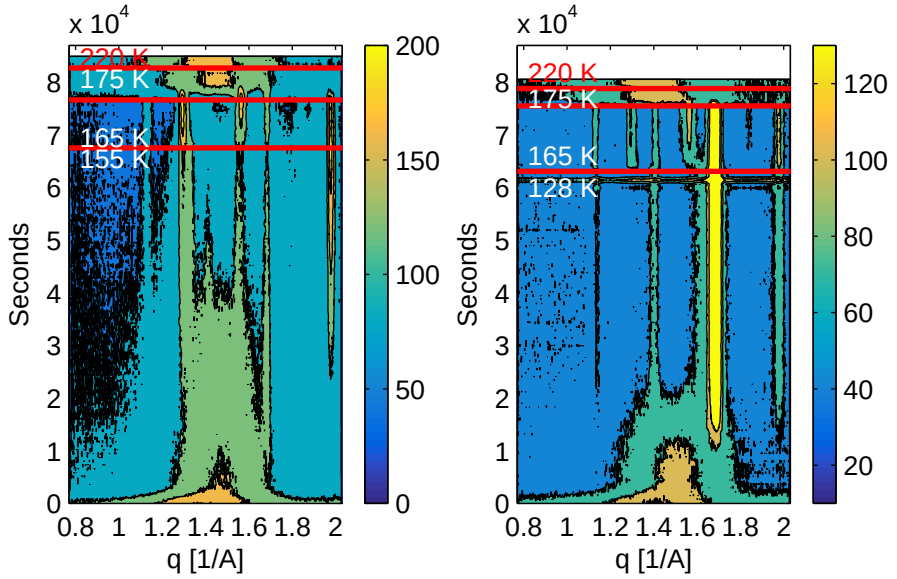

(a) Contour plot of run 1 at 155 K. **(b)** Contour plot of run 5 at 128 K.

Figure 4.16: The contour plots show the evolution of the scattered intensity with time. For crystallisation at 155 K we see the emergence of 6 peaks, of which the one around 1.9Å^{-1} is the most intense. For the annealing at 128 K the peak around 1.7 Å^{-1} is by far the most intense.

At 155 K six Bragg peaks emerge at approximately 1.1, 1.3 1.4 1.55 1.7 and

2 Å^{-1}. The run at 128K show a lot of similarity, but two differences remain: the Bragg peak at 1.7Å^{-1} is clearly the dominant peak, and the peak at 1.3Å^{-1} doesn't appear until the sample is heated to 165K. Once the samples are heated to 165K they show bragg peaks in the same positions, but the relative intensity of the Bragg peaks continue to be different.

There appears to be a difference in the kinetics as well. For the run at 155K the crystallisation appears to continue gradually from beginning to end whereas at 128K the sample reached a stable state relatively quickly.

While the contour plots are good at giving a quick overview of the entire crystallisation process, they are not good at giving a detailed view of the process. For this the 2D plot of the intensity as a function of q is better.

Looking at the intensity v.s. q plot from run 5 (fig. 4.17a) we can clearly see the difference between the meta stable state reached at 128K and the final crystal at 165K. From this plot it is clear the the main difference between the aborted crystallisation process and the final crystal in the intensity of the Bragg peaks at 1.3Å^{-1} and 1.55Å^{-1}. The Bragg peak at 1.7Å^{-1} changes very little from 128K to 165K.

But how does the final crystal from the 128K run compare to the ones at 155K and 160K? Comparing the final crystal at 165K of each of the runs (see fig. 4.17b) it becomes clear that for all the runs at 155K and 160K the crystalline structure is the same; the only difference being slight changes in the absolute level of the scattering intensity. For the run at 128 K, however, we see that the Bragg peaks are in the same positions as the other runs, but the most prominent peak is the one around $q = 1.7\text{Å}^{-1}$ rather than $q = 1.3\text{Å}^{-1}$ and $q = 1.9\text{Å}^{-1}$ as is the case for the runs at 155K and above. The explanation may be that a different crystal plane is favoured in the 128 K measurement, but since I only have the one crystallisation run at 128 K I have no way of knowing if it is a one-time thing or sometime significant.

Two conclusions can be drawn from the experiments described above. The first is that the annealing temperature may influence the structure of the final crystal. The second is that the meta-stable state reached at 128K does indeed appear to be an aborted crystallisation process, as has also been suggested in the literature [21, 36, 73].

Getting the degree of crystallinity from the neutron data

In addition to the structural information describe above we can get information about the kinetics of the crystallisation process. Ultimately, what I want is to the compare $X_c(t)$ from neutron scattering and dielectric spectroscopy. But first we will focus on the neutron data.

I obtain $X_c(t)$ as a fitting parameter by fitting a linear combination of the

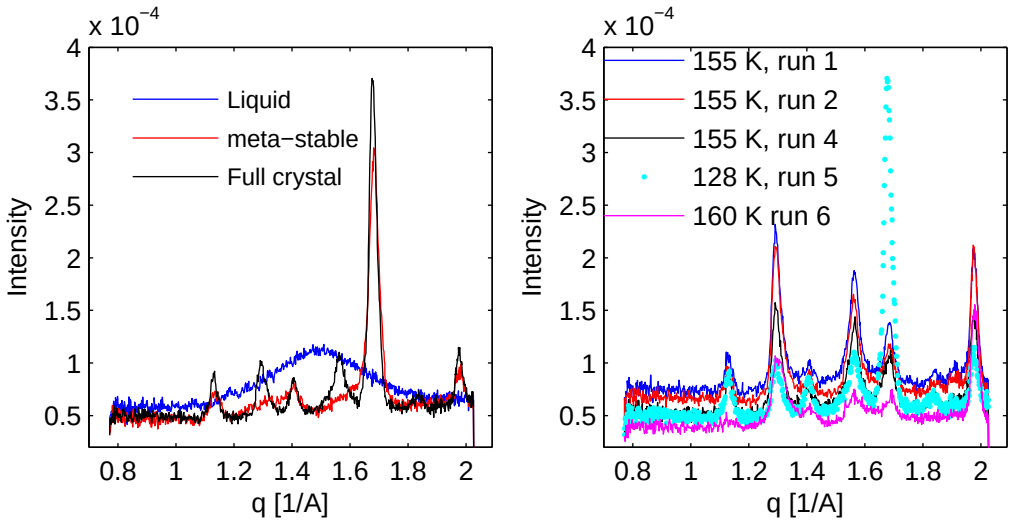

(a) Comparing the liquid, meta-stable crystal and full crystal for run 5

(b) The final crystal for each run

Figure 4.17: (a):The meta-stable state reached at 128K is clearly an unfinished crystallisation process. (b): We see quite clearly that all the crystallisation runs end up in the same crystal state. The only difference in the run at 128K is the relative intensity of the peak positions. The temperature given in the legend is the annealing temperature. All the crystals are at 165K.

liquid and crystal signal to each of the $I(q,t)$ curves. The intensity is expressed as a function of time in terms of the liquid and crystalline fraction of the sample. That is, we fit $X_c(t)$ in

$$I(t) = X_c I_{\text{crystal}} + (1 - X_c) I_{\text{liquid}}, \tag{4.7}$$

to each of the measurements. This model has a single parameter and it should fit the data nicely if the crystallisation process runs smoothly from the liquid state to the final crystal state. The results of using this fitting procedure on crystallisation at 155K and 160K are shown in figure 4.18a and 4.18b, respectively.

The red lines in fig. 4.18 are the results of fitting the entire q-range. This delivers fairly reliable results towards the end of the crystallisation, but at the early stages the fits produce a large peak around 1.9Å^{-1} while at the same time underestimating the peaks around 1.4 and 1.7Å^{-1}. In an attempt to overcome this I tried to fit only the peak around 2 Å^{-1}. These are the blue lines in fig. 4.18. Neither of the two fitting intervals deliver perfect fits. The black lines in fig. 4.18 show the average of the X_c from the two methods. Going forward the average of the two fitting method will be used.

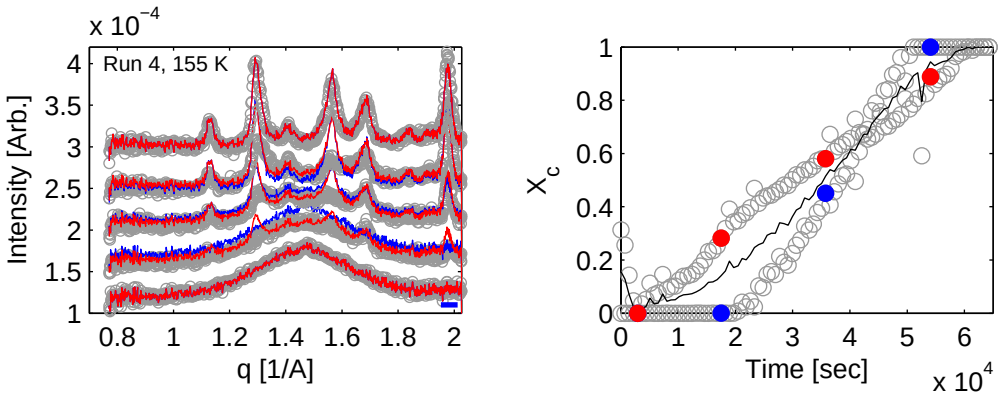

(a) Run 4, at 155 K

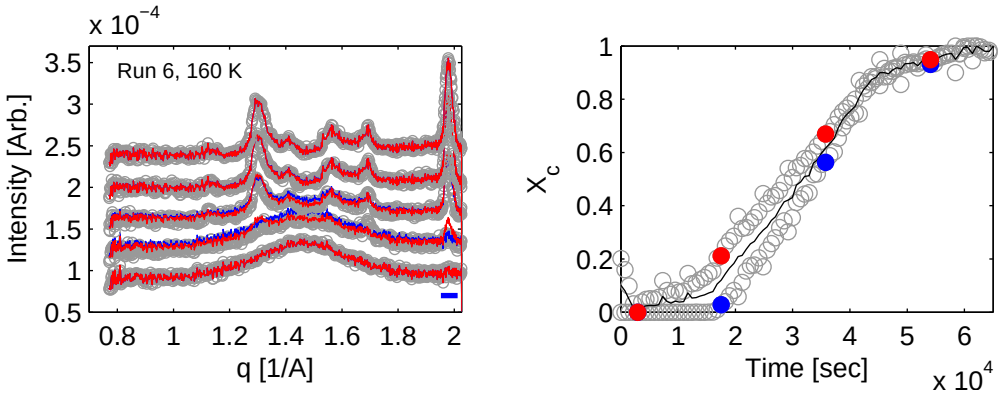

(b) Run 6, at 160 K

Figure 4.18: Overview of the results of fitting the neutron data. A sub-set of the data are shown in a) together with fits. Two approaches are being used: The red curves are the result of fitting the entire q-range. For the blue curves only the peak at 1.9 Å^{-1} was fitted. The quality of the fits are quite similar, but the resulting crystallinity differ by up to 20%, see panel b).

Now that we have $X_c(t)$ we can look at the crystallisation kinetics. The results of this fitting procedure applied to five of the crystallisation runs is summarised in fig. 4.19. The crystallisation kinetics look similar for the runs at 155K and 160K. The similarity between Run one and two at 155K is particularly striking. The sample was changed between run two and four which may partially explain the differences between run two and four. It is clear from fig. 4.19 that only the 128K run show a meta stable phase.

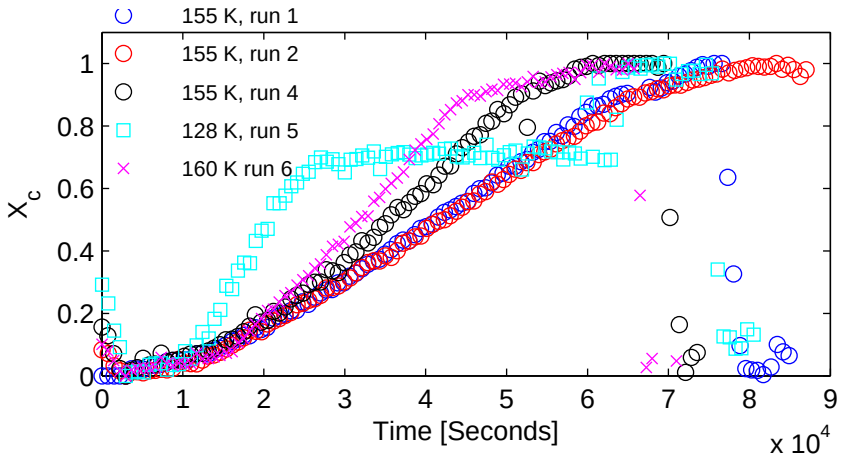

Figure 4.19: The crystallisation kinetics for each run. The similarity between run 1 and 2 is impressive. The run at 128 K is the only one that clearly exhibits a meta-stable phase. The scattered points towards the end are due to the fact that I melt the sample again.

The dielectric results

We had two successful crystallisation runs where both the neutron and dielectric equipment worked. Both the normalised relaxation strength and the Maxwell-Wagner analysis was used to get the crystallinity from the dielectric data.

Fig. 4.20 shows the dielectric data. Surprisingly, the peak of the Debye process does not shift during the crystallisation. This is different from crystallisation runs shown earlier in this chapter. Since the peak frequency does not change I used a quick and dirty way of getting the crystallinity: I simply use $\epsilon"(\nu)$ at a fixed frequency and divide it by the initial value. The frequency used is shown in red in fig. 4.20.

The fact that there is no shift of the peak position also means that I can use the spherical Maxwell-Wagner model, since only the slab model induced a shift. So I fit

$$\epsilon_{comp} = \epsilon_l \frac{2\epsilon_l + \epsilon_c + 2\phi_{\text{spheres}}(\epsilon_l - \epsilon_c)}{2\epsilon_l + \epsilon_c + \phi_{\text{spheres}}(\epsilon_l - \epsilon_c)} \tag{4.8}$$

to the data. Once again ϵ_l and ϵ_c are the dielectric constants of the liquid and crystal respectively, and ϕ_{spheres} is the concentration of the crystal domain.

The results of this procedure is shown fig. 4.20. The fits are good within the interval of the fit. The two methods of getting the crystallinity of the sample agree extremely well for run 6 (fig. 4.20b). For run 4 (fig. 4.20a) there is a difference of up to 30%. But the differences between these two methods are extremely small compared to the difference between the dielectric results and

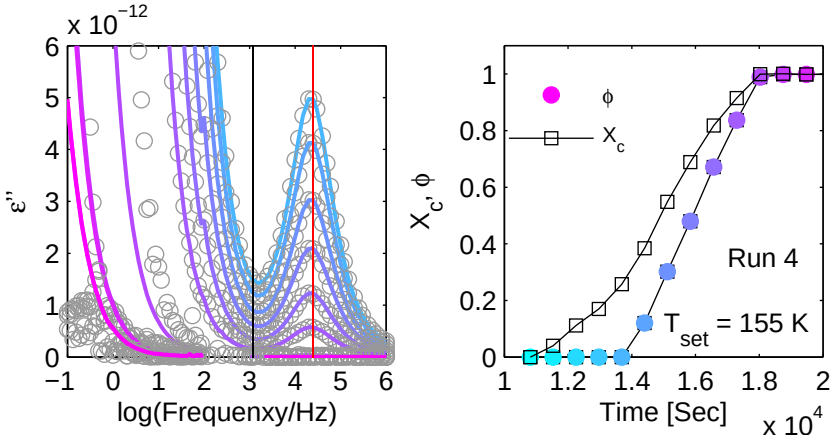

(a)

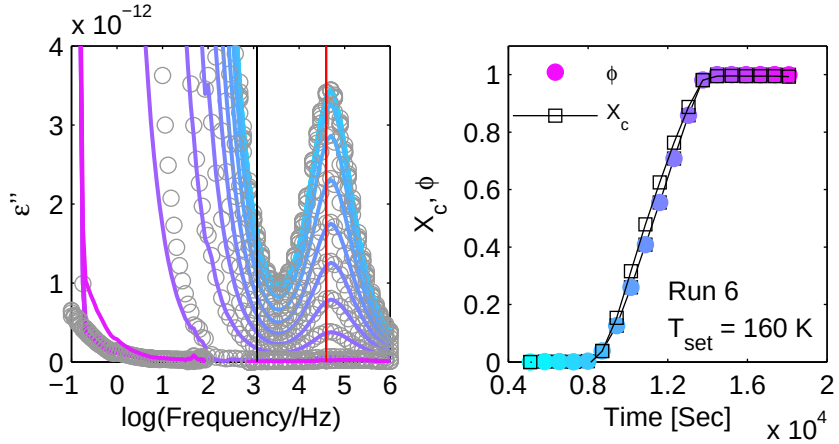

(b)

Figure 4.20: Two methods were used to get the degree of crystallinity from the dielectric data. The first is using $X_c(t) = 1 - \epsilon"(\nu_{\text{fixed}}, t)/\epsilon"(\nu_{\text{fixed}}, 0)$. The red lines in (a) and (b) indicate the frequency used. The second method is using eq. (4.8) to fit the data. The results of these fits are the full lines. The fitting interval used shown by the black line.

the diffraction results, as we shall see in the next section.

Comparing the results from the simultaneous experiments

How does the two techniques compare? The short answer is not well. One way to compare the methods is to plot $X_c(t)$ for both techniques together. This is done in fig. 4.21.

From fig. 4.21 it is clear that the crystallisation kinetics are very different between these two methods. From the dielectric point of view the crystallisation happens almost instantaneously. This is not the case for the X_c from the neut-

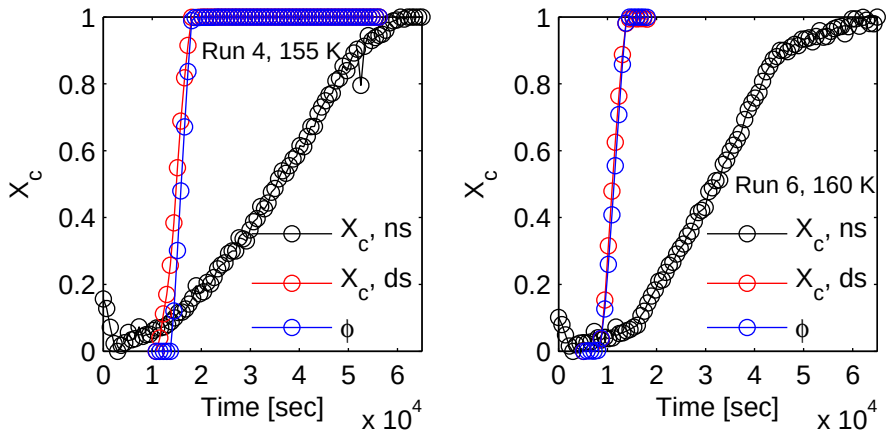

Figure 4.21: Comparing the crystallinity from the neutrons to that of the dielectrics. For the sake of completeness both the normalised relaxation strength and the results from the Maxwell-Wagner analysis are used.

rons. While some difference between the two methods was to be expected, this difference between the apparent crystallisation kinetics of the two techniques is much stronger than what we observed in 2013 and what is reported by Sanz et. al. for iso-propanol [66].

A likely explanation for this is, that the dielectric and neutron measurements are seeing different parts of the sample. The dielectric spectroscopy is only probing the liquid between the electrodes while the neutron are seeing this as well as the liquid in the hollow inner cylinder. The volume of the inner cylinder is much greater than the volume between the electrodes, so the neutron are predominantly seeing the contents of the inner cylinder. So even though the experiments are done simultaneously they are effectively seeing different sample environments. The dielectric see a small amount of sample with a large surface to volume fraction, which is located near the surface of the cell. The neutrons see a larger amount of sample, located at the centre of the cell, with lower surface to volume fraction. The volume to surface ratio may be important for the initialisation of the crystallisation process, as the roughness of the surface may enhance the likelihood of a crystal nucleation and growth.

Furthermore, when the temperature is changed it will drop at the surface faster than at the centre, making the effective temperature protocol slightly different for the two sample environments.

4.10 Concluding remarks

In this chapter I have show some of the difficulties connected to using dielectric spectroscopy to study crystallisation. I have shown that using two different

sample cells leads to different decays of the spectrum, both in terms of how the individual relaxation processes behave, but also in terms of crystallisation kinetics. This makes comparison between techniques impossible – as different experimental techniques often use different sample cells – and seriously limits our capabilities to study crystallisation.

I have proposed a way to account for the differences observed between the cells. The idea is to take into account the fact that crystallisation makes the sample heterogeneous. We model the heterogeneity of the sample using what we now call the Maxwell-Wagner analysis. The Maxwell-Wagner analysis itself introduces fitting parameters and should be tested in it's own right. I have presented preliminary results in this direction, but further development of the sample cell is necessary to test the validity of the Maxwell-Wagner analysis.

The contents of this chapter – especially the simultaneous experiments from 2016 – show just how difficult it is to compare results between different techniques. Following the same temperature protocol is not enough to enable comparison of crystallisation between different techniques. This is because small differences in the cell design may lead to a different effective temperature protocol and have different abilities to initiate the nucleation process. It is necessary to perform the experiments simultaneously and on the exact same sample volume if one wants to compare the results of different techniques when studying crystallisation.

5 | Crystallisation of glycerol-water mixtures

Water is perhaps the most studied liquid on earth and yet much remains to be understood about it's anomalous behaviour. In this chapter I focus on the approach of using glycerol to suppress crystallisation of water to study the liquid-liquid transition (LLT) proposed to take place in super-cooled water. I report on neutron scattering diffraction and small angle scattering experiments that set out to gain a more detailed microscopic understanding of the structural changes that take place in the sample during the transformation, be it a LLT or a crystallisation process.

5.1 Introduction

Over the past couple of years glycerol-water mixtures have attracted a great deal of attention. Researchers have used a variety of different experimental techniques such as neutron scattering [83, 84, 86], Raman [55], dielectric spectroscopy [64], as well as computer simulation [25] to study the mixtures. The motives for studying these mixtures range from industrial application, such as improving cryoprotectants, to fundamental science, such as uncovering new states of matter[56]. But to really understand the interest in this particular mixture of liquids we must first understand the scientific history of the two liquids that make up the mixture: Water and glycerol.

Despite the fact that water covers roughly 70% of the surface of our planet – and that it is necessary to sustain life as we know it – much remain to be understood about water. Water exhibits a number of interesting anomalies when compared to other liquids. For example, the density of water reaches a maximum at 277 K (4°C), expanding both when heated above 277 K (normal behaviour) and when cooled below this temperature (anomalous behaviour).

One glance at the pressure-temperature phase diagram of water (fig. 5.1) should be enough to give an impression of the complex nature of the liquid. I will not go into detail about every aspect of the phase diagram, since this has been the topic off many review papers (see e.g. [4, 5, 14, 16, 51]), but a brief overview will help clarify the interest in the glycerol water mixtures.

At ambient pressure, the melting temperature of water is $273.15K$. Below this temperature the liquid is unstable against crystallisation. However, like all other liquids it should be possible to form a glass, if only the liquid is cooled

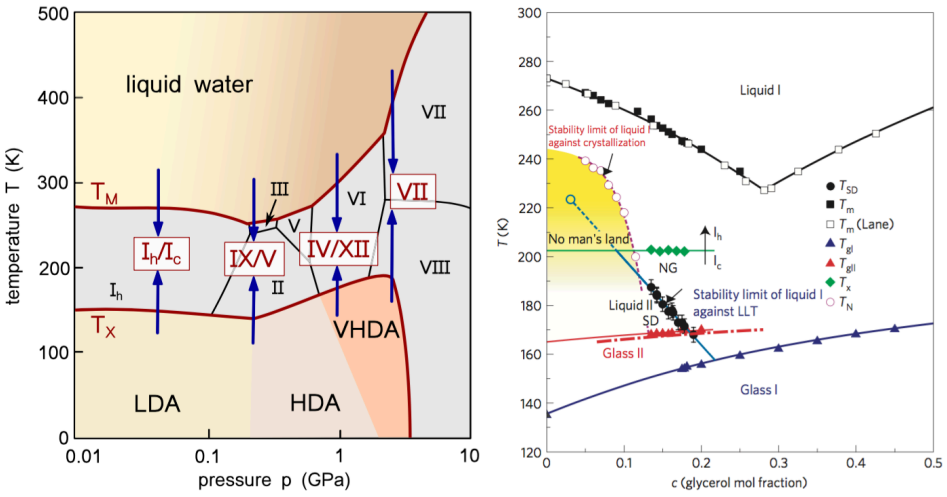

Figure 5.1: a) T-p phase diagram of water, reproduced from [4]. b) T-c phase diagram of glycerol-water mixtures, reproduced from [56].

fast enough. However, the usual method of quenching a liquid using liquid nitrogen or helium is not enough to avoid the crystallisation of water. The lowest temperature reachable by this means is about $235K$, which is not enough to reach the glassy state[16]. This has lead to a series of different approaches such as placing water vapour on a cold surface; quenching small droplets of water; exposing crystalline water to high pressure or radiation damage; confining water; or even mixing water with other liquids[51]. These efforts have yielded a surprising result – it seems that there is not just one amorphous state of water but three. They have been called LDA (low-density amorphous water), HDA (high-density amorphous water), and VHDA (very high amorphous water), see [50] for a review on the three amorphous states of water. As if this was not enough, the phase diagram also contain no less than 16 different crystalline states[92].

Given the above description of the phase diagram it might come as little surprise that a different liquid state has been proposed as well. Ever since a liquid-liquid transition (LLT) was proposed by Poole in 1992 [63] the phenomena has attracted much attention. The transition was first proposed for water which has lead to large collection of scientific literature, but it has also been proposed for other liquids such as n-Butanol[23, 44] and TPP[3, 45].

One of the challenges faced by experimentalists trying to observe the LLT is the location of the LLT in the phase diagram. It happens to be located in the temperature region below the limit of super cooling – a region now often referred to as *No Man's Land*. This means that one is trying to measure properties of a second liquid phase that is also unstable against crystallisation. Consequently

much effort have gone into escaping this No Man's Land, see [16] for a review of recent attempts.

Unlike Water, Glycerol is the archetypical glass former. It has been the subject of considerable and long-standing scientific interest because of its glass forming ability[69]. This is one of the reasons why glycerol-water mixtures have attracted so much attention recently. Glycerol and water mixtures have been used as a means of studying water, assuming that the glycerol does little else than suppress the crystallisation of water, and thus allowing one to venture into No Man's Land.

In 2012 Tanaka et. al. published a paper in Nature stating that a LLT had been observed in glycerol-water mixture for a Glycerol molar concentration of $c_g = 0.178$[56]. Supposedly this mixture can exist as liquid I and transform into liquid II. The transformation mechanism can be either spinodal decomposition or nucleation and growth, depending on the temperature. For spinodal decomposition liquid II spontaneously demixes from liquid I while for nucleation and growth, liquid II nucleates and grows in liquid I. For example, using $c_g = 0.165$ they see nucleation and growth at 180 K and spinodal decomposition at 173 K. They claim that the two liquids are iso-compositional, so liquid I at $c_g = 0.178$ transforms into liquid II at $c_g = 0.178$. This is not straightforward since as the nucleation of crystal cubic ice always goes together with the transformation. The paper includes an impressive number of experiments (SAXS, DSC, Raman spectroscopy, Dielectric spectroscopy and phase contrast spectroscopy) to support it's claim. However, ever since the publication of the Nature paper researches have tried to reproduce the proposed LLT. For instance Popov et al. [64] have studied glycerol/water mixtures in the entire concentration range focusing on dielectric spectroscopy [64]. They conclude that everything they see can be explained by water crystallising, and see no need for the LLT when explaining their observations. Likewise Mishima et al. [81] concluded that a LLT is not seen for the conditions used in [56] using Raman spectroscopy. Surprisingly, they then go on to state that they have observed a LLT at higher pressure.

As I see it two camps are set up – the LLT camp and the crystallisation camp. In the view of the crystallisation camp what appears to be a LLT is really just a mixture of liquid and crystal. Much of the evidence for a LLT in water comes from computer simulations[62, 81], but there are also experimental evidence [56, 81]. It should be noted that the both results have been challanged, on the computer simulation side by [48, 49] and on the experimental side by [64]. The disagreement is not about the validity of the experimental results, but about how they should be interpreted. It may very well be the case that we are not

in a position to exclude either of the interpretations before more data has been gathered.

In this chapter I present the results of neutron diffraction and small angle scattering experiments on the $c_g = 0.178$ Glycerol-Water mixture. The aim was to reproduce the results of [56] and to expand our understanding of the transformation.

5.2 Methods and materials

Three different isotopic mixtures.

Sample A $C_3D_5(OD)_3 + D_2O$. Fully deuterated.

Sample B $C_3H_5(OD)_3 + D_2O$. End groups of glycerol deuterated .

Sample C $C_3D_5(OH)_3 + H_2O$. Back-bone of glycerol deuterated.

All samples had a molar concentration of Glycerol of $c_g = 0.178$. For fully protonated glycerol/water mixture at $c_g = 0.178$ the melting temperature is about 250 K and the glass transition temperature is about 150 K. These numbers may vary slightly between the different isotopic mixtures.

In this chapter I present data from two different experiments.

The neutron diffraction experiments were performed using the beam lime D7 at ILL. With these experiments we study how the local structure changes during the transformation, e.g. see crystal structures as they arise from the liquid phase. Here we used samples A, B and C.

The small angle neutron scattering experiments were performed using the beam line PAXY at LLB. This allow us to study the structural changes at a larger length scale looking for differences in the morphology of the new phase. In this experiment sample B was used.

5.3 Neutron diffraction

5.3.1 Background and aim

These experiments were carried out by Christiane Alba-Simionesco and other in 2013. I was not present. The results of the experiments are included here because they are not published elsewhere and the small angle experiments were done on the basis of these results.

5.3.2 Sample and Temperature Protocol

In these experiments samples A-C were used. The temperature protocol was the following: The sample was rapidly cooled from room temperature down to 131 K at 40 K/min. Then the structure factor was measured for 90 minutes at

selected temperatures on heating. The temperatures used were T = 131, 160, 180, 195, 210, 230, 260, 300 K.

They also performed annealing experiments at 160 K for sample A and B.

5.3.3 Results

In fig. 5.2 I show the structure factor for each temperature on heating. At 130 K the broad diffraction peak, typical for at glass, is seen for both sample A and B. For sample C a gradual increase in the scattering intensity from higher to lower q-values is seen. At 160 K a narrower peak arises for sample A and B, suggesting the emergence of a Bragg peak. For sample C a large increase for $q < 0.4$ is seen together with a depletion of the intensity in the $0.4-0.12$ q-range, but no Bragg peaks are emerging. As the temperature is increased further the Bragg peaks in sample A and B become clearer. Unfortunately there is no data for sample C in this temperature range.

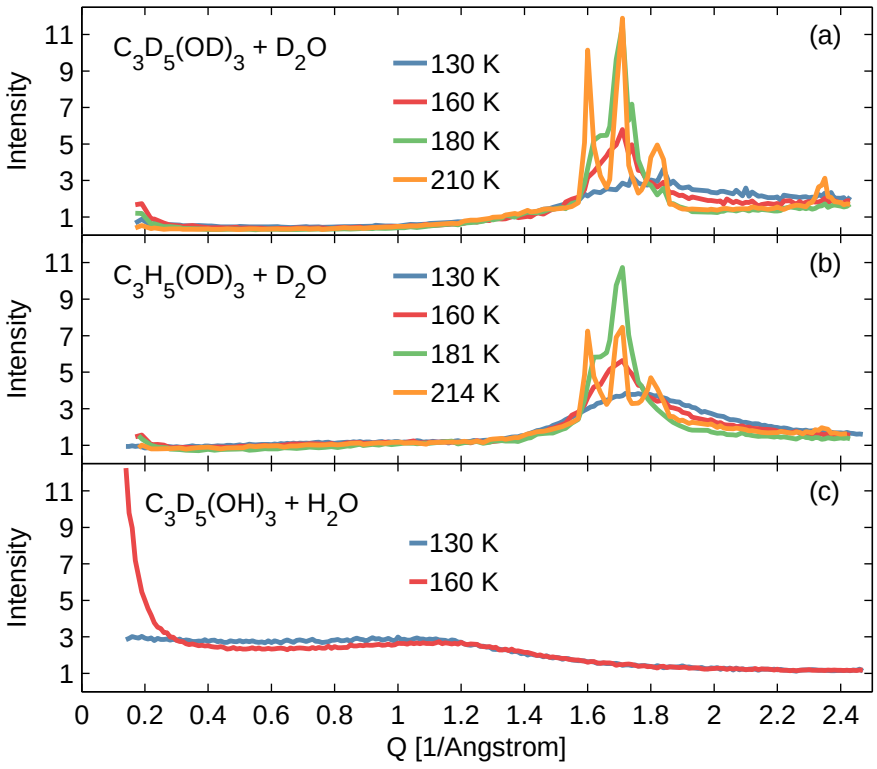

Figure 5.2: The structure factor of glycerol-water mixture during heating after quench cooling to 130 K. In the two isotopic mixture with D_2O the formation of ice is seen as Bragg peaks. For the mixture including H_2O nothing is seen, confirming that it is indeed water crystallising.

The fact that clear Bragg peas are seen in samples A and B, but not in C, suggest that the Bragg peaks are from the Water and not from the Glycerol.

In the low q-range in sample A and B the intensity increase from 130 K to 160 K, but decreases for 180 K and 210 K. This may be because an interface emerges in the sample[77]. In this case it would be the interface between water crystal domains and the remaining liquid. This would explain why the intensity falls back down again when the sample becomes completely crystalline.

The following picture emerges from these results: The Water crystallises and form crystal domains in which there is no Glycerol. This gives rise to an interface between the water crystal domains and the remaining liquid.

In fig 5.3 I show the results of the annealing experiments. Both samples were quenched with 70-90 K/min into the glass. They were then heated to 160 K and kept at this temperature for eight hours. The main purpose of these figures is to show that the sample crystallises at 160 K and that the crystallisation process is slow enough to be followed. This is important for the small-angle experiments in the next section.

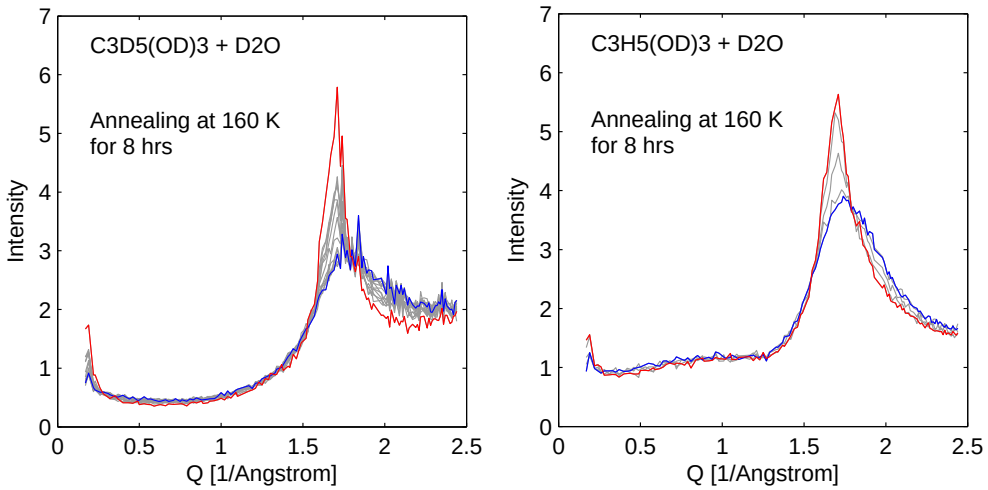

Figure 5.3: During annealing at 160 K a Bragg peak emerges at $\approx 1.71/\text{Å}$ appears.

5.3.4 Concluding remarks

By studying isotropic mixtures of glycerol and water during crystallisation it was shown that the water is in fact crystallising. In all sample we saw an increase in the scattering intensity in the low q-range. This may be caused by the emergence of an interface between the crystal water domains and the remaining liquid. We

have also shown that the crystallisation process can be followed at 160 K. None of the experiments points suggest a liquid-liquid transition took place.

5.4 Small angle neutron scattering

5.4.1 Background and aim

We set out to reproduce the SAXS experiments reported in [56], but using neutron scattering.

5.4.2 Sample and Temperature Protocol

The $C_3H_5(OD)_3 + D_2O$ sample (Sample B) was used because it showed clear signs of crystallisation in the D7 experiments. Three annealing experiments were done. In all cases the sample was quenched to 80 K outside the cryostat before being placed in the pre-cooled cryostat and heated to the annealing temperature. In all cases the annealing temperature was 170 K, but for the second run the sample was kept for 20 hrs at 160 K (with no signs of crystallisation) prior to the annealing at 170 K.

5.4.3 Results

In fig. 5.4 I compare the results of the three different runs.

For the first of the annealing experiments (see fig. 5.4 a)) a clear q^{-2} dependence of the scattered intensity is seen. As the crystallisation progresses a q^{-4} dependence arises in the high end of the q-range. This is exactly what was reported in [56] and the crossover between the two power laws at $q_c \approx 0.5nm$ reported in [56] is also reproduced here.

For the second run (see fig. 5.4 b)), the same crossover with $q_c \approx 0.5nm$ is seen. However, the intensity has an additional feature: There is a clear maximum located around $q_m \approx 0.025$.

The third run (see fig. 5.4 c)) looks similar to the second, with small differences. The position of the maximum has shifted to lower q-values with $q_m \approx 0.01$. Furthermore, the q^{-2} dependence is seen clearly in the early states of the crystallisation, but not towards the end.

Despite annealing at the same temperature three times, two different evolutions of the scattered intensity was observed, suggesting that the long-range ordering is different. One of them agree very well with the results from [56], but the other two are different. A more thorough analysis of the scattered intensity is needed to figure out what the difference between the two evolutions might be. Perhaps it is the difference between spinodal decomposition or nucleation and growth.

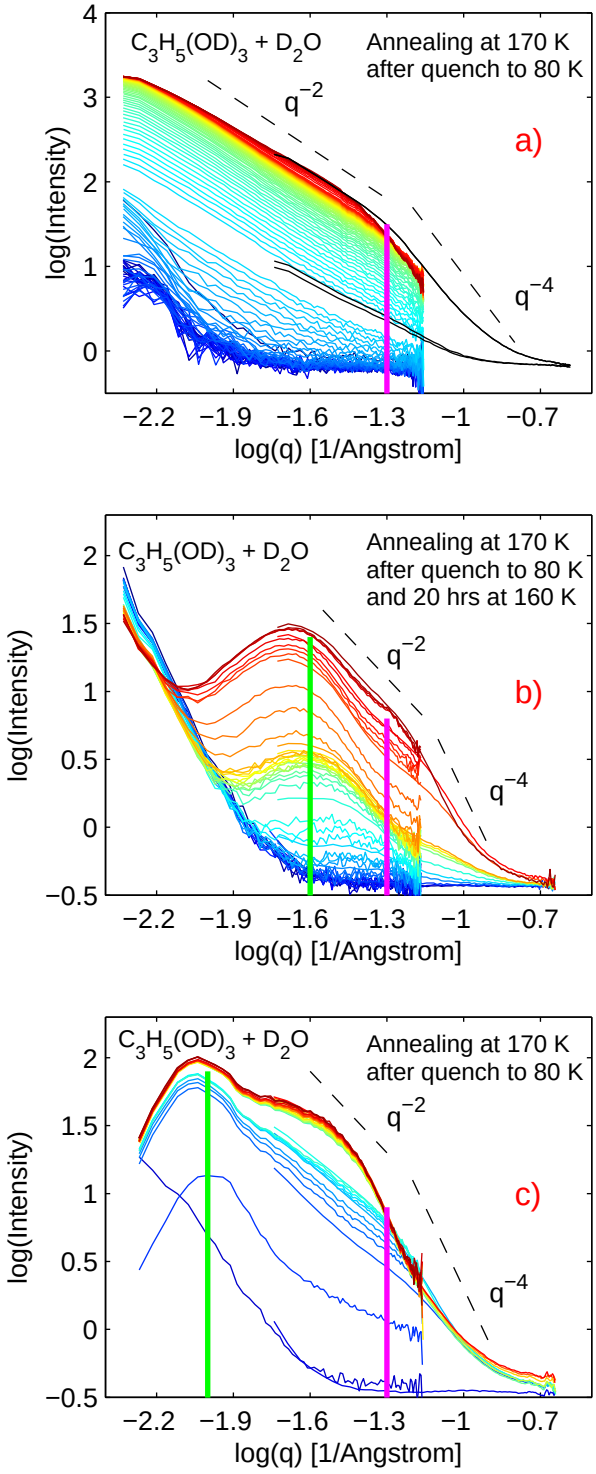

Figure 5.4: Three crystallisation experiments were done at 170 K. In all cases a clear q^{-4} dependence of the scattering intensity emerges. A transition from a q^{-4} to a q^{-2} dependence is seen clearly in a) and b). The bold magenta lines show the position of, q_c, which marks the transition between the two power laws as reported in [56]. A clear maximum is seem in the intensity for b) and c), the position of which is marked with the bold green lines.

5.5 Concluding remarks

From the diffraction experiments it appears that the water crystallises and form crystal domains in which there is no Glycerol. This gives rise to an interface between the water crystal domains and the remaining liquid.

These domains were studied using small angle neutron scattering. The SAXS results from [56] were reproduced, but a different evolution of the scattered intensity was seen in two out of three cases.

Perhaps Tanaka's claim that the transformation is iso-compositional is wrong. When the water starts to crystallise it segregates the sample into domains of crystal water and domains of liquid glycerol/water mixtures. These domains of liquid mixture then contain a higher concentration of glycerol, since some of the water is locked up is crystal ice. So we are seeing the crystallisation of water as well as an increasing glycerol concentration in the remaining liquid. The seperation of the water from the glycerol may happen as nucleation and growth or as spinodal decomposition depending on the temperature.

6 | Supra-molecular clusters in n-butanol

This chapter focuses on the dynamics of n-butanol in the 300 K to 120 K temperature range. Results from dielectric spectroscopy and neutron-spin-echo data are compared and different physical models are used to explain the observations.

6.1 Introduction

Monohydroxy alcohols have been studied widely due to the existence of a relaxation process slower than the structural relaxation, the so called Debye process. This process has been linked to the presence of supramolecular structures, but much is still unknown about the nature of the clusters [15]. In this chapter I will combine neutron-spin-echo with dielectric spectroscopy to study the dynamics of n-Butanol in a wide temperature range.

I will start this chapter off with some historical remarks about the Debye process in sec. 6.2. After having given the experimental details in sec 6.3, I will explain how I fitted the dielectric data (sec. 6.4) and neutron-spin-echo data (sec. 6.5). I will then compare the results from the two methods in sec. 6.6. After having summarised the results from the experiments I use three different models in an attempt to get to the microscopic origins of the relaxation processes. This is done in secs. 6.7-6.9. In sec. 6.10 I show some preliminary results on the q-dependence of the relaxation times from neutron-spin-echo. Finally in sec. 6.11 I give some closing remarks.

6.2 Historical remarks

The Debye process has a long history, as is evident from the title of the 2015 publication [15]: *Structure and dynamics of monohydroxy alcohols: Milestones towards their microscopic understanding, 100 years after Debye.* Understanding the history of the Debye process will help us understand the different interpretations currently in play.

The Debye process has it's name because the relaxation process is well described by a model Debye developed in 1913. The model was developed to describe polarisation phenomena and relaxation in liquids. To test his model he measured on monohydroxy-alcohols. In most mono-hydroxyl alcohols the Debye process is extremely intense, often about ten times as intense as the structural relaxation. The model described the main relaxation in these liquids well, but attempts to estimate the hydrodynamic radius of 1-propanol was off by more than a factor of 1000 [15]. So already early on this suggested that

supra-molecular cluster were at play in these liquids.

Already in the early 1940s it was suggested by Oster and Kirkwood that the Debye process could be attributed to the formation of supra-molecular chains [15]. In [30] Gainaru et. al. suggested a mechanism by which such supra-molecular chains could form. According to the model, the chains move by molecules joining and leaving the chain, rather than by displacing the entire chain. For this reason the model was called the transient chain model, supposedly to emphasise that they constantly change. In this model the chains form by the OH groups bonding to each other. This means that the joining and leaving of molecules happens on a timescale of τ_{OH}, but the chain's end-to-end vector changes on a slower timescale of τ_D. The model will be described in more detail in section 6.9.

In [75] Silrén et. al. studied the structure and dynamics of the liquid 1-propanol by neutron spin echo, NIR, NMR, and dielectric spectroscopy. They measured the intermediate scatting function at the main- and pre-peak of the structure factor. They found that the relaxation times at the main-peak data agreed well with the relaxation times calculated on the basis of viscosity data, while the relaxation times at the pre-peak data agreed with the relaxation time, τ_{OH}, as measured by NMR. These findings are qualitatively in agreement with the transient chain model. This is because the pre-peak may be connected to supra-molecular clusters in the liquid[22] and according to the transient chain model, the dynamics of the supra-molecular clusters are controlled by the joining and leaving of the molecules, which happen on the timescale of τ_{OH}.

In [76] Singh et. al. observe a considerable decrease of the Debye peak amplitudes of 5-methyl-3-heptanol with temperature. They suggest that the changes with temperature are due to the hydrogen-bonded structures changing from chains at low temperature (180 K) to rings at high temperature (215 K). This put an emphasis on using the temperature dependence of the spectrum to uncover the microscopic origins of the Debye relaxation process.

In [11] Bauer et. al. report on a anomalous behaviour at 250 K of the NIR peak absorbance, chemical shift data and dielectric relaxation strength for six mono-alcohols. They suggest that 250 K marks a transition in the hydrogen-bonded network. They explain the observation in terms of hydrogen bond co-operativity, an effect which increasingly stabilises the supramolecular structures below this temperature. The essence of the paper is that something fundamental changes about the hydrogen-bonded network at high temperatures.

So in summary: The Debye process is generally associated with hydrogen-bonded structures but the microscopic origin of this dominant dielectric process is not entirely clear. Furthermore, at high temperatures it is unclear what

happens to the hydrogen-bonded structures.

6.3 Experiment and materials

The dielectric spectroscopy measurements were done using two different setups using. The range from 10 mHz to 1 MHz was measured using RUC's custom build setup, described in [37], while the range from 1MHz to 1 GHz was measured using the alpha analyser from Novo Control.

The neutron spin echo measurements were done at MUSES at LLB using fully deuterated n-Butanol. The time window of the instrument covers 0.8 ps - 3 ns. The experimental resolution function was measured using a piece of quartz as the sample.

6.4 Fitting the dielectric spectra

The dielectric spectrum was measured at 42 temperatures between 120 K and 280K. A subset of these curves are shown in fig. 6.2. The temperatures between 120-134K were already presented in Paper A and the general attributes of the dielectric spectrum of n-Butanol was described in chapter 4 as well.

Here I focus on the how the spectra changes in a larger temperature range. In the low temperatures range three relaxation processes are quite easily distinguished from one and another. However, as the temperature is increased the processes start to merge due to different temperature dependencies of the relaxation times.

In fig. 6.1 I show the time-temperature-superposition for the dielectric data. The Debye process does not seem to change shape in the studied temperature range. However, both the α and β-process change. The results from the fits will help us quantify these changes.

As the temperature is increased it becomes increasingly difficult to distinguish between the processes. This makes fitting the spectrum at high temperatures complicated so ones has to be careful when interpreting the results of such fits. Since the relaxation processes move closer and close to the end of the frequency window, it becomes increasingly difficult to fit the spectrum. I have chosen to use use the same fitting routine for all spectrums above 134 K, but we do not know that the shape parameters are constant in this temperature range. For example, what I see as the alpha process moving to higher frequencies could be the alpha process changing its shape parameters. For this reason relying only of dielectric spectroscopy in this temperature range is dangerous.

That being said, I will now describe how the fitting was done. First I split the data into two temperature ranges. In the temperature range where I think the three processes can be distinguished I used the method described in chapter

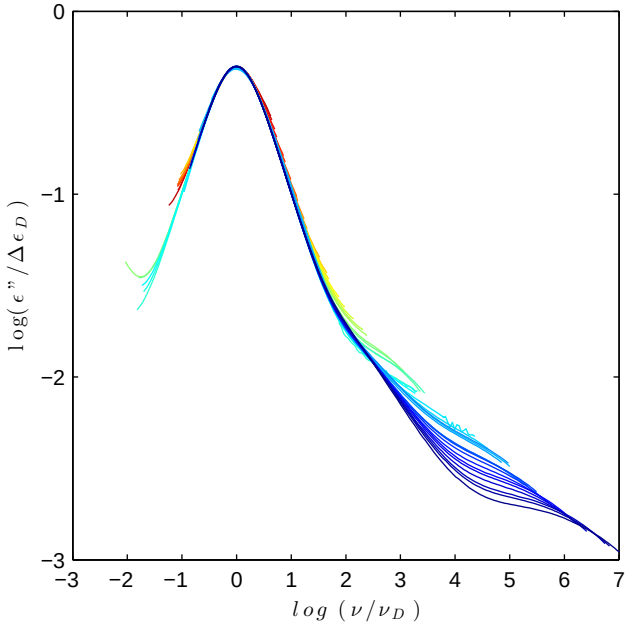

Figure 6.1: Time-temperature-superposition of all the dielectric spectra. The curves have the same colours as in fig. 6.4, so blue is the lowest temperature and red is the highest.

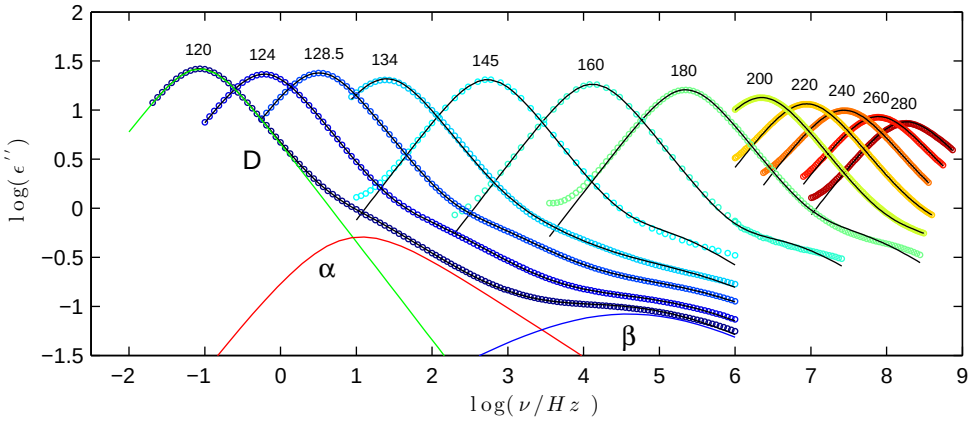

Figure 6.2: A subset of the 42 measurements made in the 120 K to 280 K temperature range. For 134 K and below I fit three relaxation processes to the spectrum. Above I no longer fit the β process. For details about the fitting procedure see the main text.

4 and Paper A, with the one distinction that the Debye stretching parameter is kept constant at 1. So all the shape parameters are kept constant throughout the temperature range. At 134 K and above I no longer fit the β process, but

otherwise the fitting procedure is the same. This is why the fits are so bad for the last couple of points on the high frequency side above 134 K. I tried fitting the β process in this temperature as well, but the resulting parameters behaved unsystematically.

Each spectrum is shown together with the results of the fit for visual inspection in fig. 6.3. The fitting parameters are shown in fig. 6.5 together with the results from the neutron spin echo and will be discussed in sec. 6.6.

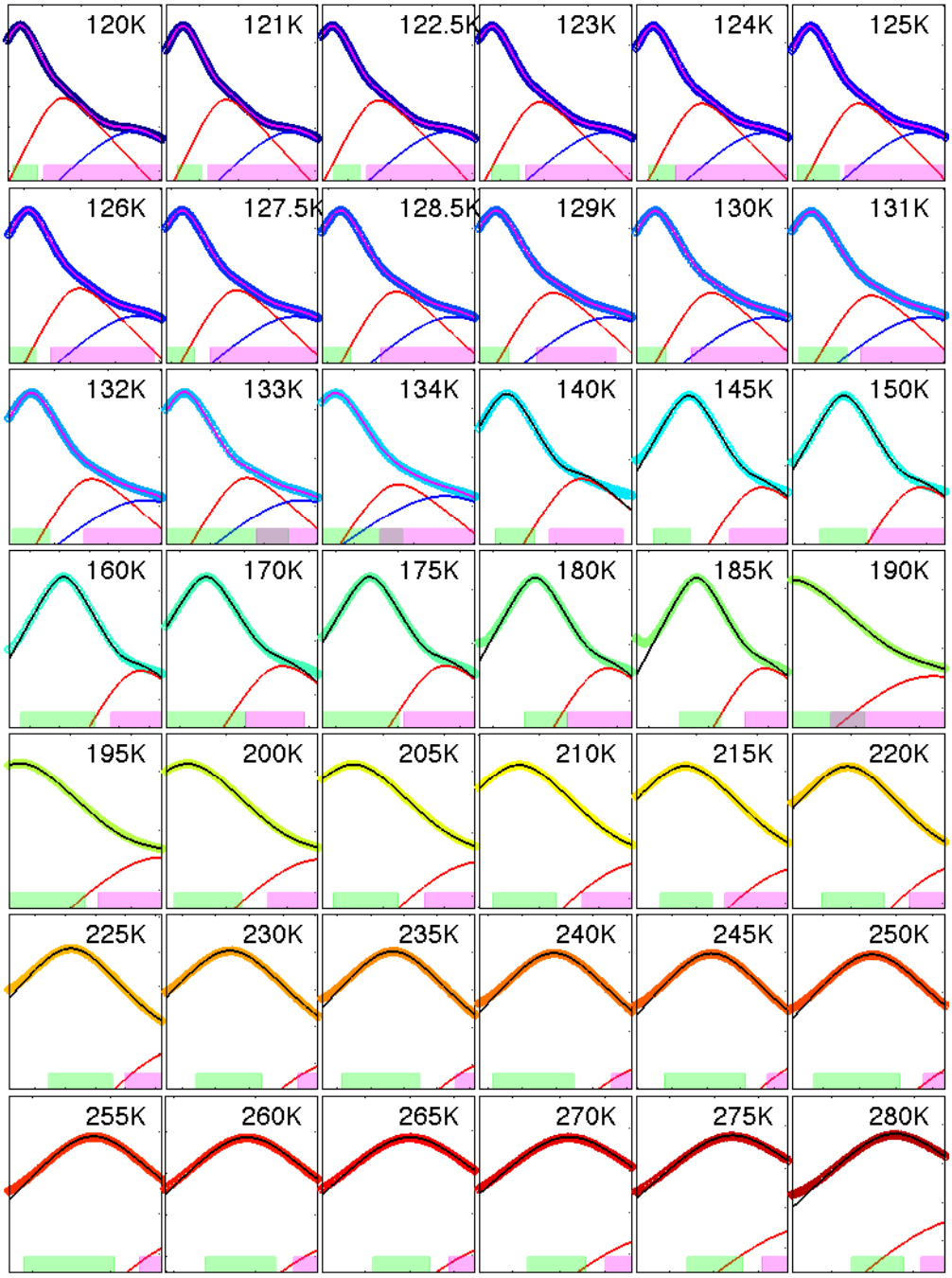

Figure 6.3: Overview of fits for 42 temperature. Purely for visual inspection of the fit quality. Numbers and legends have been removed to save space. See fig 6.5 for the numbers. Transparent boxes show the frequency interval used for fitting the Debye (green) and Alpha+Beta (magenta)

6.5 Fitting the intermediate scattering function

Since the dielectric data becomes unreliable at high temperatures it is useful to compare the results to other experimental techniques. This is why I have carried out the neutron-spin-echo experiments.

The intermediate scattering function was measured at $q = 1.5\text{Å}^{-1}$ for nine temperature between 280 and 175 K. The data are shown in fig. 6.4 together with fits using a stretched exponential:

$$\frac{S(q,t)}{S(q,0)} = A \exp\left[-\left(\frac{t}{\tau}\right)^{\beta}\right] \tag{6.1}$$

Where τ is the relaxation time, A is the amplitude, and β is the stretching parameter. β was set to 0.5 since it has been suggested that this is the proper value to use for the structural relaxation[58]. So only τ and A were fitting parameters.

The resulting relaxation time are shown in fig. 6.5 (a). The results will be discussed together with the dielectric results in the next section.

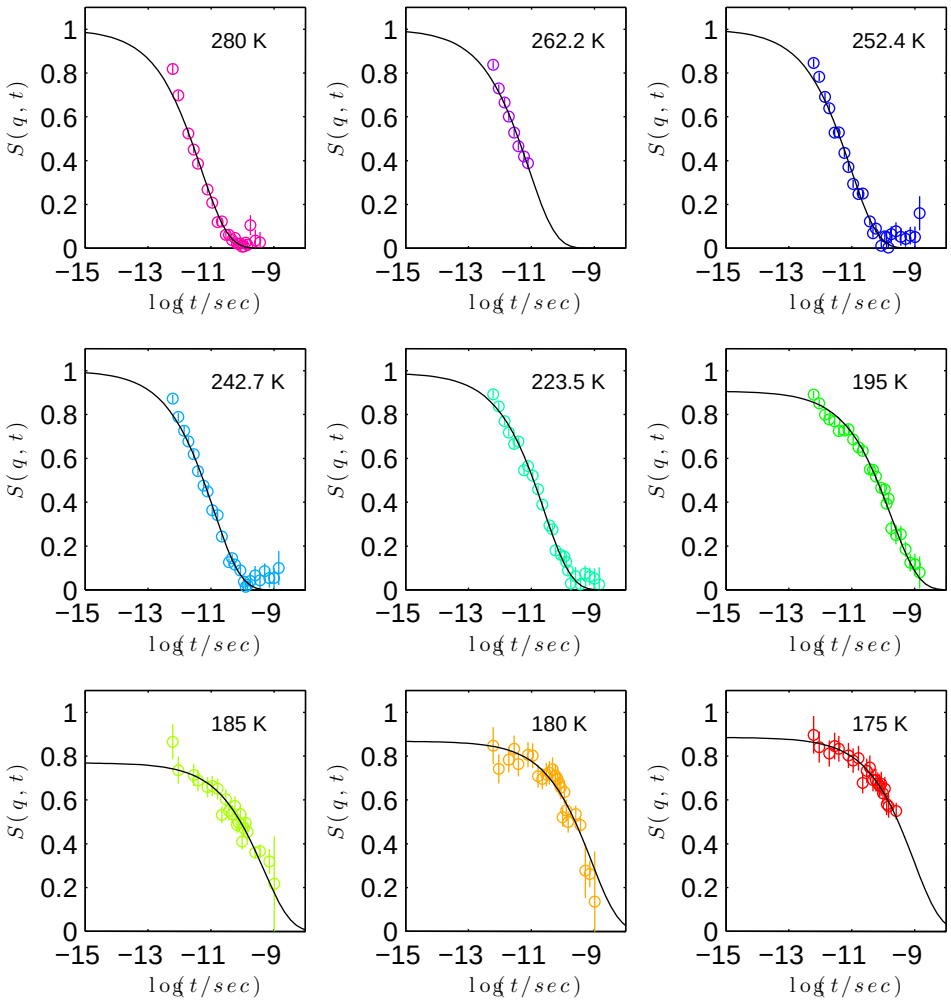

Figure 6.4: TThe intermediate scattering function was measured at $q = 1.5\text{Å}^{-1}$ for nine temperature between 280 and 175 K. The fitted relaxation times are shown in fig. 6.5

6.6 Comparing the NSE and DS results

Fig. 6.5 (a) show the relaxation time as a function of inverse temperature for both the dielectric and neutron spin-echo-measurements. To these I have add the relaxation of the OH group from NMR experiments [30].

I have also added the Maxwell relaxation time, τ_M, calculated using the Maxwell model. The Maxwell model relates the viscosity, η, and the shear modulus, G_∞, to the relaxation time, τ_M, through $\tau_M = \eta/G_\infty$. I was not able to find the shear modulus for n-Butanol, so I have used the bulk modulus, K_∞, instead. The exact value used is $K_\infty = 1.13\ GPa$[1]. The bulk and shear moduli are usually different, so I call the relaxation time calculated from the viscosity for τ_η going forward.

τ_η agrees well with the relaxation times from the neutron-spin-echo experiment. Similar results have been reported in [75] for 1-Propanol.

In 6.5 (b) I show the relaxation strength of the three dielectric processes. In the 120-134 K interval the relaxation strength of the beta-process increases while that of the alpha-process decreases. As the temperature increases above roughy 210 K the strength of the alpha-relaxation increases whereas the strength of the Debye relaxation decreases. This relation between the structural and Debye relaxation strength has been reported in [30] as well.

In fig. 6.5 (c) I show the shape parameters. They were all kept locked during the fitting, I show them here simply for easy reference.

The relaxation strengths of the alpha and beta processes become similar, but their relaxation times remain separated by more than a decade. For the Debye and alpha processes it is the opposite: Their timescales merge, but the relaxation strengths remain separate by more than a decade.

In fig. 6.6 I have multiplied τ_α from NSE and τ_η by a factor of five. With this shift they agree well with the dielectric data. It is not uncommon for different response function to lead to different absolute values of the relaxation time, but the temperature dependence should be the same [39]. This is possibly what we see here. Above 195 K the fits are not delivering reliable results for the alpha-process. So perhaps what looks to be the merging of τ_D and τ_α in the dielectrics is a consequence of fitting a limited frequency window rather than something physical.

[1]The value is taken from `http://www.kayelaby.npl.co.uk/general_physics/2_2/2_2_2.html`

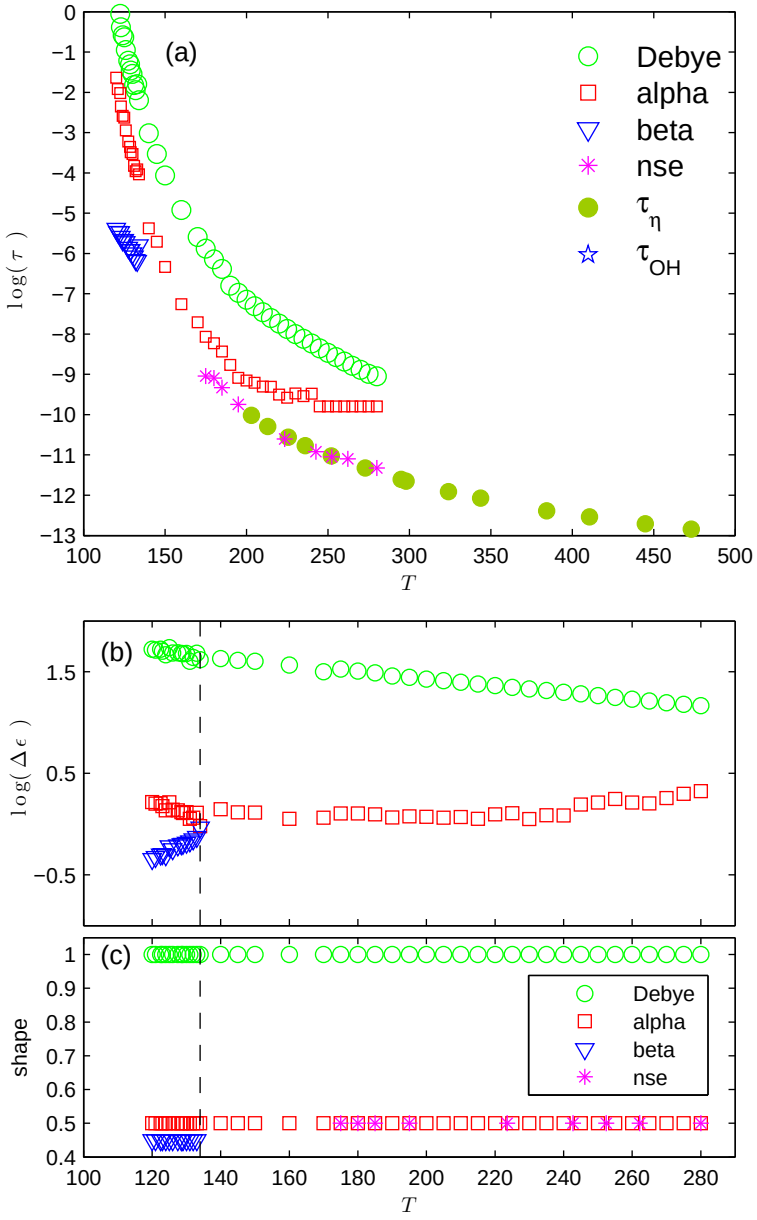

Figure 6.5: a) The relaxation time for the three relaxation processes from the dielectric measurements together with the relaxation time of the NSE. The relaxation time from the viscosity data, τ_η. τ_{OH} from NMR[30] is included as well. b) The relaxation strength, $\Delta\epsilon$, from the fits as a function of temperature. c) The shape parameters used in the fits. They are here to remind the reader that they are constant during the fits.

In the following section I will look into several different models so see if they help us get to the microscopic origins of the observations described above.

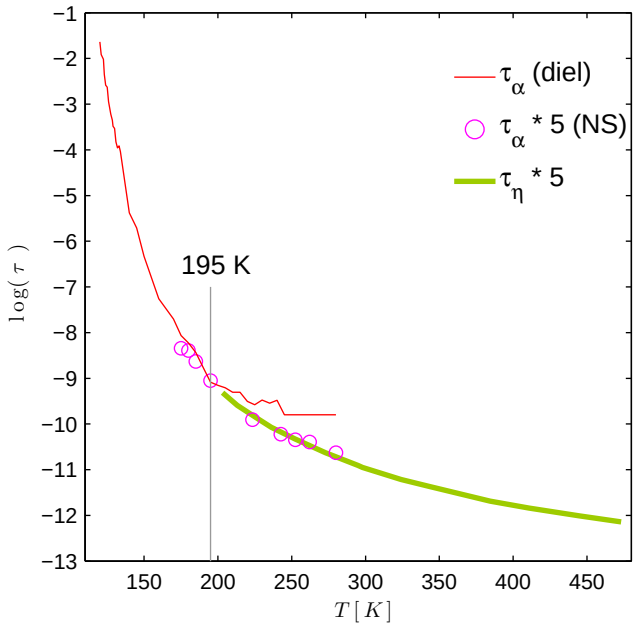

Figure 6.6: Comparing the relaxation times from dielectric spectroscopy (DS) and neutron-spin-echo (NSE) to τ_η. I have multiplied τ_α from NSE and τ_η by a factor of five to make them collapse with τ_α from DS. The collapse is quite convincing. I take this to mean that above 195 K the fits are not delivering reliable results.

But before we dive in let us first consider what scattering experiments tell us about the the length scales involved in liquid n-Butanol. The structure of n-Butanol has been studied extensively using x-ray [21, 36, 73, 87] and neutron [19] scattering. The main peak is located around $q = 1.3$ 1/Å and the prepeak – which may be connected to supra molecular structures in the liquid phase – is located around $q = 0.6$ 1/Å. A quick estimate length scales is reached by using $d = 2\pi/1.3 \approx 5$Å and $d = 2\pi/0.6 \approx 10$Å. We should keep these numbers in mind when we go onto discussing the different explanations.

6.7 Changing alignment: The Kirkwood correlation factor

The decrease in the strength of the Debye process could be interpreted in the light of the Onsager relation:

$$\frac{(\epsilon_s - \epsilon_\infty)(2\epsilon_s + \epsilon_\infty)}{\epsilon_s(\epsilon_\infty + 2)^2} = \frac{\rho N_a}{9k_B T\epsilon_0 M}\mu^2 g_K \tag{6.2}$$

with ϵ_s and ϵ_∞ being the static and instantaneous limits of $\epsilon(\omega)$. N_a is Avagado's number,ρ is the density, M is the molar mass, k_B is Boltzmann's constant, and ϵ_0 is the permittivity of free space. Finally g_K is the Kirkwood correlation factor. The Kirkwood correlation factor takes into account the short range orientational correlations of the dipoles. If $g_K = 1$ these orientational correlation are negligible, where as $g_K > 1$ implies a parallel alignment of the dipoles and $g_K < 1$ implies an anti-parallel alignment[42]. In this view the decrease in the relaxation strength of the Debye process could be understood as arising from a decrease in the Kirkwood correlation factor. This could happen if the structures goes from a parallel alignment to something different. This would explain the decrease in the relaxation strength of the Debye processes, but it doesn't explain anything about the α processes, or anything about the relaxation time of the Debye process.

6.8 Changing supra-molecular size: The hydrodynamic radius

If we think of the Debye process as being connected to supra-molecular structures, then their size can bed estimated by considering the hydrodynamic radius – the hydrodynamic radius being the effective radius a macro molecule has when submerged in a liquid. The reasoning behind this approach is the following: If the supra-molecular molecular cluster get small, then that would lead to a shorter Debye relaxation time.

First a few words about the equation we will be using: The Stokes-Einstein equation:

$$D = \frac{k_B T}{6\pi\eta R_H}. \tag{6.3}$$

It was derived to explain Brownian motion of macro molecules submerged in a liquid, such as pollen in water. It relates the diffusion constant, D, of a diffusing entity with radius R_H, to the viscosity, η, of the liquid the diffusing entity is submerged in.

Applying the Stokes-Einstein equation to molecular liquids to connect the diffusion coefficient of the molecules comprising the liquid to the viscosity of the

liquid does not make a lot of sense conceptually. However, it is often used for exactly this purpose and it works remarkably well [24].

Taking the diffusion data from [47] and the viscosity from [57] leads to $R_H \approx 1.6$Å at $298K$. The van der Waals radius of n-Butanol is 2.93 Å [24], so the estimate is off by little less than a factor of 2. In [24] Edward summarises the corrections one must apply to the Einstein-Stoke equation when dealing with small molecules (say around 5 Å). The correction is the following:

$$D = \frac{k_B T}{n\pi\eta R_H (f/f_0)} \tag{6.4}$$

where f is the friction constant of an ellipsoid, f_0 is the friction constant of a sphere and n molecule specific *correction factor* [24]. For n-butanol the values $n = 4.81$ and $(f/f_0) = 1.06$ are given for n-Butanol [24], which amounts to using 5 rather than 6 in eq. (6.3).

If we want to estimate the hydrodynamic radius based on dielectric data we have to connect the diffusion constant to the relaxation time. This can be done using the following expression [12]:

$$R_H = \left(\frac{k_B T}{4\pi} \frac{\tau_{rot}}{\eta} \right)^{1/3} \tag{6.5}$$

Where τ_{rot} is the rotational relaxation time, which connects to the rotational diffusion constant. Eq. 6.5 was used in [12] to estimate R_H for the 4M3H molecule, another mono-alcohol. They find that using $\tau_{rot} = \tau_\alpha$ underestimate the R_H while using $\tau_{rot} = \tau_D$ yields an estimate in good agreement with the literature.

In fig. 6.7 I show the results of using eq. 6.5 with the different relaxation times to estimate the hydrodynamic radius. The Debye relaxation time as well as the dielectric τ_α seem to be converging towards the van der Waals radius of n-Butanol of 2.93. But this in the temperature range where the results from the dielectrics are unreliable, and neither the NSE τ_α or τ_η delivers good results in this case.

So simply thinking in terms of the size of the supra-molecular clusters is probably too simplistic.

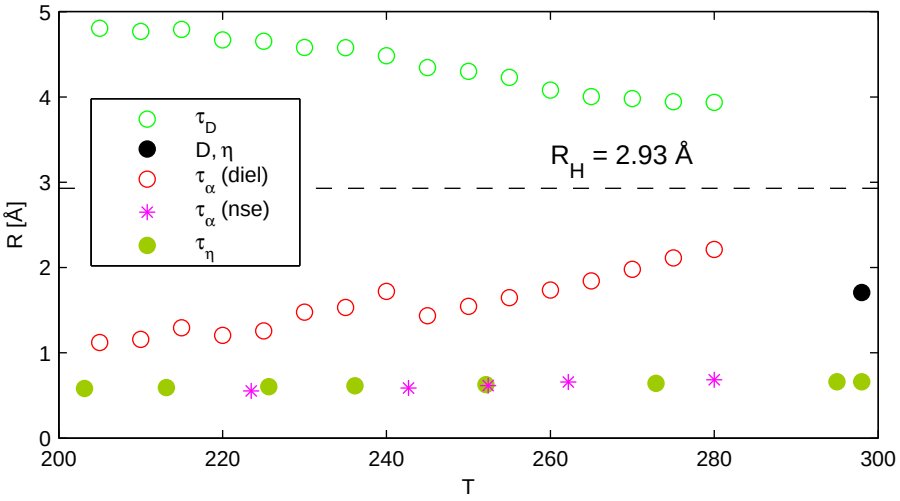

Figure 6.7: Estimates of the hydrodynamic radius using different approaches. Putting the viscosity and diffusion constant into eq. (6.3) gives a too smal estimate. Relying on the relaxation times and eq. (6.5) likewise gives a too small estimate for the alpha process. Using the Debye process yields sizes of 4Å and above

6.9 Alignment and size: The transient chain model

In the last two section we have looked at alignment of the dipoles and size of the supra-molecular clusters as possible explanations for the observations presented in this chapter. In this section I will describe a model that includes both alignment and size. The model is the transient chain model. I will present the model here as it was first described in [30]. The essence of the model is that the molecules form supra-molecular chains and that these chain move, not as a connected chain like a polymer, but by molecules joining and leaving the chain. This way one achieves chain motion without displacing the chain as a whole.

Assuming free molecules are transported to and away from the chain on a timescale of τ_α, then the average lifetime of a molecule within a chain of length N is of the order $N\tau_\alpha$. Since the OH groups are essentially fixed while the molecules are in the chain it follows that the relaxation time of the OH group, τ_{OH}, should be of the same order of magnitude as $N\tau_\alpha$. This leave us with a way of estimating the size of the chains using only the relaxation times:

$$\frac{\tau_{OH}}{\tau_\alpha} \approx N. \tag{6.6}$$

Considering the neutron spin echo results from earlier one can wonder about which τ_α to use. In fig. 6.8 I used τ_α from dielectric spectroscopy, neutron-spin

echo, and τ_η calculated on the basis of the viscosity. They lead to very different estimates of the chain lengths.

Another way to estimate the chain length within the framework of the transient chain model is to use the relaxation strengths. This argument is longer. The conclusion is reached by considering the decomposition of the dipole moment of the supra-molecular chain into a part parallel to the chain, $\mu_{||}$, and a part perpendicular to it, $\mu_\perp$.

The dipole moment of the alkyl chain will be perpendicular to the supra-molecular chain and most of the dipole moment of the alkyl chain lies with the OC bond. Since $\mu_{OC} \approx 0.74D$ [2] and the dipole moment of the entire n-Butanol molecule is $\mu \approx 1.7D$ (both values are from [30]) a rough estimate of $\mu_\perp$ becomes

$$\mu_\perp \approx \frac{\mu}{2}. \tag{6.7}$$

Likewise the dipole moment parallel to the supra-molecular chain is

$$\mu_{||} \approx \mu_{OH} \approx 1.5D \approx \mu. \tag{6.8}$$

The end-to-end dipole moment of a chain of length N is thus expected to be sum of all the $\mu_{||}$ contributions:

$$\mu_{\text{end-to-end}} \approx N\mu_{||} \approx N\mu \tag{6.9}$$

Since in general, the relaxation strength and dipole moment are related though

$$\Delta\epsilon_x \propto N_x\mu_x^2, \tag{6.10}$$

we can use this to relate the estimates of the decomposed dipolar moment with relation to the chain to the relaxation strengths.

Now, if we assume that all molecules are participating in both the Debye and alpha-process, we can assume that the number of molecules participating in the alpha-process is N times larger than the number of chains participating the the Debye processes, that is

$$N_\alpha = NN_D. \tag{6.11}$$

To be clear here N_α is the number of molecules participating in the α-relaxation processes and N_D is the number of chains participating the the Debye relaxation process. Finally N is still the average number of molecules in a chain.

[2] The unit Debye, D, is not the SI unit, but for the present purpose of getting rough proportionalities it does not matter.

Using eqs. (6.7), (6.10) and (6.11) the relaxation strength for the α-process becomes:

$$\Delta\epsilon_\alpha = N_\alpha \mu_\perp^2 = \frac{N_\alpha \mu^2}{4} = \frac{N N_D \mu^2}{4} \tag{6.12}$$

Likewise, using eqs. (6.8) and (6.10) for the Debye process we have:

$$\Delta\epsilon_D = N_D \mu^2_{\text{end-to-end}} = N_D N^2 \mu^2 \tag{6.13}$$

With this we can estimate the chain length by using the ration of the relaxation strength of the Debye and α-process:

$$\frac{\Delta\epsilon_D}{\Delta\epsilon_\alpha} \approx 4N \tag{6.14}$$

With this we now have two ways of estimating the average number of molecules in transient chain. In fig. 6.8 I show the estimate for the entire temperature range.

Of course, these estimates can be no better than the estimates of τ_α and $\Delta\epsilon_\alpha$. As we have already pointed out, these are hard to estimate as the temperature increases. Then there is the question of of using τ_α and $\Delta\epsilon_\alpha$ to represent the structural, reorientational, dynamics. At least at higher temperatures we saw that the viscosity does not agree with the relation times from fitting the spectrum.

Despite these problems, the model gives us an interesting way of thinking about the observation presented in this chapter. The dielectric strength of the Debye process decreases with temperature because the length of the chains become shorter.

However, the model also predicts that no signal should be seen in mechanical spectroscopy since *"the transient nature of the chain does not couple to the internal stress field"* [30]. But relaxation modes corresponding to the Debye peak have now been observed for mono-aocohols[29, 31]. So perhaps the chains are not so transient after all.

6.10 q-dependence of the relaxation time

In sec. 6.2 I mentioned the results from 1-Propanol [75], that the dynamics change when studied at different length scales. One can wonder how the relaxation time changes with the length scale in a simpler case than a hydrogen-bonded liquid. This was done by de Gennes [20] in 1959. He considered hard spheres and concluded that the q-dependence of the relaxation time connected to the collective dynamics (the coherent intermediate scattering function) should follow the structure factor divided by q^2, that is

$$\tau(q) \propto \frac{S(q)}{q^2} \tag{6.15}$$

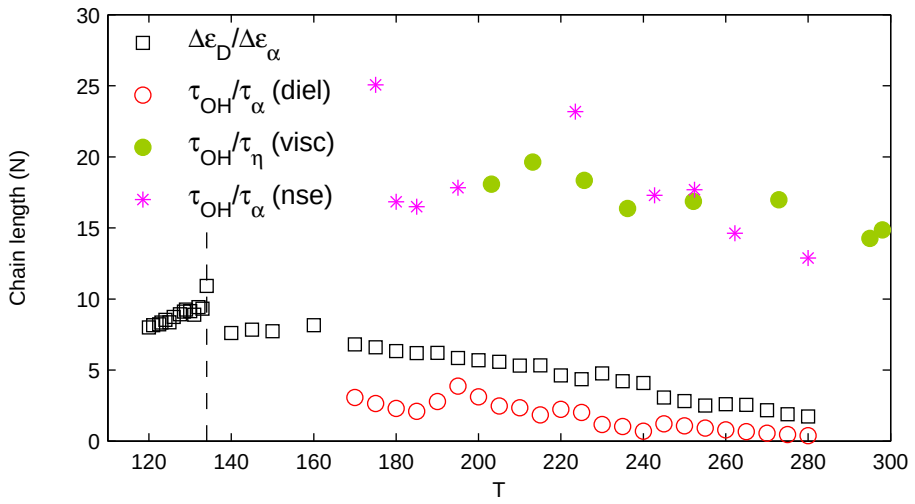

Figure 6.8: Estimates of the chain length using eq. (6.6) and eq. (6.14). Estimates vary widely depending on which τ_α is used.

This effect is now called de Gennes *narrowing* because the half-width-half-height of the dynamic structure factor, $S(q,\omega)$, has a minimum where the static structure factor has its first maximum – $S(q,\omega)$ becomes narrower close to the maximum of the static structure factor.

But not only that, if one thinks in terms of the intermediate scatting function represented as a stretched exponential,

$$S(q,t) = A \exp\left(-\left[\frac{t}{\tau}\right]^{\beta}\right), \tag{6.16}$$

then both the stretching, β. and amplitude, A become function of q and they should follow the static structure factor as well.

Experimentally, this effect has been observed by coherent quasi-elastic neutron scattering on simple atomic fluids like noble gases, such as argon [78, 88, 89], on molecular deuterium [13] and also on liquid metals, such as lead [79] and Rubdium [18]. Experimentally, only a few studies of the wave vector dependence of the alpha-process in supercooled liquids [54, 82] indicate that a narrowing is present.

Since dynamics at different length scales is at the heart of the discussions about Debye process, we wanted to see to what extent the simple model used by de Gennes holds for a system such as n-Butanol with its hydrogen-bonded supramolecular structures. This would give a context for understanding the slow dynamics reported for 1-Propanol at the pre-peak – is it de Gennes narrowing

or evidence for supra-molecular clusters? – and possibly confirm the observation in another similar liquid.

We measured the q-dependence of the intermediate scatting function for two different temperatures. Making such measurements can be extremely difficult because the the polarisation, and thus the quality of the intermediate scatting function, can change a lot with q. Two different temperatures were used to compensate for the relative small time window (3 decades) covered by MUSE at LLB.

The results are shown in fig. 6.9 together with fits and the resulting fitting parameters. While the quality of the data leaves something to be desired, we can at least say that τ, β, and A qualitatively follow the static structure factor. While the results are preliminary, it does suggests that the structural relaxation in n-Butanol is not so different from what is expected for a hard sphere system.

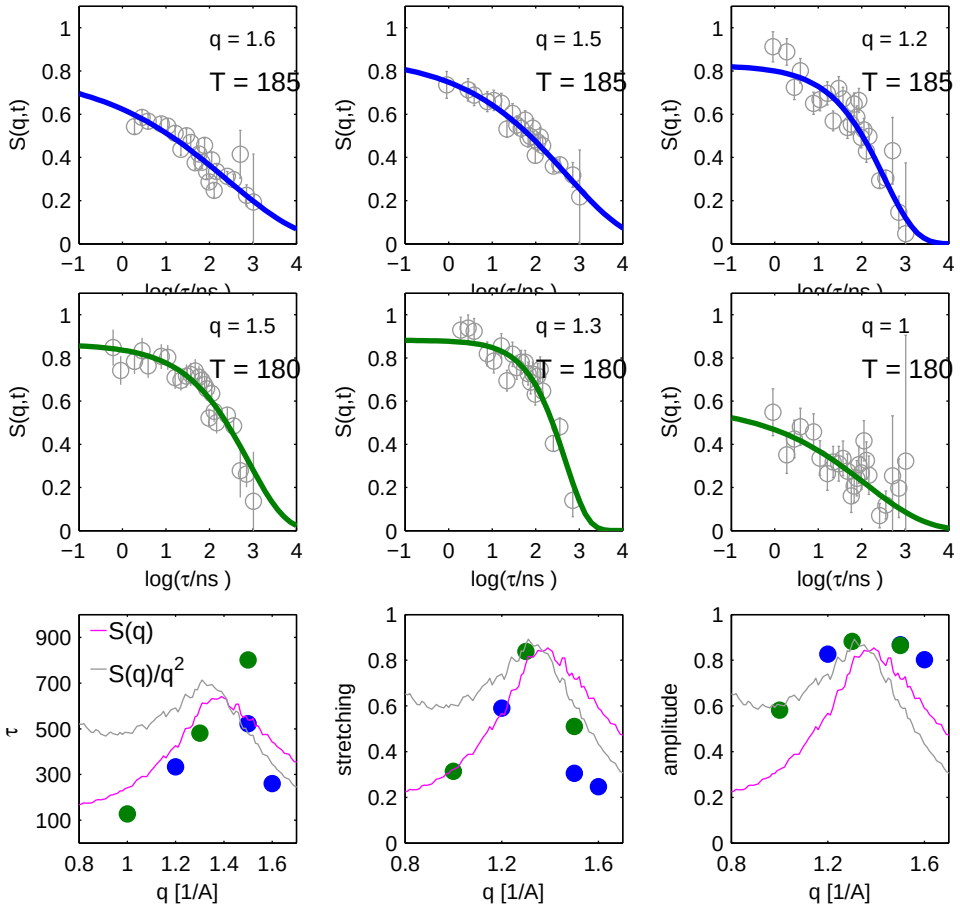

Figure 6.9: Looking at the q-dependence of the relaxation time for the temperatures 185 K (blue) and 180 K (green). τ, β and A qualitatively follow the static structure factor.

6.11 Concluding remarks

In this chapter I have presented results from dielectric spectroscopy and neutron-spin-echo experiments on n-Butanol. I have focused on how the neutron-spin-echo measurements can help us understand the temperature dependence of the dielectric fitting parameters.

The main observations can be summarised as follows: The relaxation times from the intermediate scattering function at the main peak agree with the relaxation times calculated using the viscosity data. If multiplied by a factor of five both become natural extension of the temperature dependence of the alpha-process from dielectrics in the 120-195 K range. This suggests that above roughly 195 K the fitting parameters for the alpha process can not be trusted. Above 195 K is exactly the the temperature region where the Debye and alpha-process merge. Our neutron-spin-echo results suggests that this merging may be a consequence of fitting a limited frequency window, rather than something physical.

Several different physical models were used to try to get a microscopic understanding of what takes place in the liquid as the temperature is increased. We covered alignment of dipoles through the Kirkwood correlation factor; the size of the supra-molecular clusters with the hydrodynamic radius; and we analysed the fitting parameters in terms of the transient chain model. Neither of the models were able to account for all the observations.

It seems that we do not fully understand the microscopic origins of the Debye process in mono-alcohols just yet. When studying the high temperature dynamics of these interesting system dielectric spectroscopy should be complimented with other experimental techniques.

Finally I presented preliminary results on the q-dependence of the relaxation time in n-Butanol. The results are qualitatively in accordance with the de'Gennes narrowing which was originally developed for spheres. It is surprising that this result appears to be valid even for a molecular liquid with hydrogen bonding. It suggests that the structural relaxation for a hydrogen-bonded molecular liquid is not so different from the structural relaxation in a hard sphere system.

7 | Supra-molecular structure in glycerol and glycerol-water mixtures

In this chapter neat glycerol and glycerol water mixtures are studied with shear mechanical spectroscopy. A new feature is revealed in the shear mechanical spectrum. The data are combined with data from the literature in order to infer a coherent physical picture of the dynamics of the mixtures

7.1 Introduction

Supercooled glycerol is one of the most studied liquid in the fundamental research on the glass transition. Moreover supercooled glycerol plays a crucial role in nature and industry because of its potential as a cryoprotectant. There is general consensus that the hydrogen-bond network in glycerol plays a crucial role both for its dynamics and structure. The interaction of water with this network is likewise of great interest, both from a fundamental point of view, and in terms of understanding the mechanisms behind the antifreeze effect of glycerol.

Glycerol-water mixtures have been divided into three concentration intervals on the basis on their ability to super-cool[64]. In the high glycerol range, $0.28 < c_g < 1$, the sample can be cooled and reheated without crystallisation. In the intermediate range, $0.15 < c_g < 0.28$, the sample can be super-cooled with a quick quench, but it crystallises upon heating. Finally in the the low concentration range, $0 < c_g < 0.15$, the sample crystallises easily upon cooling.

Within the last 5 years it has been found that supramolecular structures in hydrogen-bonding systems can give rise to a low frequency signal in broad band shear mechanical spectroscopy[2, 29]. These low frequency modes are slower than the structural relaxation associated with the calorimetric glass transition, and resemble the rouse modes in polymers. The mechanical signature was originally found in mono-alcohols[29], but has also been seen in an amines[2]. To our knowledge this type of mode has not before been identified in polyalohols. In this chapter we study neat glycerol and glycerol water mixtures with shear mechanical spectroscopy.

In this chapter we are studying the high glycerol concentration range to avoid crystallisation.

7.2 Sample preparation and characterisation

For this study six mixtures of glycerol and water were prepared. The glycerol was purchased from Sigma Aldrich at $\geq$ 99% purity. The water was tapped from a Arium®611 ultrapure water system.

The molar concentrations of a binary mixture of two substances x and y is defined as

$$c_{x,mol} = \frac{n_x}{n_x + n_y}. \tag{7.1}$$

with n denoting the mols of the substance. The samples were prepare by weight, so the molar concentration was calculated as:

$$c_{g,mol} = \frac{m_g/M_g}{(m_g/M_g + m_w/M_w)}, \tag{7.2}$$

with M being the molar mass of the substances. In our case we are dealing with glycerol ($M_g = 92.09382\ \mathrm{g\,mol^{-1}}$) and water ($M_w = 18.01528\ \mathrm{g\,mol^{-1}}$). Thus, the mixture of $c_{g,mol} = 0.8$ was made by mixing 6.3152 g of glycerol with 0.3091 g of water. See table 7.1 for a complete overview of how the mixtures were made. Concentrations are usually given as molar concentration but sometimes they are given as volume or mass concentration. Therefore I have given these concentration as well in table 7.1. After mixing the sample were stirred for at least 4 hours before being loaded into the sample cell.

In table 7.2 I give the boiling, melting and glass transition temperature for the mixtures. We have measured the glass transition temperature of four of our mixtures using thermalization calorimetry[40]. In fig. 7.1 I compare T_g for different techniques.

The results from thermalisation calorimetry agree with T_g from. The glass transition temperature from our shear mechanical measurements agree with data provided by Catalin Gainaru, using the same technique, but a different experimental set-up.

Table 7.1: Overview of the concentrations used. α_V is the thermal expansion coefficient in the $15 - 20°C$ range, from [1]. It is included here because we use it to correct the data from the PSG.

m_{glycerol}	m_{water}	$c_{\text{g, mol}}$	$c_{\text{g, vol}}$	$c_{\text{g, wt}}$	$\alpha_V \cdot 10^4$
6.3183	0	1	1	1	6.1
6.3152	0.3081	0.7999	0.9419	0.9533	6.2
6.3045	0.5282	0.7004	0.9046	0.9228	6.2
6.3082	0.8225	0.6000	0.8589	0.8846	6.1
6.3230	1.2324	0.5002	0.8024	0.8365	6.2
6.3388	2.8766	0.3012	0.6362	0.6878	5.8

Table 7.2: Relevant temperatures for each mixture. The boiling temperatures, T_b, and the melting temperature, T_m, are from [1]. The glass transition temperature from DSC, $T_{g,dsc}$, is from [10]. The glass transition temperature from shear, $T_{g,dsc}$, is from the results presented in this chapter.

$c_{\text{g, mol}}$	T_b $[K]$	T_m $[K]$	T_g, dsc $[K]$	T_g, shear $[K]$
1	563	291	196	183
0.7999	437	281	191	179
0.7004	412	275	189	175
0.6000	406	269	187	172
0.5002	399	259	181	170
0.3012	286	231	170	161

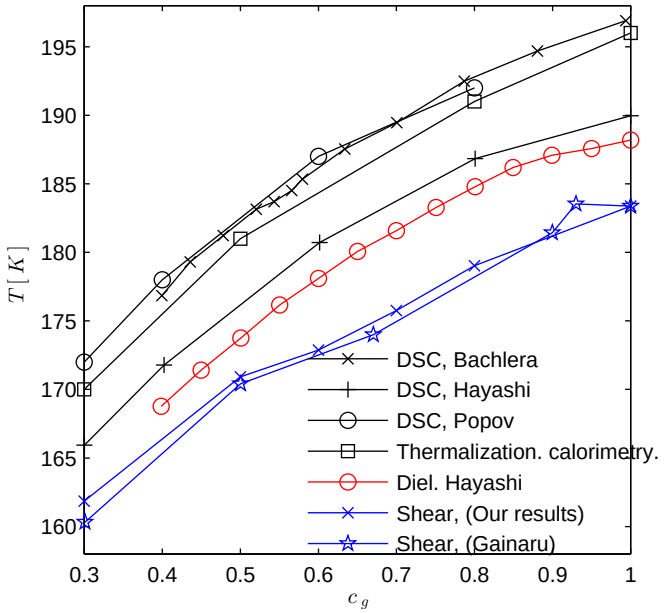

Figure 7.1: Comparing glass transition temperatures from different techniques. Bachlera is from [10]. Hayashi DSC data is from [33]. Popov data is from [64]. Hayashi dielectric spectroscopy data is from [33] where the T_g is defined using $\tau(T_g) \equiv 100s$. The same definition of T_g is used for the shear data

7.3 Results

The complex frequency dependent shear modulus $G^*(\nu) = G'(\nu) + iG''(\nu)$ of the glycerol water mixtures was measured using the piezoelectric shear-modulus gauge (PSG) technique[17]. In this section I will present the results of these measurements. First I will explain how the relevant physical properties were extracted from the data.

7.3.1 Extracting physical properties from the data

The following properties are extracted from the data:

The loss peak frequency, ν_{max}: By fitting a second order polynomial to the points around the loss peak I cen get the loss peak frequency as the position of the maxima of the polynomial. The points used for the fitting are shown as grey circles in panel b) of the figures on the following pages.

Relaxation time, τ_{max}: Since the data are plotted on a frequency axis, I need to convert the loss peak frequency to angular frequency if I want to compare the results to the relaxation time used in the different response functions. So $\tau_{max} = 1/2\pi\nu_{max}$.

$G"(\nu_{max})$: I calculate the maximum of the same second order polynomial used to find ν_{max}. This value is primarily used for making time-temperature-superposition plots.

The instantaneous shear modulus, G_∞: This I get by fitting the entire spectrum with the following generalisation of the BEL (Barlow, Erginsav, Lamb) model which is sometimes referred to as the extended Maxwell model[38]:

$$G^*(\omega) = \frac{G_\infty}{1 + (i\omega\tau)^{-1} + q(i\omega\tau)^{-\alpha}} \tag{7.3}$$

where G_∞ is the instantaneous shear modulus, τ is the relaxation time and α is a stretching parameter.

The Maxwell relaxation time, τ_M: The Maxwell Time is given by:

$$\tau_M = \frac{\eta_0}{G_\infty}. \tag{7.4}$$

Where I use G_∞ found as described above. η_0 is found by taking the maximum of $\eta'(\omega)$ with $\eta'(\omega) = G"(\omega)/\omega$.

The glass transition temperature, T_g: I have experimented with three ways of getting T_g. The first to is to do a linear extrapolation of the relaxation

times to $\tau = 100s$. For this the relaxation times for the three lowest temperatures were used. The second method is to fit the entire temperature range with a VFT equation and using this fit to extrapolate to $\tau = 100s$. The last of the three methods defines T_g to be at $\tau = 10s$ rather than $\tau = 100s$, which allow us to do a linear interpolation between the measures relaxation times, so we avoid any extrapolation.

$G'(T_g)$: Since we had three ways of estimating T_g we also have three ways of estimating this number. For the extrapolations I fit a straight line the the the lowest three temperature points, and use this to extrapolate to T_g. When using the T_g at $\tau = 10s$ I do a linear interpolation instead.

In figs. 7.2-7.7 I show the results of extracting these properties. In the next couple of section I will analyse how these properties change with varying water content and temperature.

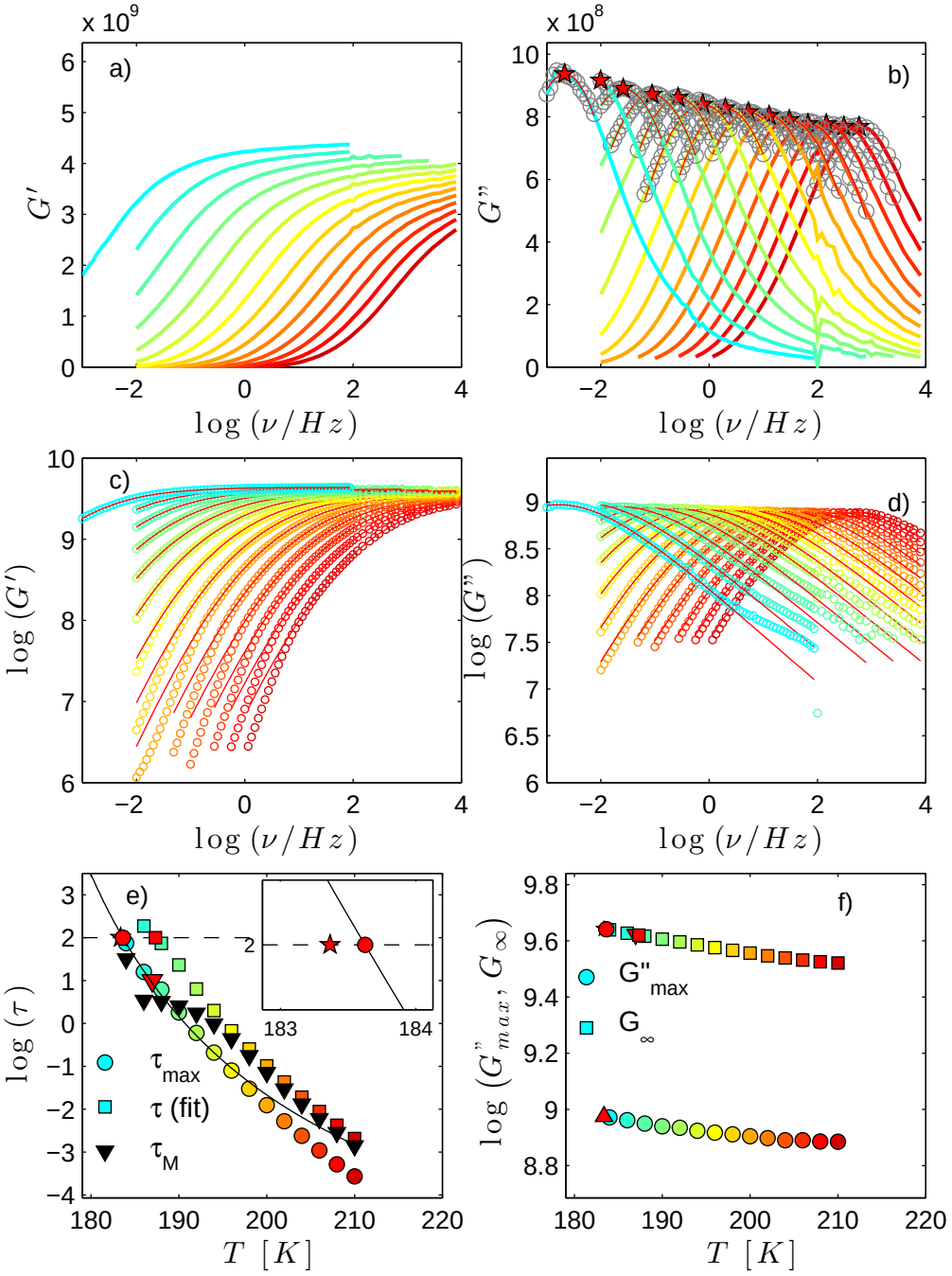

Figure 7.2: Overview of the results on neat glycerol. From the data I extract properties as explained in section 7.3.1. a) real part of G^*. b) Imaginary part of G^*. The grey circles indicate the pointes used for fitting the second order polynomial and the red pentagons show the loss peak frequency, ν_{max}, and $G"(\nu_{max})$. c) and d) show the real and imaginary part of G^* on a log scale. The red lines are fits using extended Maxwell model. e) The relaxation times extracted. The inset shows the results of using the different extrapolations methods to get T_g. f) $G"_{max}$ and G_∞ as a function of temperature. $G_\infty(T_g)$ is shown in red with the pentagon and circle being T_g from the linear and VFT extrapolation respectively. The downward pointing triangle is the interpolation using $T_g|_{\tau=10s}$.

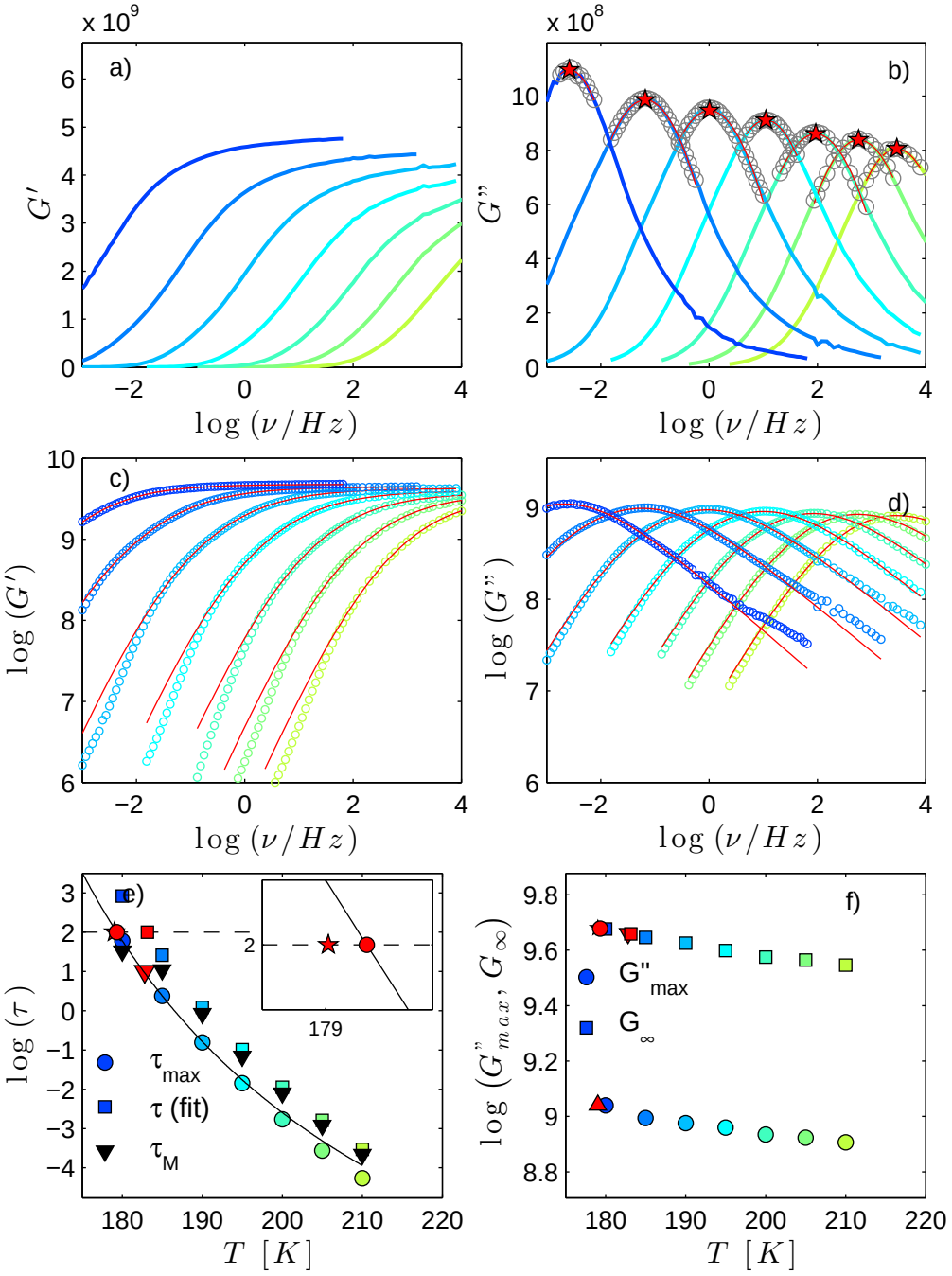

Figure 7.3: Overview of the results on the $c_G = 0.8$ mixture. From the data I extract properties as explained in section 7.3.1. a) real part of G^*. b) Imaginary part of G^*. The grey circles indicate the pointes used for fitting the second order polynomial and the red pentagons show the loss peak frequency, ν_{max}, and $G"(\nu_{max})$. c) and d) show the real and imaginary part of G^* on a log scale. The red lines are fits using extended Maxwell model. e) The relaxation times extracted. The inset shows the results of using the different extrapolations methods to get T_g. f) $G"_{max}$ and G_∞ as a function of temperature. $G_\infty(T_g)$ is shown in red with the pentagon and circle being T_g from the linear and VFT extrapolation respectively. The downward pointing triangle is the interpolation using $T_g|_{\tau=10s}$.

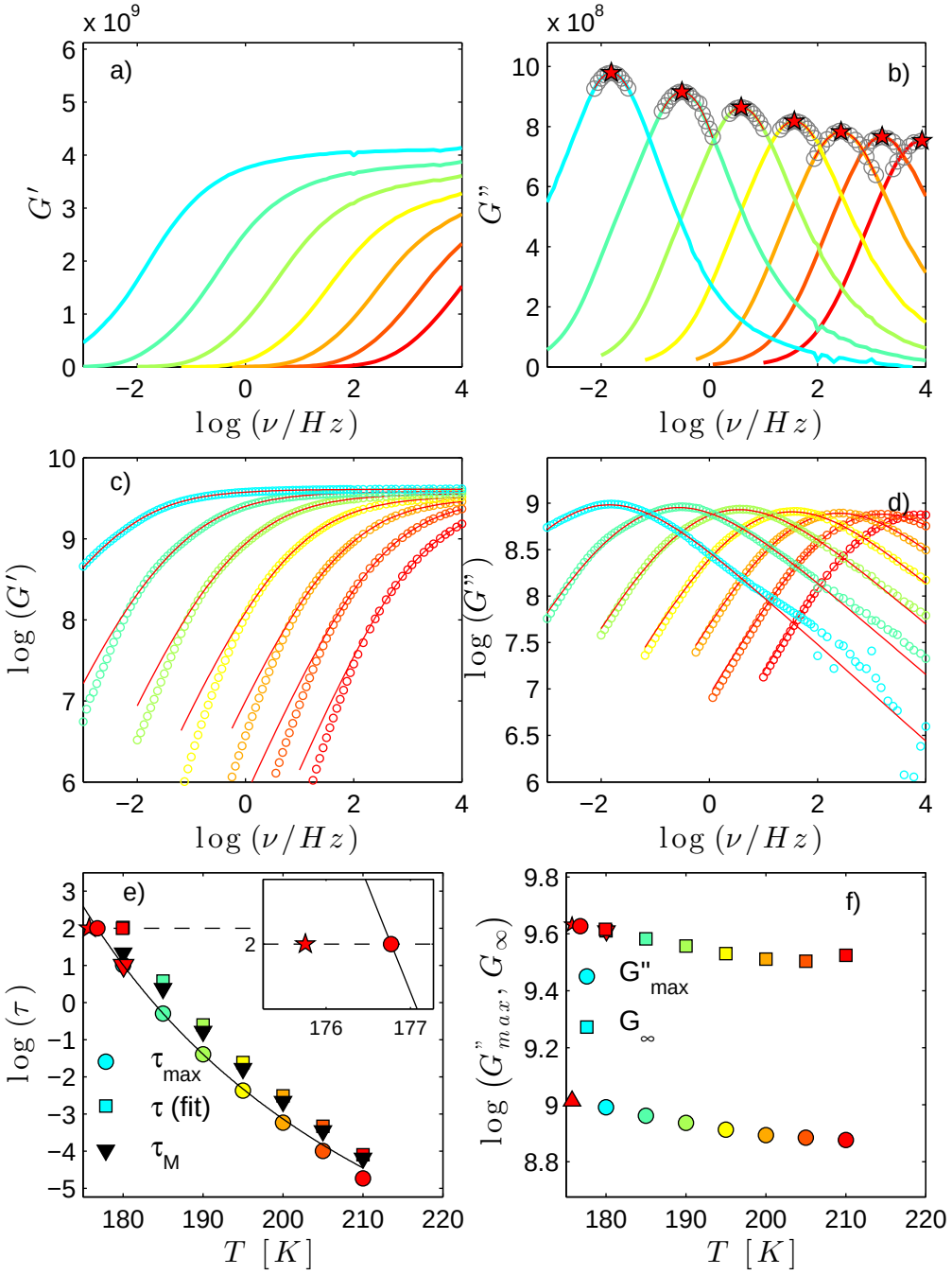

Figure 7.4: Overview of the results on the $c_G = 0.7$ mixture. From the data I extract properties as explained in section 7.3.1. a) real part of G^*. b) Imaginary part of G^*. The grey circles indicate the pointes used for fitting the second order polynomial and the red pentagons show the loss peak frequency, ν_{max}, and $G"(\nu_{max})$. c) and d) show the real and imaginary part of G^* on a log scale. The red lines are fits using extended Maxwell model. e) The relaxation times extracted. The inset shows the results of using the different extrapolations methods to get T_g. f) $G"_{max}$ and G_∞ as a function of temperature. $G_\infty(T_g)$ is shown in red with the pentagon and circle being T_g from the linear and VFT extrapolation respectively. The downward pointing triangle is the interpolation using $T_g|_{\tau=10s}$.

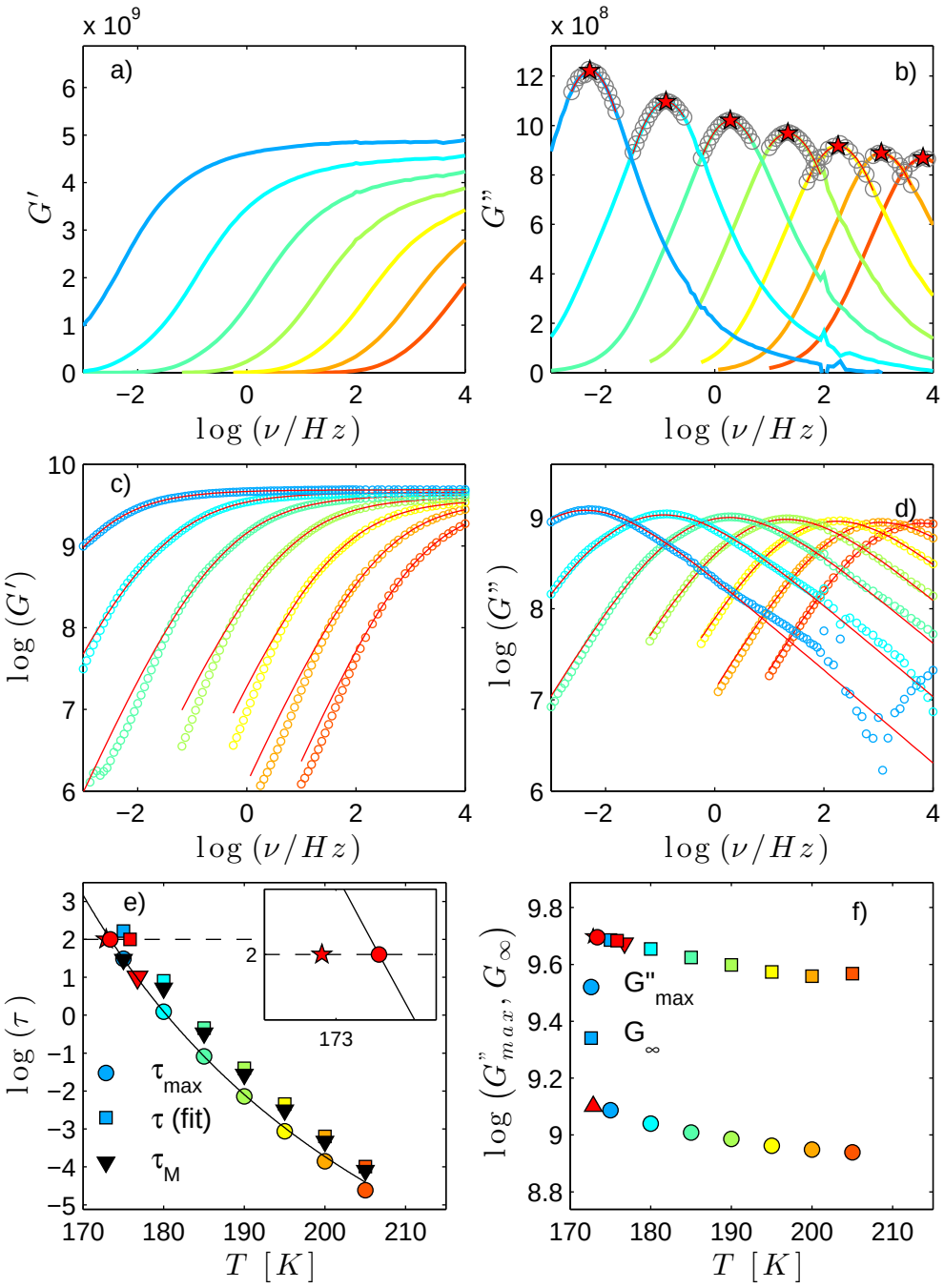

Figure 7.5: Overview of the results on the $c_G = 0.6$ mixture. From the data I extract properties as explained in section 7.3.1. a) real part of G^*. b) Imaginary part of G^*. The grey circles indicate the pointes used for fitting the second order polynomial and the red pentagons show the loss peak frequency, ν_{max}, and $G"(\nu_{max})$. c) and d) show the real and imaginary part of G^* on a log scale. The red lines are fits using extended Maxwell model. e) The relaxation times extracted. The inset shows the results of using the different extrapolations methods to get T_g. f) $G"_{max}$ and G_∞ as a function of temperature. $G_\infty(T_g)$ is shown in red with the pentagon and circle being T_g from the linear and VFT extrapolation respectively. The downward pointing triangle is the interpolation using $T_g|_{\tau=10s}$.

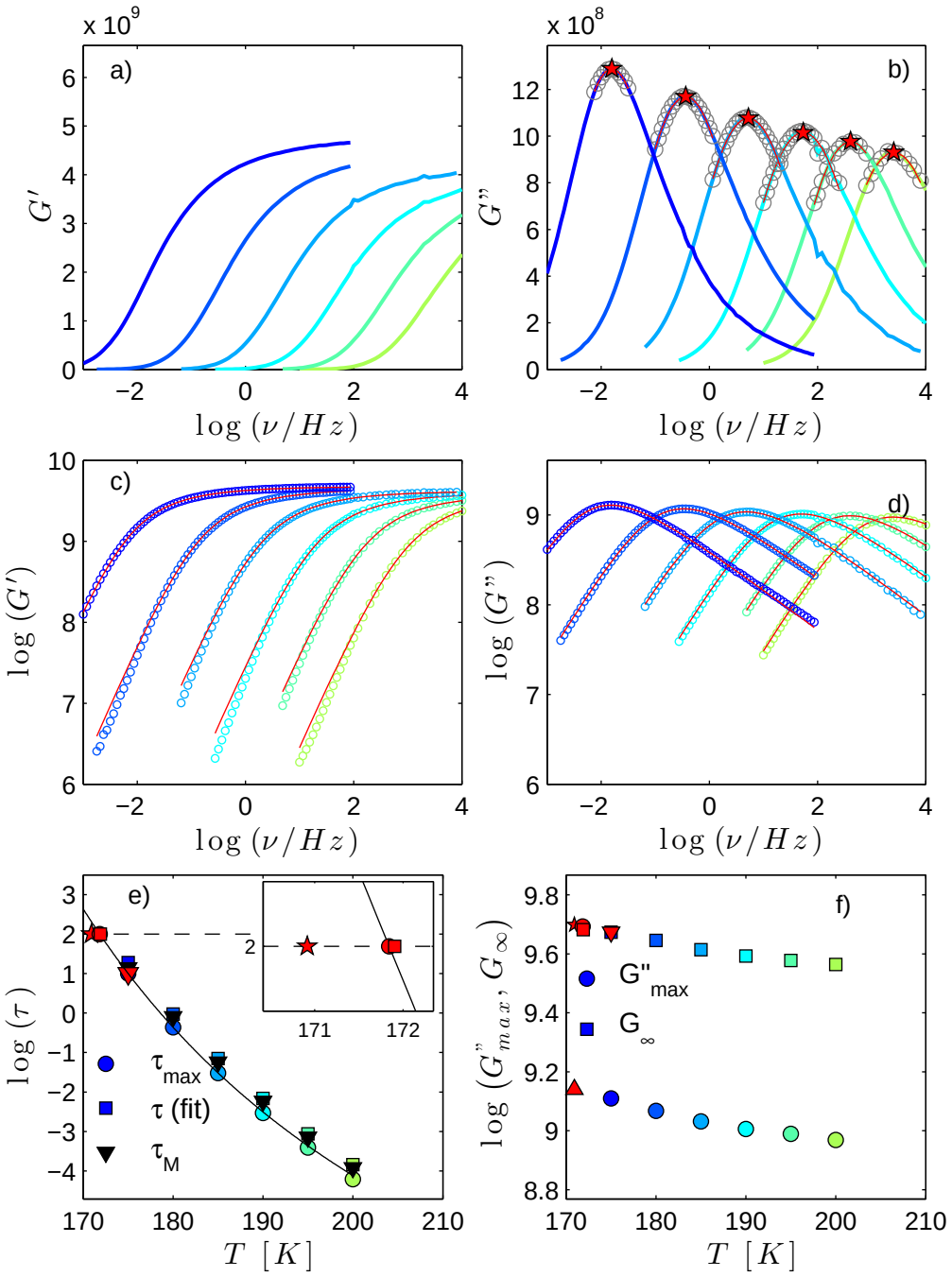

Figure 7.6: Overview of the results on the $c_G = 0.5$ mixture. From the data I extract properties as explained in section 7.3.1. a) real part of G^*. b) Imaginary part of G^*. The grey circles indicate the pointes used for fitting the second order polynomial and the red pentagons show the loss peak frequency, ν_{max}, and $G"(\nu_{max})$. c) and d) show the real and imaginary part of G^* on a log scale. The red lines are fits using extended Maxwell model. e) The relaxation times extracted. The inset shows the results of using the different extrapolations methods to get T_g. f) $G"_{max}$ and G_∞ as a function of temperature. $G_\infty(T_g)$ is shown in red with the pentagon and circle being T_g from the linear and VFT extrapolation respectively. The downward pointing triangle is the interpolation using $T_g|_{\tau=10s}$.

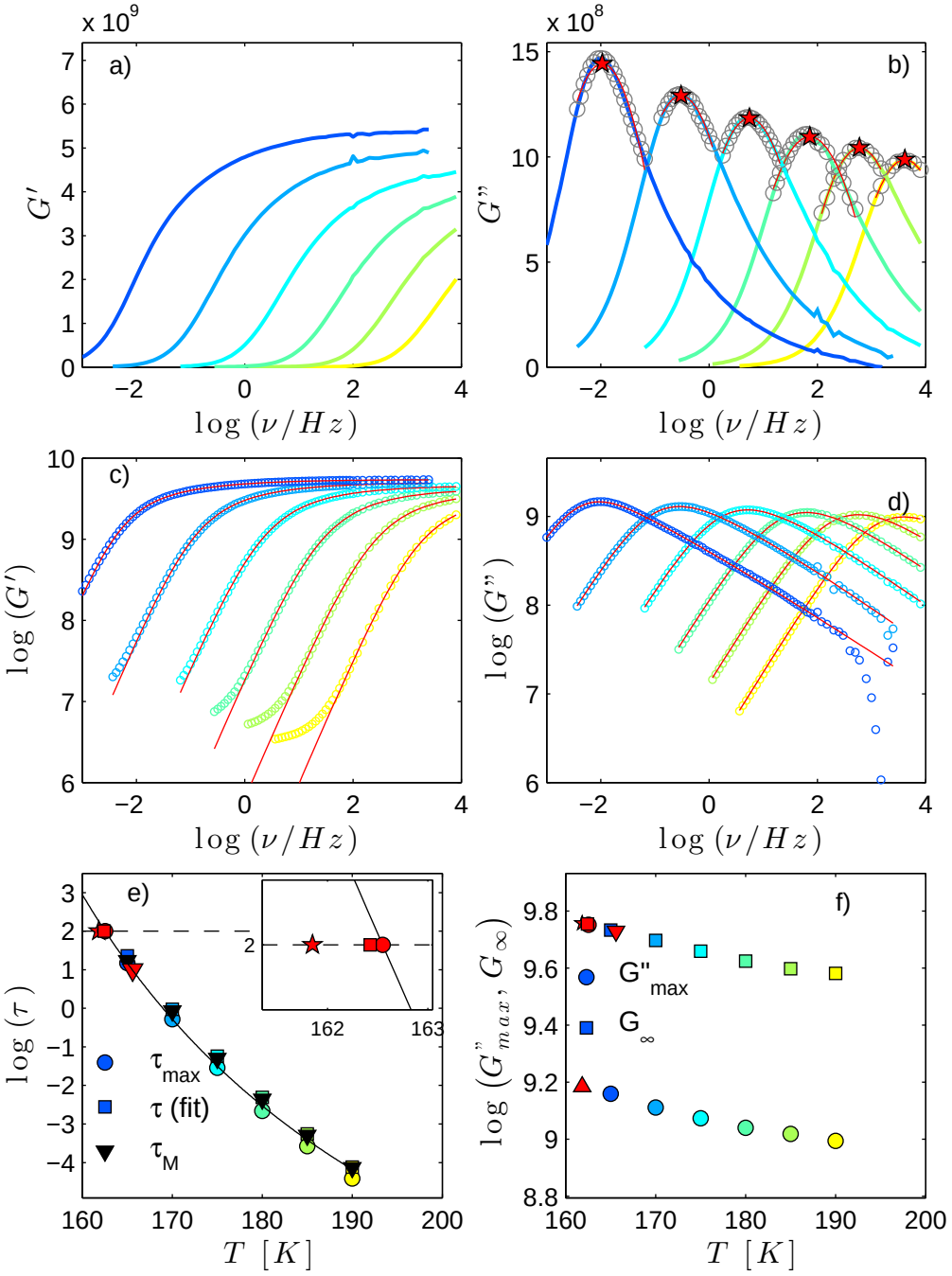

Figure 7.7: Overview of the results on the $c_G = 0.3$ mixture. From the data I extract properties as explained in section 7.3.1. a) real part of G^*. b) Imaginary part of G^*. The grey circles indicate the pointes used for fitting the second order polynomial and the red pentagons show the loss peak frequency, ν_{max}, and $G"(\nu_{max})$. c) and d) show the real and imaginary part of G^* on a log scale. The red lines are fits using extended Maxwell model. e) The relaxation times extracted. The inset shows the results of using the different extrapolations methods to get T_g. f) $G"_{max}$ and G_∞ as a function of temperature. $G_\infty(T_g)$ is shown in red with the pentagon and circle being T_g from the linear and VFT extrapolation respectively. The downward pointing triangle is the interpolation using $T_g|_{\tau=10s}$.

7.3.2 Analysing the spectral shape

To compare the spectral shape of the shear modulus the frequency of each spectrum was scaled by the peak frequency, $\nu_{\max}$. The real and imaginary part of G^* were scaled by G_∞ and $G^{"}_{\max}$ respectively. This is shown in fig. 7.8 a) and b) for a single spectrum for each concentration. The temperatures were chosen to match roughly the same relaxation time across the concentration. Fig. 7.8 a) and b) show two things. The first thing is that all concentration exhibit the $G''(\nu) \propto \nu$ and $G'(\nu) \propto \nu^2$ terminal modes. The second is that a *slow mode* is visible in neat glycerol. Furthermore, the slow mode disappears gradually with increasing water content. Interestingly the slow mode can also be seen in the 10 years old data of Schroter et al., but it seems that no one ever noticed it before [71]. For the sake of comparison the liquids 2E1H and DC704 were added to the figure. They represent a liquid with and without supra-molecular clustering respectively. We see that the glycerol-water mixtures fall between these two liquids, with neat glycerol being closer to 2E1H and the glycerol-water mixtures move toward DC704 with increasing water content. Apparently neat glycerol behaves like a liquid with supra-molecular clusters while adding water makes it behave more like a liquid without supra-molecular clusters.

Having focused on the shape of a single temperature we can continue to look at how the shape changes with temperature. Fig. 7.8 (c) and (d) show the Time-Temperature superposition for all concentrations for both the shear mechanical and dielectric spectroscopy. The dielectric data is from [64]. Each concentration has been given an offset to make comparison between the concentrations easier.

In the shear spectrum the time-temperature-superposition becomes better with increasing water content, and it appears that the slow mode and the structural relaxation separates more when the temperature is lowered. In the dielectric spectrum time-temperature-superpostion becomes worse with increasing water content as a second relaxation process emerges at $c_g = 0.5$ and becomes clearly visible for $c_g = 0.3$. The two processes separate more with decreasing temperature.

The dielectric and shear mechanical spectroscopy give different results, which stresses the importance of using different experimental techniques probing dynamics. The results will be discussed further in section 7.4.

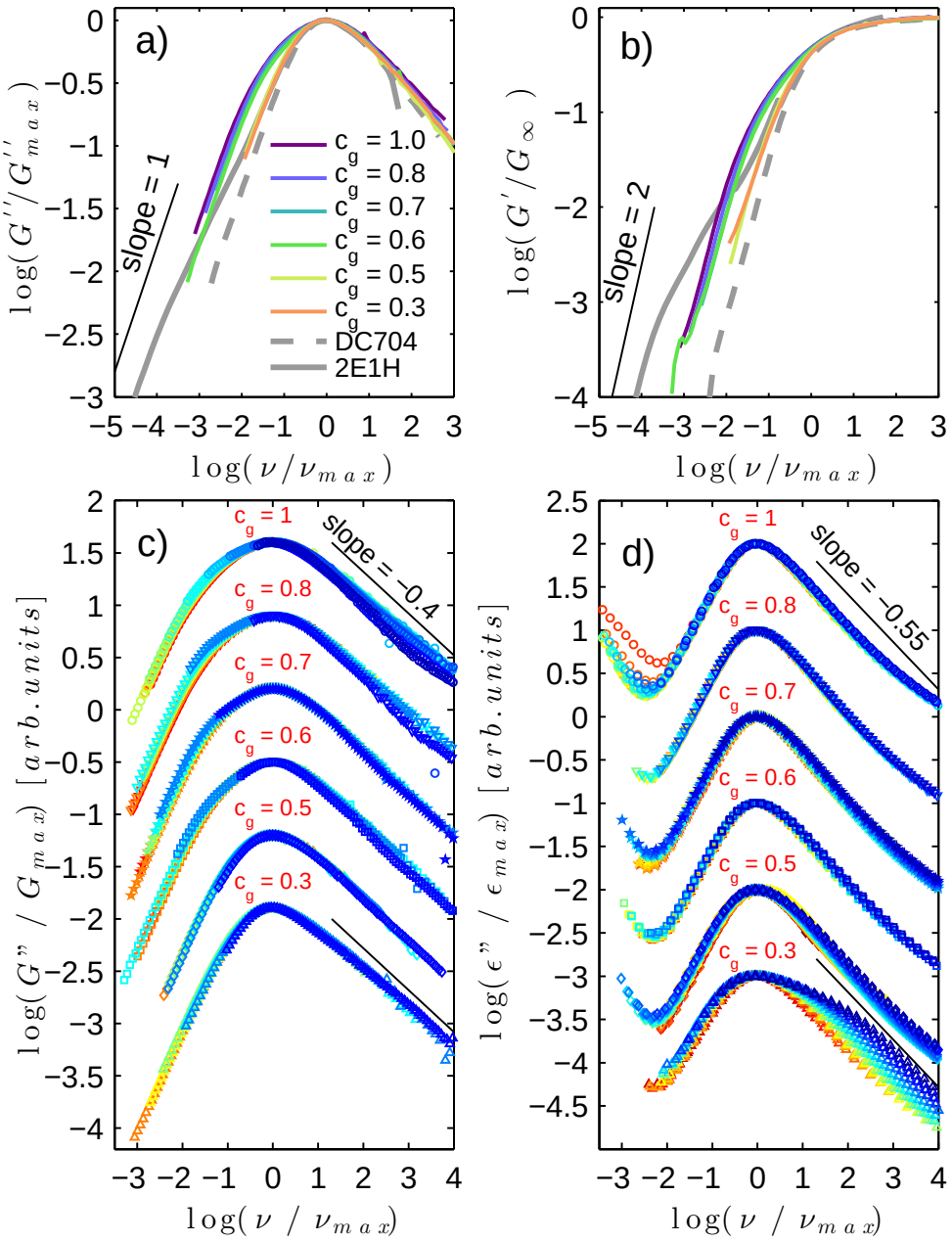

Figure 7.8: Time-temperature-superpostion of the imaginary, a), and real, b), part of G^* for a single temperature for each concentration. The temperature was chosen to match roughly the same relaxation time for each spectrum. The liquids DC704 and 2E1H are show for comparison. The imaginary part of G^* and ϵ^* are shown in c) and d) for each temperature and concentration. The dielectric data are from [64].

7.3.3 Temperature dependence of τ_{max}

Fig.7.9 shows how τ_{max} varies with temperature for each concentration. Adding water to glycerol lowers the relaxation time. This is consistent with the dielectric measurements in [64]. The inset in fig. 7.9 scales the temperature axis by T_g for each concentration. The overlap between the different concentrations is excellent.

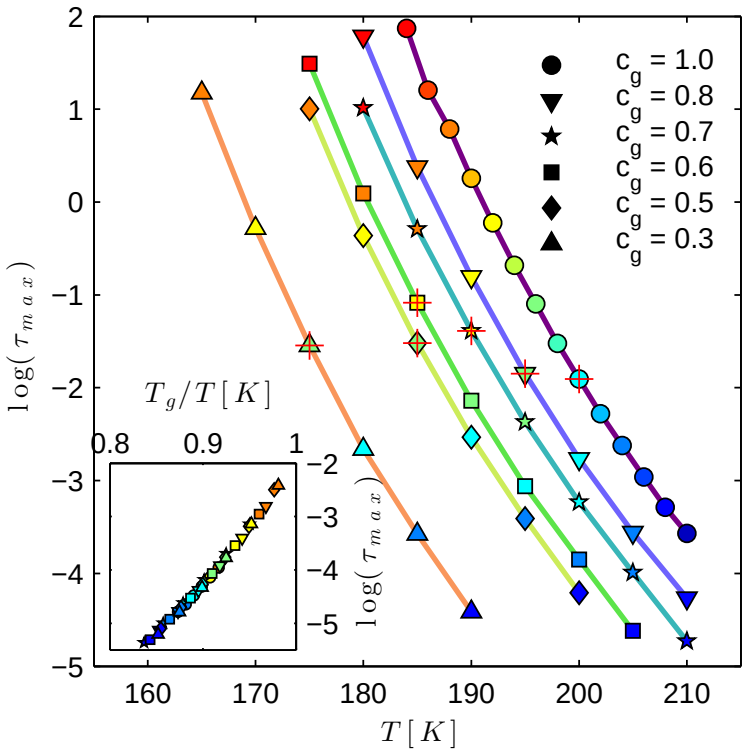

Figure 7.9: The relaxation time as a function of temperature for each concentration. Adding water to glycerol lowers the relaxation time. The red + mark the temperatures used in fig. 7.8 a) and b). The inset show show the Angell plot. The different concentrations collapse nicely.

7.3.4 Decoupling of relaxation times

To quantify the slow mode we can use the Maxwell Time which relates the instantaneous shear modulus to the viscosity of the liquid. It is given by:

$$\tau_M = \frac{\eta_0}{G_\infty} \tag{7.5}$$

where η_0 and G_∞ are the limiting behaviours:

$$\eta_0 \equiv \lim_{\omega \to 0} (G"(\omega)/\omega) \tag{7.6}$$

$$G_\infty \equiv \lim_{\omega \to \infty} (G'(\omega)) \tag{7.7}$$

To calculate τ_M it is necessary to reach both the low terminal modes of G" and the high frequency plateau of G'. Since the frequency window accessible with our set-up is restricted reaching both limiting behaviours for all temperatures is not possible. I have calculated τ_M for all temperatures, as can be seen in figs. 7.2-7.7. However, not all the temperatures are useful. For the comparison of τ_M and τ_{max} I only take the values that I trust.

In fig. 7.10 the decoupling of the two relaxation times, defined as $\log(\tau_M/\tau_{\max})$. Two things can be concluded from fig. 7.10. That decoupling decreases with increasing water content, and it drops a lot between $c_g = 0.6$ and $c_g = 0.5$. Above $c_g = 0.5$ the decoupling looks to have a temperature dependence, with the decoupling increasing as the temperature decreases. Hints of this was visible in fig. 7.8. The decoupling is compared with the decoupling in 2E1H and DC704. Again neat glycerol is close to 2E1H and adding water brings it close to DC704.

In fig. 7.11 I compare the relaxation times of the shear and dielectric spectroscopy. There is a difference in the absolute value of the relaxation time, but the temperature dependence appears to be similar.

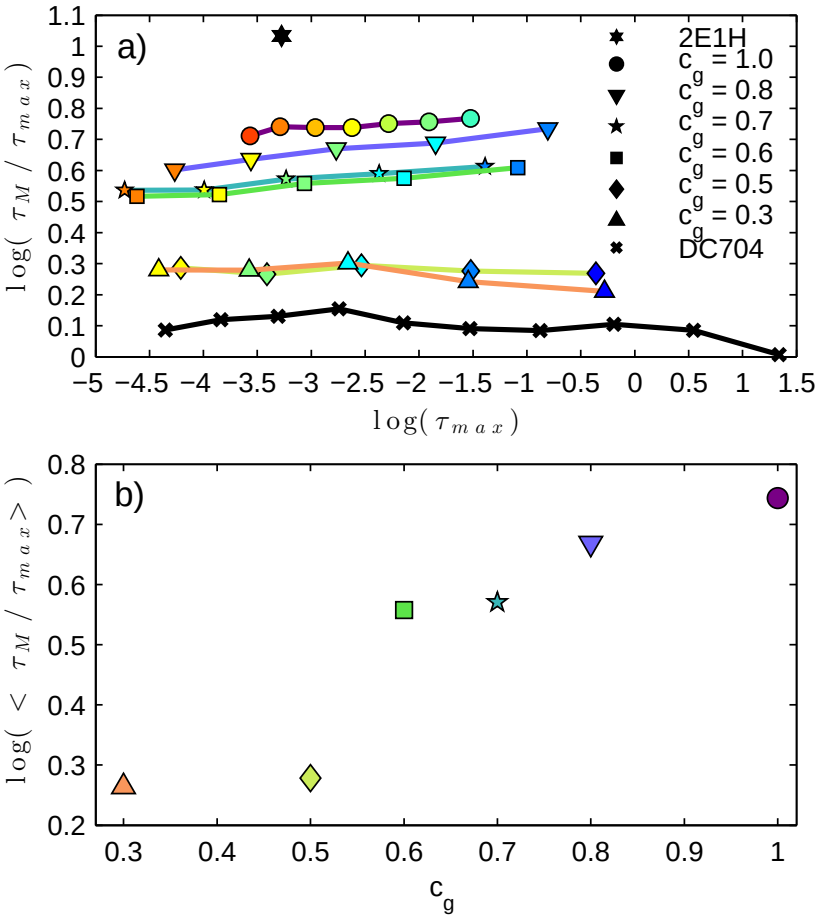

Figure 7.10: For $c_g > 0.5$ the decoupling to increase with decreasing temperature. For $c_g > 0.5$ it is constant or slightly decreasing. The colours correspond to the temperatures in fig. 7.9. The decoupling drops between $c_g = 0.6$ and $c_g = 0.5$.

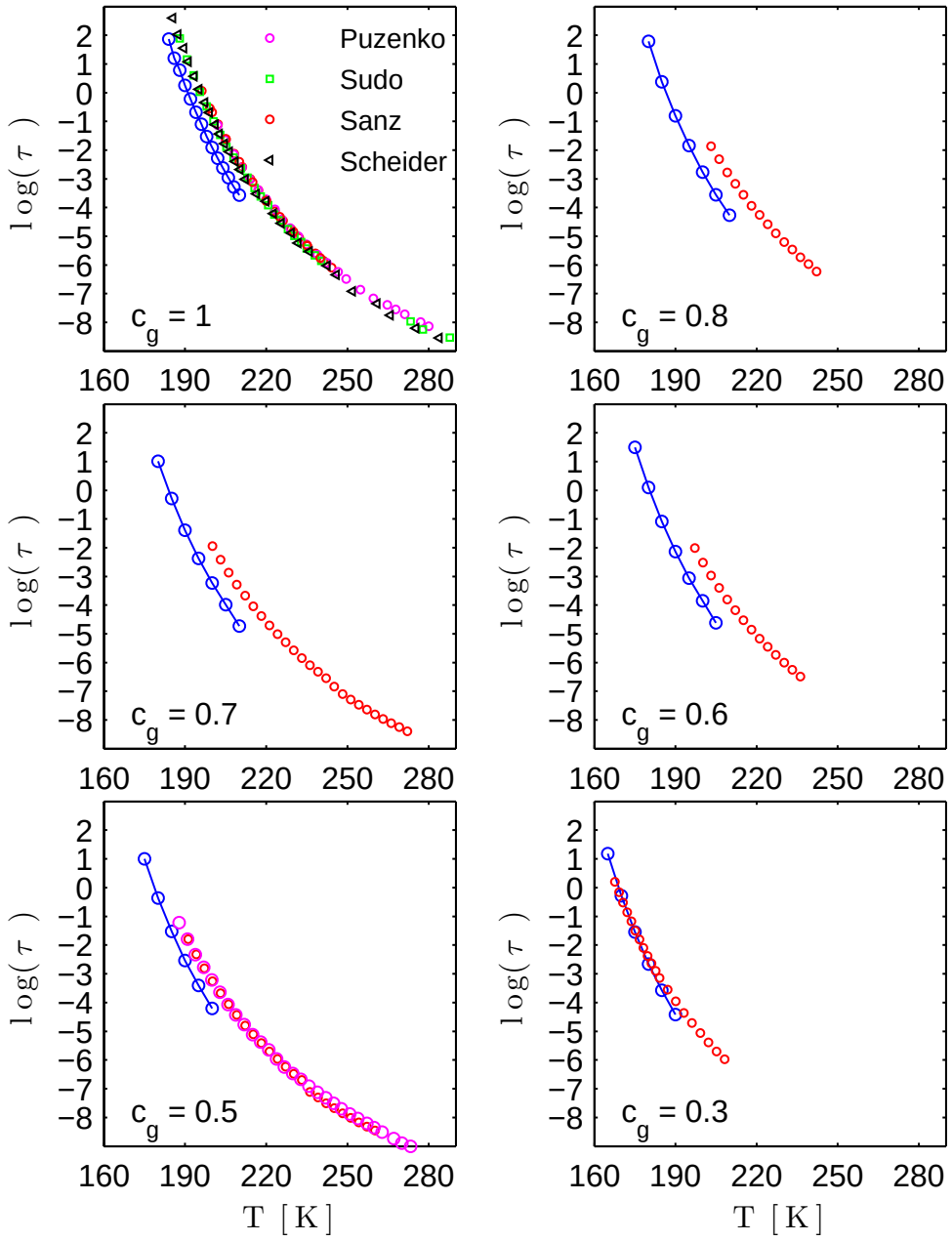

Figure 7.11: Comparing the relaxation times from shear (blue circles) with the ones from dielectric spectroscopy (see legend). Puzenko data is from [65]. Sudo data is from [80]. Sanz data is from [67].

7.3.5 The fitting parameters from the Extended Maxwell Model

The fits with the Extended Maxwell Model are not intended to accurately describe the entire spectrum. In fact, since it does not model the slow mode we know it will do poorly on the low frequency side. I only really use it to get a reliable estimate of G_∞. However, for the sake of completeness I show the fitting parameters in fig. 7.12.

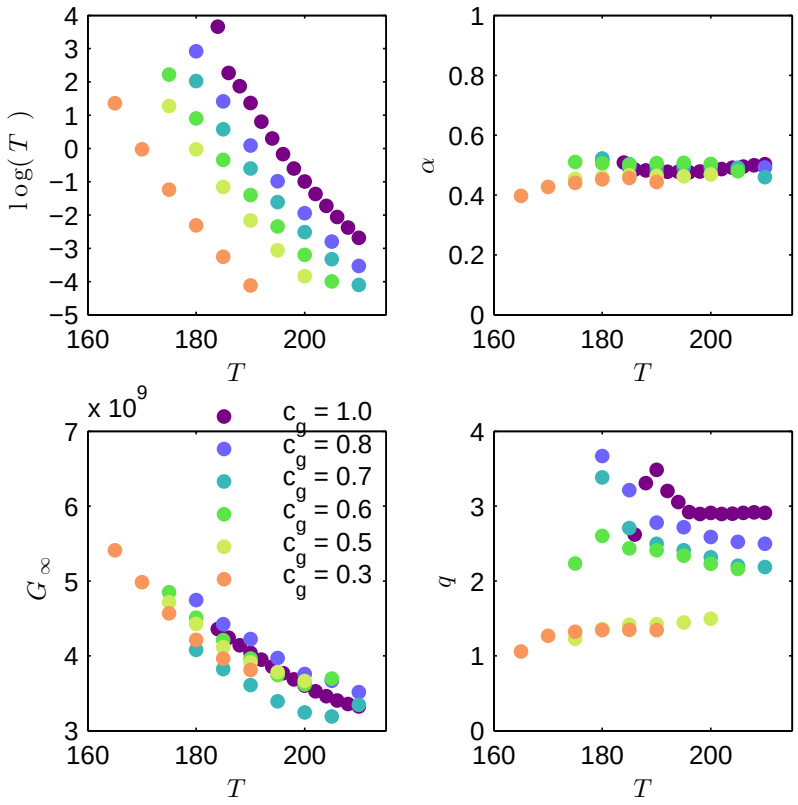

Figure 7.12: The parameters from fitting the Extended Bell Model to the entire spectrum for each temperature of each sample.

7.3.6 Temperature dependence of G_∞

In fig. 7.12 I showed how G_∞ changed with temperature for the different mixtures. The temperature dependence of G_∞ was similar all samples, but the absolute values were shifted slightly.

In fig. 7.13 I compare our G_∞ values from neat glycerol with those reported in the litterature. Our values compare nicely with Schroter (2006) values, but not with the ones reported by Scarponi.

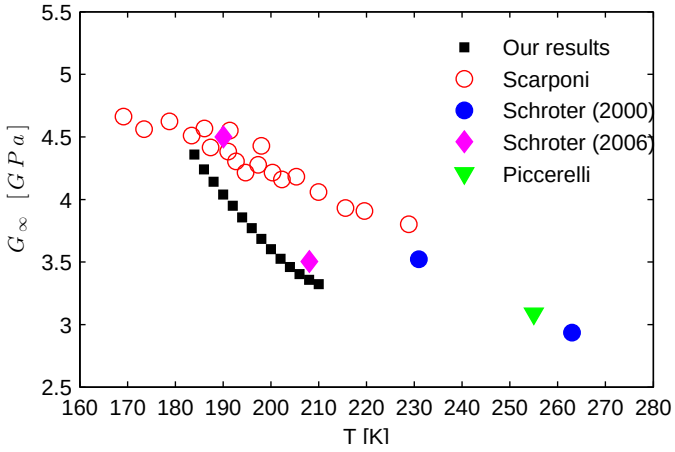

Figure 7.13: Here I compare the G_∞ values for neat glycerol with values reported in the literature. Scarponi data is from [68]. Schroter (2000) data is from [70]. Schroter (2006) data is from [71]. Piccirelli are using an ultrasonic technique [61].

7.3.7 The showing model

According to the shoving model is should be possible to collapse the relaxation time onto a single curve, if the temperature axis is scaled in an appropriate manner. The single curve is defined by[35]:

$$\ln\left[\tau(T)\right] = \left[\frac{\tau(T_g)}{\tau_0}\right] \frac{G_\infty(T)}{T} \frac{T_g}{G_\infty(T_g)} + \ln(\tau_0). \tag{7.8}$$

Defining

$$X \equiv \frac{G_\infty(T)T_g}{G_\infty(T_g)T}, \tag{7.9}$$

and using the standard definition of T_g as $\tau(T_g) = 100s$, and $\tau_0 = 10^{-14}$, gives the following:

$$\log\left(\tau(T)\right) = 16X - 14. \tag{7.10}$$

In our case we had to use T_g defined as $\tau(T_g) = 10s$ to avoid extrapolations. So instead the line used here is:

$$\log\left(\tau(T)\right) = 15X - 14. \tag{7.11}$$

Fig. 7.14 shows the relaxation time plotted vs X. It works well in the entire concentration range.

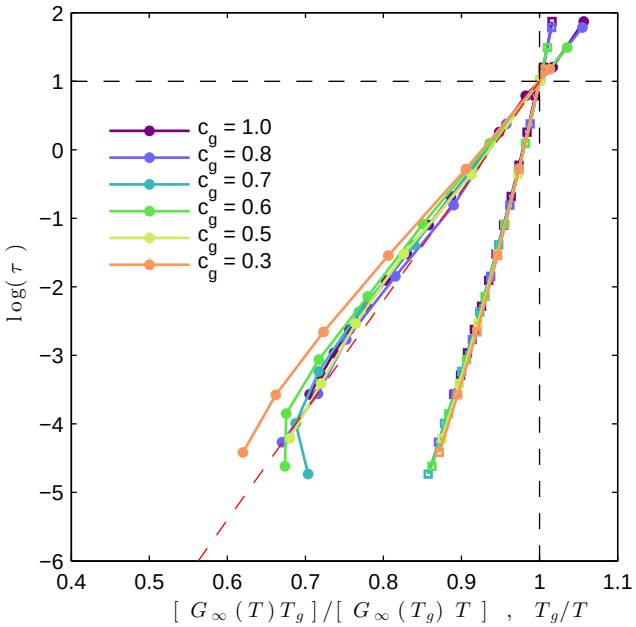

Figure 7.14: Comparing the Angell plot (squares) and Shoving plot (circles). The shoving model holds well in the entire concentration and temperature range.

7.4 Discussion

In this section I will combine our shear-mechanical results with data from the literature to form a cohesive picture of what takes place in the sample. This is made difficult by the fact that the different studies are rarely made in the same temperature and/or concentration range.

The first thing to note is that the volume of glycerol and water decreases upon mixing [26]. This effect is called negative excess molar volume. The excess molar volume has a minimum close to $c_g \approx 0.3$ which is also where a minimum in T_m is seen[56]. The minimum of the excess molar volume shifts towards lower c_g with decreasing temperature. This means that optimal packing of the molecules happens at a lower concentration of glycerol for lower temperatures. The excess molar volume becomes more negative with decreasing temperature. This increased packing efficiency can come from two places: Either the hydrogen-bonded network changes or the conformation of glycerol changes. Both possibilities will be discussed in the following. However, it should be noted that the experiments were performed in the 278 to 333 K range, so extrapolation deep into the super-cooled liquid state is dangerous.

A computer simulation has shown that conformation of glycerol – that is the internal structure of glycerol – changes when mixed with water [25]. They found that the water molecules tended to aggregate and that the size of the aggregates decreases with increasing concentration of glycerol. However, the computer simulations of the conformation is based in mixtures with $c_g \approx 0.22$ and $c_g \approx 0.12$. This brings them into the intermediate and low concentration range respectively, so the relevance to our concentration range is not entirely clear. But it at least open up for the possibility that some of the increased packing efficiency is caused by changes to the conformation of glycerol.

Towey et. al. has used neutron scattering to study the hydrogen-bonded structure in glycerol[85] as well as glycerol-water mixtures[83, 84, 86]. They find that in neat glycerol each glycerol molecule forms 5.68 ± 1.51 hydrogen-bonds per molecule while for neat water the number of hydrogen-bonds per water molecule is about 3.56 ± 1.10. When mixing water and glycerol the number of hydrogen-bonds per molecule remain almost constant, but the number of glycerol-glycerol hydrogen-bonds decrease as they are replaced by glycerol-water hydrogen-bonds. So while the number of hydrogen-bonds remain constant the hydrogen-bonded structure changes. Thus, both the conformation of glycerol and the nature of the hydrogen-bonded network changes when water is added to glycerol.

The slow mode in the shear mechanical spectrum may be explained by changes in the hydrogen-bonded network of glycerol. If the slow mode was directly related to the fraction of glycerol-glycerol bonds to glycerol-water or

water-water bonds we would expect a gradual change in the decoupling throughout the concentration range, as was reported for the hydrogen-bonded network [86]. The sudden change in the decoupling below $c_g = 0.6$ suggests a percolation effect, e.g. a percolation in terms of the extent of the glycerol-glycerol hydrogen-bonded network. One could then explain the changes in the sample as the glycerol-glycerol hydrogen-bonded structures stop percolating the sample for $0.6 > c_g > 0.5$. But according to [86] glycerol-glycerol bonded structures are still percolating the sample at $c_g = 0.5$. Therefore percolation effects alone does not seem to explain our observation. However, the neutron scattering results are at room temperature. In our results we have seen the temperature dependence of the decoupling, so comparing to room temperature may be dangerous.

The fact that no slow mode is visible in the dielectric spectrum tells us that the hydrogen-bonded network is structured in such a way that it does not build up a net dipole moment.

In [52] they study neat glycerol by NMR, and get a spectrum that look a lot like our shear mechanical spectrum. They split the relaxation spectrum into inter and intra molecular motion. They contribute the slow mode to intermolecular motion, that is, the motion of the hydrogen-bonded network. This supports our notion that the slow mode we see in the shear mechanical spectrum is connected to the hydrogen-bonded network. This study was done on neat glycerol and in the 248 K - 348 K range.

In [55] they use Raman spectroscopy to study glycerol/D2O mixtures for $c_g = 0, 0.02, 0.12, 0.32, 1$. They find that the addition of D2O to neat Glycerol breaks the glycerol-glycerol hydrogen bonding, taking it from oligomers to monomers. They report that for $c_g = 0.32$ the D2O solution looses its hydrogen-bonding network completely and exist in the solution as monomers. This was also the concentration for which the dielectric spectrum shows a high frequency shoulder. This suggest that the shoulder in the dielectric spectrum may be connected to the formation of water domains in the sample.

Taken together, results above give rise to the following physical picture of what takes place in the sample: The slow mode reflects the glycerol-glycerol hydrogen-bonded network. When water is added to glycerol the glycerol-glycerol hydrogen-bonded network is diminished in extent, resulting in a decrease of the slow mode. When $c_g \approx 0.5$ the glycerol and water starts to segregate, and the water now dominates the shear-mechanical properties of the mixture.

7.5 Concluding remarks

Shear mechanical spectroscopy was used to study the neat glycerol and glycerol-water mixtures. A slow mode in neat glycerol was revealed, which gradually

disappeared when the concentration of water was increased. We suggest that the slow mode reflects the glycerol-glycerol hydrogen-bonded network. When water is added to glycerol the glycerol-glycerol hydrogen-bonded network is diminished in extent, resulting in a decrease of the slow mode. When $c_g \approx 0.5$ the glycerol and water starts to segregate, and the water now dominates the shear-mechanical properties of the mixture.

8 | Concluding remarks

In this chapter a reflection on my thesis as a whole will be presented. I will address the key questions raised in this thesis and suggests ways of making further progress on those questions.

The focus of this thesis has been the structure and dynamics of hydrogen-bonded liquids. Two aspects of this relationship has been studied. The first aspect was to study the crystallisation of hydrogen-bonded systems, with the aim of understanding how the molecular dynamics influences the crystallisation and vice versa. The second aspect was to study the dynamics of the supra-molecular hydrogen-bonded structures, that are believed to form in these liquids, with the aim of getting a better microscopic understanding of the dynamics of the structures.

8.1 Key questions

8.1.1 How dynamics influences crystallisation and vice versa

The motivation for studying n-butanol during crystallisation was originally to get a better understanding of the interplay between molecular dynamics and crystallisation. There are two perspective to this: One perspective is to study how different relaxation processes influence the crystallisation process in terms of the kinetics of the crystallisation process and the morphology of the crystal domains. The second perspective is to see how the structural constraints imposed by the crystalline ordering influence the relaxation processes.

Dielectric spectroscopy seemed like a good experimental technique because it is fast, easy, and sensitive to changes in the rotational dynamics of the molecules. However, the growing inhomogeneity of the sample during crystallisation turned out to be more difficult to deal with than expected. For this reason, I no longer believe that dielectric spectroscopy alone is a useful tool for probing dynamical changes during crystallisation. At least not until the Maxwell-Wagner analysis proposed in this thesis has been tested rigorously. I will put forward some suggestion on how to make progress on this in sec. 8.2.3.

Therefore, my contribution to this question has consisted in bringing to light a limitation of dielectric spectroscopy, rather than new results that help us understand how dynamics influences crystallisation and vice versa.

The main conclusion from my work on this question is, that simultaneous experiments are necessary if one is interested in comparing results across different

experimental techniques.

8.1.2 The liquid-liquid transition

Liquid-liquid transitions (LLTs) have been claimed to exist in both n-butanol and the glycerol-water mixture with a 0.178 molar concentration of glycerol. However, the claims have also been challenged in both cases, as I explained in chapter 1. After having studied both liquids I am now of the opinion that the existence of LLTs have not been convincingly demonstrated in these liquids. I want to make it clear that I am not against the LLT hypothesis on a fundamental level – I see nothing wrong with molecules packing differently under different conditions. LLTs may exist in these liquids, and it may one day be possible to observe them experimentally. But I do not believe that has happened yet.

My reasoning is essentially applying Occam's razor to the problem: Of the two hypotheses put forward to explain the experiments observations, I believe that a crystallisation process is the simplest. The existence of a new liquid phase should only be used as an explanation if none of the phases we already know to exist can explain the observations. The argument that the LLT takes place just before the crystallisation is not convincing to me.

8.1.3 The dynamics of supra-molecular hydrogen-bonded structures

One of the motivations for studying n-butanol in a wide temperature range using dielectric spectroscopy and neutron spin echo was to get more information about the microscopic origins of the Debye process. My contribution has been to show that using dielectric spectroscopy at high temperatures is dangerous because the fitting procedure can become unreliable. However, neutron spin eco and viscosity data can be used together with the dielectric data to give a more complete picture of the temperature dependence of the relaxation time.

Personally, I think that the interpretation of the Debye process, seen in dielectric spectroscopy, as fluctuations of the the end-to-end dipole moment of the supra-molecular clusters, is correct. I believe that the transient chain model has the right idea, but that it should be updated to be consistent with the fact that slow modes are also observed in mechanical-spectroscopy for at least some of these systems.

Our discovery of a slow mode in the shear-mechanical spectrum of neat glycerol, which is not present in the dielectric spectrum, and may be connected to the hydrogen-bonded network between the glycerol molecules. The fact that the slow mode is not present in the dielectric spectrum could be because the hydrogen-bonded structure does not build up a net dipole moment.

Both contributions described in this section emphasise the need for using

different techniques when studying the dynamics of liquids.

8.2 Things for the future

8.2.1 Using computer simulations to study crystallisation

The questions we have been addressing about crystallisation could also be aided by results from computer simulation. When studying crystallisation we have used one of three ways of getting structural information: Either we do scattering experiments and look for changes in the structure factor; or we do dielectric spectroscopy and use the the kinetics an the Avrami equation; or we do dielectrics and do a Maxwell-Wagner analysis.

One way to approach this question with computer simulations would be to use the interface pinning method[60]. This method can be used to calculate the growth rate of the crystallisation process, and since the morphology of the growth is 2-dimensional in the the method, the Avrami parameter is known (if the formation of new nuclei can be checked or controlled). It would be interesting to simulate the crystallisation of systems with different dynamics to look for a relationship between dynamics and crystallisation that goes deeper than the mere diffusion controlled predictions of classical nucleation theory.

8.2.2 Shear-mechanical spectroscopy on n-Butanol during crystallisation

Shear-mechanical spectroscopy experiments on n-butanol would be interesting for two reasons. The first would be to see if a slow mode is visible in the shear mechanical spectrum of n-butanol. I suspect it will be.

The second reasons is that doing shear-mechanical spectroscopy doesn't have the Maxwell-Wagner polarisation problem. So it may be a better suited than dielectric spectroscopy for studying changes to the dynamics during crystallisation.

I have not done these measurements during my thesis because crystallisation would break the ceramic plates used in the cell. However, together with the workshop at RUC Tina Hecksher has now developed a cell that partly avoids these problems, making the experiments described here feasible.

8.2.3 Maxwell-Wagner polarisation

I am convinced that simultaneous measurements is of the utmost importance when studying crystallisation. The Maxwell-Wagner analysis presented in sec. 3.3 was put forward as a way of explaining why we got different results when using different sample cells for dielectric spectroscopy. In fact, the Maxwell-Wagner effect *should* occur whenever one is measuring on inhomogeneous mixtures using dielectric spectroscopy. However, other effects, such as changes to

the dynamics of the supra-molecular structures, may come into play simultaneously. Therefore the Maxwell-Wagner models presented here should be tested.

In this thesis I have presented preliminary data from simultaneous dielectric spectroscopy and neutron scattering experiments, intended to test the Maxwell-Wagner models. The experiments were largely unsuccessful, but with changes to the design of the cell it should be possible to carry out the experiment.

One of the open questions about the Maxwell-Wagner model, as presented here, is how far the volume fraction of spheres, $\phi_{spheres}$, can be pushed. At some point the mean-field approximation should break down, but it is not clear exactly when.

One way to approach this problem is to do computer simulations. Nick Bailey has started working on this together with students at RUC. They simulate a capacitor filled with rectangular domains of dielectric permittivity ϵ_2 embedded in a matrix of dielectric permittivity ϵ_1. They calculate the potential at every point inside the capasitor and use this to calculate the capacitance of the capacitor, which gives them the compound dielectric permittivity. Preliminary results suggest that the Maxwell-Wagner model is accurate to at least $\phi_{\text{spheres}} = 0.5$. They have not simulated higher concentrations yet. Much remains to be done, since the calculations were done on rectangular domains in 2D, but the preliminary results are encouraging.

Appendices

A | Finding the electric potential outside a sphere

In chapter 3 I presented two Maxwell-Wagner models: One of a crystal layer and one of spherical crystal domains. For the spherical model, the electric potential outside a sphere imbedded in a dielectric material, is needed. Here I show how the electric potential is found. This is standard text book stuff [32]. I include it here for the sake of completeness.

Consider a sphere of dielectric material of dielectric permittivity, ϵ_c, placed in an infinite dielectric material of dielectric permittivity, ϵ_l, with a uniform electric field. To find the electric potential, V, one must solve Laplace's equation:

$$\nabla^2 V = 0 \tag{A.1}$$

where ∇^2 is the Laplacian.

The boundary conditions we are going to use are the following the following:

$$(i) \qquad V_{in}(r,\theta) = V_{out}(r,\theta) \quad \text{for} \quad r = R \tag{A.2}$$

$$(ii) \qquad \epsilon_c \frac{\partial V_{in}}{\partial r} = \epsilon_l \frac{\partial V_{out}}{\partial r} \quad \text{for} \quad r = R \tag{A.3}$$

$$(iii) \qquad \lim_{r\to\infty} V_{out}(r,\theta) = -E_0 r\cos\theta \quad \text{for} \quad r >> R. \tag{A.4}$$

Where V_{in} and V_{out} are the electric potentials inside and outside the sphere. E_0 is the strength of the electric field.

A general expression for the electric potential is:

$$V(r,\theta) = \sum_{l=0}^{\infty} \left(A_l r^l + \frac{B_l}{r^{l+1}} \right) P_l(\cos\theta), \tag{A.5}$$

where P_l is the lth order Legendre polynomial. A_l and B_l constant for each term of the sum.

Writing up the expression for the potential inside and outside the sphere:

$$V_{in}(r,\theta) = \sum_{l=0}^{\infty} \left(A_l r^l + \frac{B_l}{r^{l+1}} \right) P_l(\cos\theta) \tag{A.6}$$

$$V_{out}(r,\theta) = \sum_{l=0}^{\infty} \left(C_l r^l + \frac{D_l}{r^{l+1}} \right) P_l(\cos\theta). \tag{A.7}$$

Where C_l and D_l are constants. Using the the boundary conditions one can determine the constants A_l, B_l, C_l and D_l.

The first step is to realise that we do not want the potential to blow up inside the sphere. This means that $B_l = 0$ since the term B_l/r^{l+1} would blow up for small r otherwise. Similarly we can use boundary condition (iii) (eq. A.4) to establish that $C_l = 0$ since the term $C_l r^l$ would blows up for $r \to \infty$ which is not consistent with the boundary condition.

This allows us simplify eq. (A.7) and eq. (A.6):

$$V_{in}(r,\theta) = \sum_{l=0}^{\infty} \left(A_l r^l\right) P_l(\cos\theta) \tag{A.8}$$

$$V_{out}(r,\theta) = \sum_{l=0}^{\infty} \left[\left(\frac{D_l}{r^{l+1}}\right) P_l(\cos\theta)\right] - E_0 r\cos\theta \tag{A.9}$$

We can then use boundary condition (i) (eq. A.2) to write up the following expression:

$$\sum_{l=0}^{\infty} A_l R^l P_l(\cos\theta) = \sum_{l=0}^{\infty} \left[\left(\frac{D_l}{R^{l+1}}\right) P_l(\cos\theta)\right] - E_0 R\cos\theta \tag{A.10}$$

We cannot get any further using the boundary conditions alone, but there is a trick. We can get rid of the sums by using the fact that the Legrendre polynomials are orthogonal, that is:

$$\int_0^{\pi} P_n(\cos\theta) P_l(\cos\theta)\sin\theta d\theta = \frac{2}{2l+1} \tag{A.11}$$

for $n = l$ and 0 for $n \neq l$.

This allows us to pick out the term $n = l$ term from the sums by multiplying both sides of eq. (A.10) by $P_n(\cos\theta)\sin(\theta)$ and integrating from 0 to π, giving:

$$\int_0^{\pi} P_l(\cos\theta) P_l(\cos\theta)\sin\theta A_l R^l d\theta = \tag{A.12}$$

$$\int_0^{\pi} P_l(\cos\theta) P_l(\cos\theta)\sin\theta \frac{D_l}{R^{l+1}} d\theta - \int_0^{\pi} P_l(\cos\theta)\sin\theta\cos\theta E_0 R d\theta. \tag{A.13}$$

Using just $l = 1$, eq. (A.11), and $\int_0^{\pi}(\cos^2\theta\sin\theta)d\theta = 2/3$, the expression simplifies to:

$$A_1 = \frac{D_1}{R^3} - E_0 \tag{A.14}$$

But for $l \neq 1$ we get:

$$A_l R^l = \frac{D_l}{R^{l+1}} \tag{A.15}$$

From eq. (A.15) we can conclude that $A_l = D_l = 0$ for $l \neq 1$. So all we need now is D_1.

By using $l = 1$ in the expressions for $V_{\text{in}}(r, \theta)$ and $V_{\text{out}}(r, \theta)$ and inserting them in in boundary condition (ii) (eq. A.3) and carrying out the differentiation we get

$$\epsilon_c A_1 = -\epsilon_l \left(\frac{2D_1}{R^3} + E_0 \right) \tag{A.16}$$

Inserting A_1 from eq. (A.14) gives:

$$\epsilon_1 \left(\frac{D_1}{R_3} - E_0 \right) = -\epsilon_2 \left(\frac{2D_1}{R^3} + E_0 \right) \tag{A.17}$$

From which it follows that

$$D_1 = \frac{E_0 R^3 (\epsilon_c - \epsilon_l)}{\epsilon_c + 2\epsilon_l}. \tag{A.18}$$

Inserting eq. (A.18) into eq. (A.9), and using $P_1(\cos\theta) = \cos\theta$ gives us:

$$V_{out}(r, \theta) = \left(\frac{\epsilon_c - \epsilon_l}{\epsilon_c + 2\epsilon_l} \frac{R^3}{r^2} - r \right) E_0 \cos\theta. \tag{A.19}$$

Which is the expression we set out to derive.

B | Sillars' derivation of ellipsoids embedded in a matrix

In chapter 3 I presented two Maxwell-Wagner models: One of a crystal layer and one of spherical crystal domains. Here I present an extension of the of the spherical case to cover ellipsoids. It was not used in the analysis of the crystallisation data, but is included here for future reference.

B.1 Ellipsoid imbedded in a matrix

We have treated the case of spherical domains embedded in a matrix. If one has crystallites in mind, this is a decent assumption since the crystallites probably have all sorts of shapes. The average of all these shapes probably aren't too different from being spherical.

However, the shapes could be different. Sillars derived an expression that takes into account the shape of the domains imbedded in the matrix [74].

The derivation follows the one for the spherical case, presented in sec. 3.3.3, but since the domains are ellipsoids the mathematics become more involved. Before we calculate the potential of the situation describe above, it is useful to introduce some short hand notation concerning the geometry of the situation.

B.2 Geometry

Any point inside the spheroid will obey the following expression:

$$\frac{x^2}{a^2}+\frac{y^2}{b^2}+\frac{z^2}{c^2}=1 \tag{B.1}$$

Since we will later be interesting in properties in the neighbourhood of the boundary of the spheroid we can write up an expression of an extension, u to the spheroid as follows:

$$\frac{x^2}{a^2+u}+\frac{y^2}{b^2+u}+\frac{z^2}{c^2+u}=1 \tag{B.2}$$

Since we will often be using the surface of this extended spheroid, we will denote the root of this equation as α. Thus, α are the points on the surface of this spheroid and will be used throughout the following derivations. Another useful quantity to define is β:

$$\beta \equiv \frac{\sqrt{(a^2+\alpha)(b^2+\alpha)(c^2+\alpha)}}{2\pi abc}, \tag{B.3}$$

which is the ratio between the extended spheroid and the original. Finally we will define l_a

$$l_a \equiv \int_{\alpha}^{\infty} \frac{d\alpha}{(a^2+\alpha)\beta} = \frac{4\pi}{n} \tag{B.4}$$

These definitions will greatly simplify the remainder of the derivation.

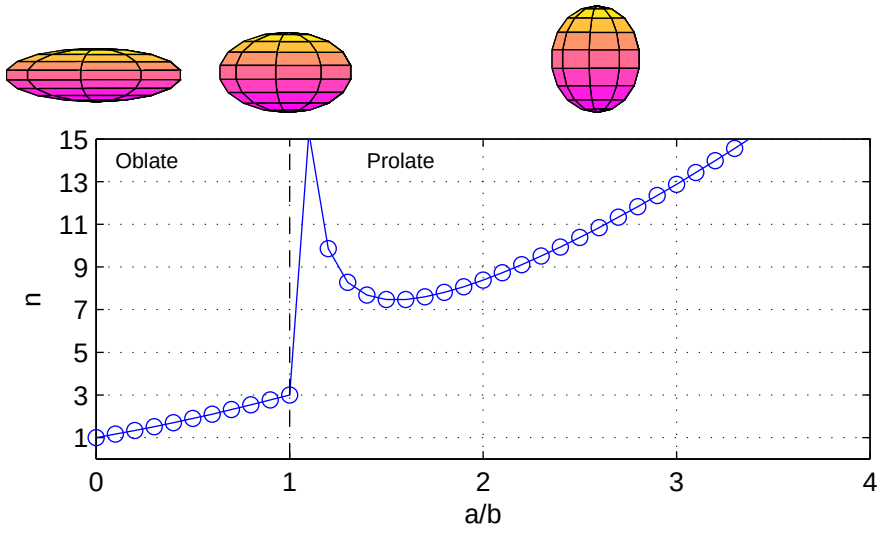

Figure B.1: Showing how the parameter n varies as a function of a/b.

B.3 The potential inside and outside the spheroid. Boundary conditions. Laplace's equation

Sillars' way of getting the potential outside the spheroid is different from what we did in section 3.3.3 for the spheres. He simply shows that a given potential satisfies Laplace's equation and the boundary conditions. Solutions to the Laplace equation are unique, so as long as you have a potential that satisfies the equation and the boundary conditions, it does not matte how you came by the potential.

In Sillars' paper he gives the potential inside the spheroid as:

$$V_1 = -xk_z \left[1 - \frac{\epsilon_2 - \epsilon_1}{4\pi\epsilon_1 + (\epsilon_2 - \epsilon_1)l_a} \int_{\alpha}^{\infty} \frac{d\alpha}{(a^2+\alpha)\beta} \right], \tag{B.5}$$

and the potentiel outside to be

$$V_2 = -xk_x \frac{4\pi\epsilon_1}{4\pi\epsilon_1 + (\epsilon_2 - \epsilon_1)l_a}. \tag{B.6}$$

where β and l_a are defined by eq. (B.2) and (B.4), respectively.

B.4 Finding the dielectric constant of the inhomogeneous material

The rest of the derivation follows the case of the spheres. He equates the expressions for two cases. The first case is that of spheroids of dielectric permittivity ϵ_2 embedded in a matrix of dielectric permittivity ϵ_1. The second is that of a spheroid of dielectric material ϵ_{comp}, embedded in a matrix of permittivity ϵ_1.

The electric potential far away from the first case is given by:

$$V = E\frac{(\epsilon_2 - \epsilon_1)\phi w}{4\pi\epsilon_1(\epsilon_2 - \epsilon_1)l_a} \tag{B.7}$$

where E is the strength of the electric field, and w is the volume taken up by the spheroids.

Likewise electric potential far away from the second case if given by:

$$V = E\frac{(\epsilon_{comp} - \epsilon_1)w}{4\pi\epsilon_1(\epsilon_2 - \epsilon_1)l_a'} \tag{B.8}$$

Equation the two expressions, canceling E and w and isolating ϵ_{comp} leaves:

$$\epsilon_{\text{comp}} = \frac{4\pi\epsilon_1}{\dfrac{4\pi\epsilon_1 + (\epsilon_2 - \epsilon_1)l_a}{(\epsilon_2 - \epsilon_1)q} - l_a'} + \epsilon_1 \tag{B.9}$$

What remains to be done now is cleaning up the expression.

Putting everything in the denominator on the same denominator and taking ϵ_1 outside a parentheses we get

$$\epsilon_{\text{comp}} = \epsilon_1\left(\frac{4\pi\epsilon_1}{\dfrac{4\pi\epsilon_1 + (\epsilon_2 - \epsilon_1)l_a - (\epsilon_2 - \epsilon_1)\phi l_a'}{(\epsilon_2 - \epsilon_1)q}} + 1\right) \tag{B.10}$$

wich is equivalent to

$$\epsilon_{\text{comp}} = \epsilon_1\left(\frac{4\pi(\epsilon_2 - \epsilon_1)q}{4\pi\epsilon_1 + (\epsilon_2 - \epsilon_1)l_a - (\epsilon_2 - \epsilon_1)\phi l_a'} + 1\right) \tag{B.11}$$

putting everything inside the parentheses on a common denominator, we get

$$\epsilon_{\text{comp}} = \epsilon_1\left(\frac{4\pi(\epsilon_2 - \epsilon_1)q + 4\pi\epsilon_1 + (\epsilon_2 - \epsilon_1)l_a - \phi l_a'(\epsilon_2 - \epsilon_1)}{4\pi\epsilon_1 + (\epsilon_2 - \epsilon_1)l_a - \phi l_a'(\epsilon_2 - \epsilon_1)}\right) \tag{B.12}$$

Dividing through with l_a (remember: $l_a \equiv 4\pi/n$) yields

$$\epsilon_{\text{comp}} = \epsilon_1 \left(\frac{n(\epsilon_2 - \epsilon_1)\phi + n\epsilon_1 + (\epsilon_2 - \epsilon_1) - \phi(l_a^{'}/l_a)(\epsilon_2 - \epsilon_1)}{n\epsilon_1 + (\epsilon_2 - \epsilon_1) - (\epsilon_2 - \epsilon_1)q(l_a^{'}/l_a)} \right) \tag{B.13}$$

using $(\epsilon_2 - \epsilon_1) + n\epsilon_1 = (n-1)\epsilon_1 + \epsilon_2$ and $\phi n(\epsilon_2 - \epsilon_1) - q(\epsilon_2 - \epsilon_1)(l_a^{'}/l_a) = \phi(\epsilon_2 - \epsilon_1)(l_a^{'}/l_a)$ to simplify the expression further we arrive at:

$$\epsilon_{\text{comp}} = \epsilon_1 \left(\frac{(n-1)\epsilon_1 + \epsilon_2 + \phi(n - l_a^{'}/l_a)(\epsilon_2 + \epsilon_1)}{(n-1)\epsilon_1 + \epsilon_2 - \phi(l_a^{'}/l_a)(\epsilon_2 - \epsilon_1)} \right) \tag{B.14}$$

assuming $l_a^{'}/l_a = 1$ we arrive at

$$\epsilon_{\text{comp}} = \epsilon_1 \left(\frac{(n-1)\epsilon_1 + \epsilon_2 + \phi(n-1)(\epsilon_2 + \epsilon_1)}{(n-1)\epsilon_1 + \epsilon_2 - \phi(\epsilon_2 - \epsilon_1)} \right) \tag{B.15}$$

This is the expression we set out to derive. It relates the dielectric permittivity of of the compound material to the two dielectric permittivities and the volume fraction taken up by the layer, just like the other two, but it also includes a parameter that controls the shape of the domains ranging from oblate to prolate.

I would like to point to difference in notation used in the two references I have used when working with the Maxwell-Wagner polarisation. I this derivation I have used the notation that Sillars uses in his paper [74]. But in [42] they use the inverse. With that small difference the equations given in [74] and [42] are equivalent, as I will now show.

In Kremer's book, they prefer to give the expression using $n^* = n^{-1}$. To arrive at this expression we simply multiply nominator and denominator with n^*:

$$\epsilon_{\text{comp}} = \epsilon_1 \left(\frac{(n^*n - n^*)\epsilon_1 + n^*\epsilon_2 + \phi(n^*n - n^*)(\epsilon_2 + \epsilon_1)}{(n^*n - n^*)\epsilon_1 + n^*\epsilon_2 - \phi n^*(\epsilon_2 - \epsilon_1)} \right)$$

which gives the expression from [42]:

$$\epsilon_{\text{comp}} = \epsilon_1 \left(\frac{(1 - n^*)\epsilon_1 + n^*\epsilon_2 + \phi(1 - n^*)(\epsilon_2 + \epsilon_1)}{(1 - n^*)\epsilon_1 + n^*\epsilon_2 - \phi n^*(\epsilon_2 - \epsilon_1)} \right)$$

So the expressions given in Sillar's paper and Kremer's book are, in fact, equivalent.

B.5 Trying out the model

Fig. B.2 show the normalised relaxation strength and peak frequency as a function of ϕ for different values of n. It shows that eq. (B.15) can cover both the spherical (setting $n = 3$ restores eq. (3.13)) and layer model, since very oblate domains corresponds to a layer (setting $n = 1$ restores eq. (3.8)).

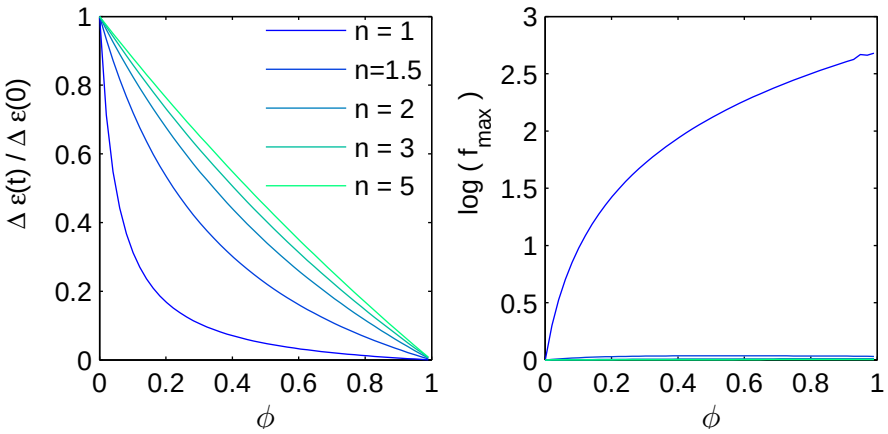

Figure B.2: The normalised relaxation strength and normalised relaxation frequency are influence by the shape parameter, n.

B.6 Concluding remarks

By modelling the shape of the domains it is possible to capture the essence of both the spherical model and the layer model. However, this introduced another fitting parameter into the model.

C | Developing a Cell for Simultaneous Dielectric Spectroscopy and Neutron Diffraction

We developed two prototypes of a sample cell for simultaneous neutron scattering and dielectric spectroscopy. In this appendix I will describe each of the prototypes as well as the reasoning behind the changes made between the first and the second design. I will also suggest further changes to the last prototype.

C.1 Introduction

Part of my work has consisted in developing and testing a cell for simultaneous dielectric and neutron scattering experiments.

Designing and testing a cell is a iterative process. During my Ph.d. I tested two version of the cell – once in 2013 and once in 2016. Both tests will be included in this chapter. A section will de devoted to for each of the prototypes of the cell.

C.2 The 2013 testing

C.2.1 The dielectric cell anno 2013

The cell is an adaptation of the cell that are usually used at LLB to study liquids with neutron diffraction. The cell is a co-centric cylindrical capacitor with a distance of 0.6 mm between the electrodes. See fig. C.1 for a picture of the assembled cell.

The cell consists of three main parts. An outer cylinder, an inner cylinder, and a top piece. All of which are made of aluminium. The top piece is held in place by six screws and is separated from the cylinders by a piece of teflon. To top piece is connected to the inner electrode through a piece of indium that had to be replaced every time the cell was opened. The cell is mounted to a stick through a piece that is also made of teflon.

The cell is loaded by removing the top piece and pouring the liquid down between the two cylinders.

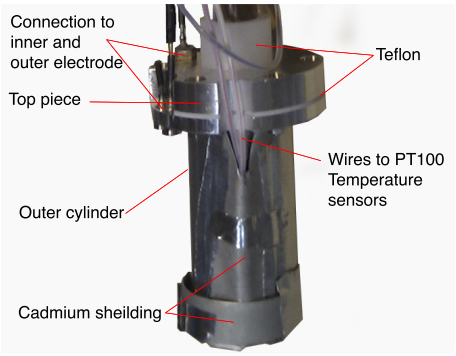

Figure C.1: A picture of the assembled cell used for the 2013 experiments

C.2.2 Protocol and measurements

We did two crystallization runs. One at 130 K and another at 133 K. In both cases the cell was quenched outside the cryostat to liquid nitrogen temperature before being placed in the cryostat which was set at 90 K. The sample was then heated inside the cryostat to the annealing temperature. In all cases the temperature given is the set-point of the cryostat. The actual temperature of the cell was one or two kelvins above the set-point.

C.2.3 Results and discussion

The simultaneous neutron diffraction and dielectric spectroscopy was successful in the sense that we were able to see changes occurring simultaneously. The results are shown in fig. C.2. However, several minor difficulties makes a thorough analysis practically impossible. Some of the difficulties were simply unfortunate events – such as the reactor shutting down and the software controlling the dielectric set-up crashing, but some were more difficult to deal with. In this section I will go through these difficulties and explain how we changed the cell to overcome them.

We had three problems which were not connected to the dielectric cell, but which never the less makes a thorough analysis difficult. The are listed below with descriptions of why they cause a problem.

Intensity fluctuations of unknown origin in the raw neutron data. Our neutron measurements were 'fixed time' measurements. This means that we count the scattered neutrons over a fixed time period. This makes the analysis of the crystallisation kinetics simpler, but it also means that the data has to be normalised to the monitor count (total number of scattered neutrons). After having done this we still saw fluctuations in the (normalised) scattered intensity.

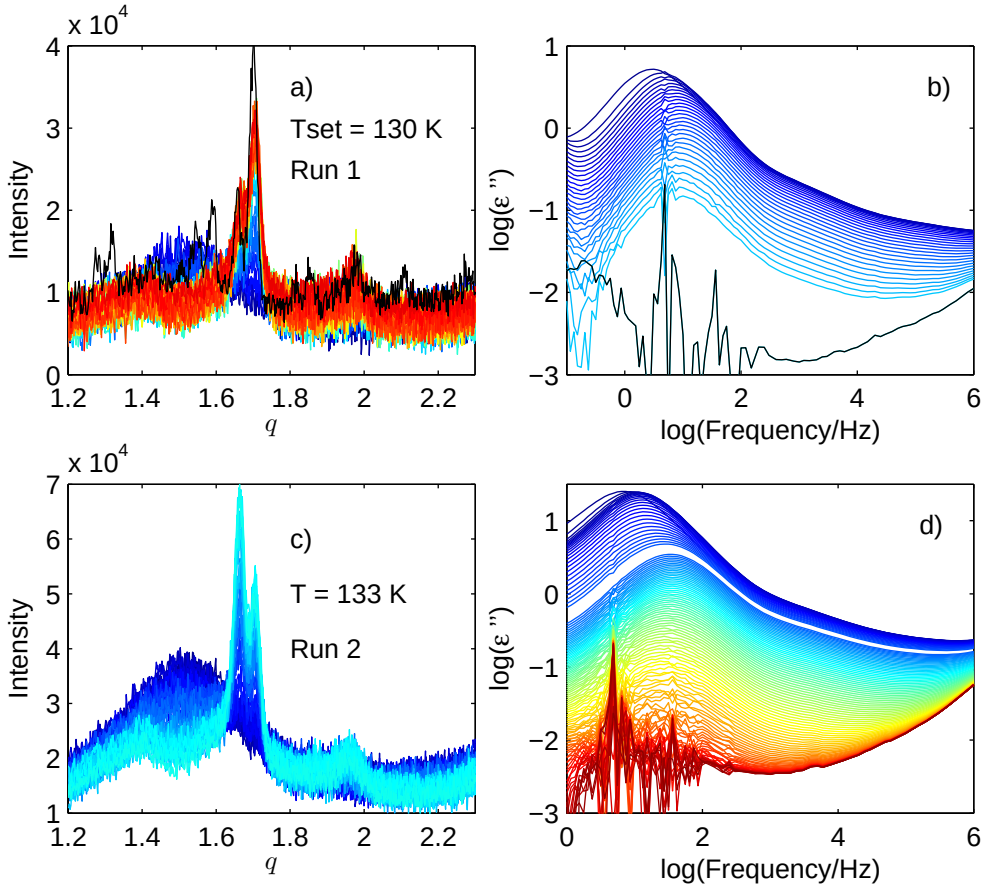

Figure C.2: Cell for simultaneous neutron diffraction and dielectric spectroscopy anno 2013

No neutron measurement of the complete crystal of the second run This makes getting the crystallinity of the sample impossible since the final state is needed in for the fitting procedure.

Dielectric measurements crashed during crystallisation of the first run. This means that we loose a good deal of information about the crystallization kinetics.

The cell also gave rise to some problems. They are listed below together with suggestions for how to solve them.

Increase of the dielectric loss in the 1KHz - 1MHz regime. The origin of this is unknown. It may have been due to some looseness in the wire connecting to the electrodes. We aimed at increasing the reliability of the connection between the stick and the cell while decreasing the likelihood of any unwanted contact between the cell and the stick or cryostat.

Unreasonable level of conduction The top piece was changed to teflon in order to minimise any kind of conductivity that may have been due to contact with the stick. We also decided to use better wires and connectors. A copper spring was used to make the contact between the inner cylinder and the stick. In the 2013 version we used a piece of indium that had to be replaced every time the cell was opened.

Low signal to noise ratio of the neutron data To improve the signal to noise ratio of the neutron data we made the inner cylinder hollow so it could contain liquid. This way the neutron signal should be improved without decreasing the dielectric signal.

Loading the cell was difficult. To make the loading of the cell easier we designed the cell such that it could be loaded through the hollow cylinder in the middle.ă

As the first iteration the results were not too bad. It served as a proof of concept and we identified several problems to solve in the next iteration. Unfortunately this had to wait three years.

C.3 The 2016 testing

C.3.1 The dielectric cell anno 2016

The original cylindrical design of the cell was kept. The cell consists of three main parts. An outer cylinder, an inner cylinder, and a top piece. The top piece is made of teflon while both cylinders are made of aluminium. The distance between the inner and outer cylinder is is 0.6 mm. See fig. C.3 for for a picture of the completely disassembled cell.

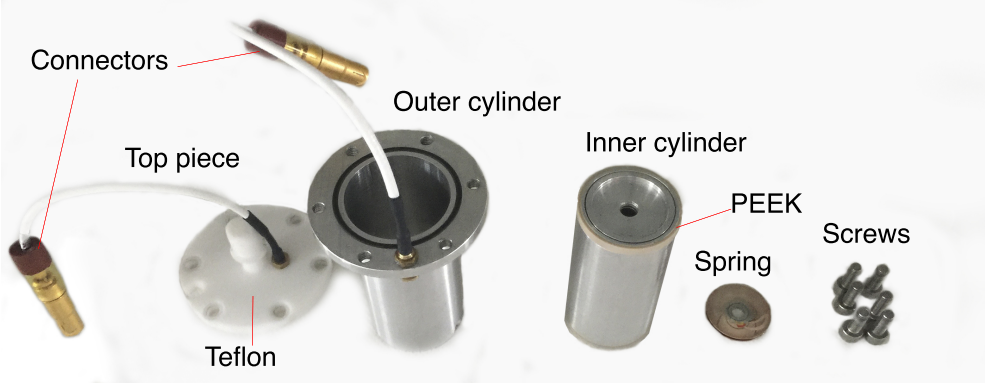

Figure C.3: a picture of the completely disassembled cell used in 2016.

To assemble the cell, the inner cylinder is placed inside the outer cylinder. The spring is placed at the top of the inner cylinder and the top piece is then fastened to the top of the outer cylinder with 6 screws. The cell is connected to the dielectric equipment through the two connectors.

The inner cylinder is itself two co-centric cylinders. The outer part has a diameter of 24.7 mm. It has a hollow inner piece with a diameter of 5 mm. This is the part we fill with liquid. The two pieces are held together with pressure. O-rings are placed between the two parts at both the top and bottom to keep the liquid from seeping into the hollow space between the two parts. Two PEEK spacer are placed at the bottom and top of the inner cylinder to keep the distance between the inner and outer cylinder fixed. The bottom PEEK spacer covers the bottom (except for the hole) of the inner cylinder to avoid contact between the inner and outer cylinder.

The cell has two connectors. The outer cell has a connector welded directly onto the cylinder. A hole is made in the top teflon piece to allow for the passage of the connector. For the inner cylinder a connecters is places on the top teflon piece. This connector has contact to the copper spring which is in direct contact with the inner cylinder.

The cell is loaded by removing the top piece and filling liquid into the centre of the inner cylinder. The liquid will then be sucked into the space between the inner and outer cylinders.

C.3.2 Conclusion of the 2016 experiments

We succeeded in eliminating some of the problems from the 2013 version of the cell. Making the top piece in teflon and improving the connectors seems to have solved some of the conductivity problems we faced in 2013.

However, even with the changes the cell was still extremely unreliable to work with. The dielectric measurements did not work most of the time, which is why we only have dielectric data for two crystallisation runs. Sometimes taking the sample cell in and out of the cryostat was enough to make it work. But other times it would stop working during the crystallisation process. For the future the outer electrode should not be used as the outer cell container – it leads to contact problems.

The hollow space for extra liquid improved the neutron signal and made filling of the cell easier. But unfortunately it also undermines the entire purpose of the simultaneous experiment, because the neutron and dielectric measurement are no longer probing the same sample.

This just goes to show how difficult it is to compare results between different techniques. Following the same temperature protocol is not enough to enable comparison of crystallisation between different different techniques. Small dif-

ferences in the cell design may lead to different effective protocols. It really is necessary to perform the experiments simultaneously and on the exact same sample volume to do compare the results of different techniques.

D | Temperature calibration of cryostats at RUC

In this chapter I investigate the differences in the absolute temperature between cryostats we have at RUC. The investigation was partially motivated by the fact that I used two cryostats when studying the the crystallisation of n-Butanol.

At RUC we have about ten custom build cryostats. Two are cooled by liquid nitrogen and have to be refilled everyday while the remaining cryostats have a cooling pump system that works continuously with no nitrogen required. In addition to the ten cryostats we have a wide collection of sample cells and sample cell holders (sticks). This can lead to differences in the temperature, which has to be corrected if one is interested in comparing results across different sticks or cryostats. See figure D.1 for an example of for different sample cells. afterpage

The differences between the cryostats and the sample cells will influence the absolute temperature inside the cryostat. The aim of this chapter is finding out just how much the absolute temperature is influence by these differences.

In addition to the absolute temperature, the stability of the temperature is crucial when studying the dynamics of supercooled liquids, as well as the kinetics of crystallisation. The temperature stability of the cryostats has been documented in [37] and tested again in [34]. In [34] Hecksher looked at the influence of filling the liquid nitrogen cryostat on the temperature stability. She found it to be a modest effect, that only lasts a couple of minutes, and has a maximum amplitude of ≈ 50 mK. Over a period of 50 hrs the nitrogen cryostat is stable within ≈ 30 mK, while the cooling pump cryostat were stable within a few mK. Thus, we will not worry about the stability of the temperature in this study. However, the numbers are important to keep in mind as they set the limits of our temperature resolution.

Hecksher also looked at the absolute temperature of two of the cryostat (CRYO 3 and 5). She found a difference of 0.35 K between the two cryostats (see [34] p. 238). The experiments were done using the same sample, stick and sample cell.

Here I will build on these investigations by looking at the difference in absolute temperature between six of the cryostats, as well as looking at how different conditions may change the absolute temperature within a cryostat.

We will focus on three main questions:

(a) The stick

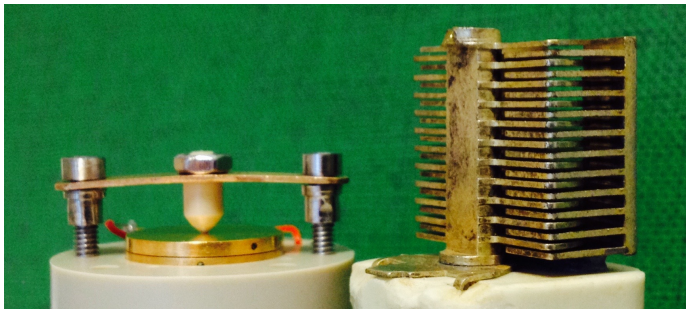

(b) Two dielectric cells

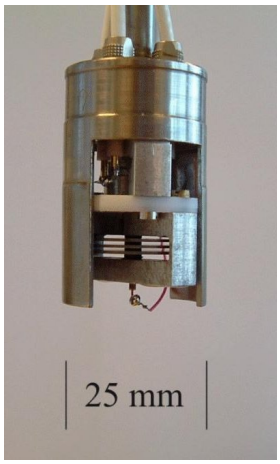

(c) Shear transducer

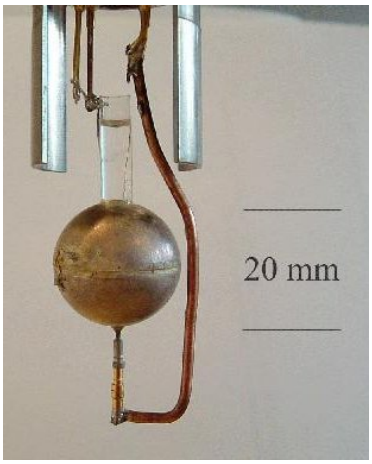

(d) Bulk transducer

Figure D.1: To control the temperature during the experiments we mount a sample holder (b)-(d) onto a stick (a) and put the stick into a cryostat. We have several different sample cells and sticks, which makes for different thermal environments.

1. Can the thermal contact be improved? Should we use grease to increase the thermal contact?
2. How much does changing the sample influence the absolute temperature inside the cryostat?
3. What is the difference in absolute temperature between the cryostats?

These questions will be addressed one at a time in the following sections. But first we must explain how we determine the absolute temperature inside the cryostat.

D.1 Howe we compare temperatures

Essentially the approach amounts to using time-temperature-superpostiion to convert a difference in relaxation time to a difference in temperature. Two identical measurements are made using the same temperature protocol, but while changing the property under investigation. E.g., I use the same stick and sample cell, but clean and refill the cell between two measurements to look for the influence of refilling the cell.

To get the relaxation time, the data around the peak position (± 4 points) are fitted to a second degree polynomial. The peak position is then converted into a relaxation time, τ, by using

$$\tau = \frac{1}{2\pi f_{max}}. \tag{D.1}$$

The relaxation time is then plotted as a function of temperature. For every temperature we then make a linear fit between the current temperature and the next. This defines a line that we expect the relaxation time to fall on, see the inset in fig. D.2.

Defining $\Delta\tau$ as the difference between the line and the measured τ we can find the temperature difference, ΔT, by exploiting the linearity:

$$\Delta T = \frac{\Delta\tau}{a} \tag{D.2}$$

where a is the slope of the line defined by $\tau = aT + b$. The results of this procedure is shown in the inset of fig. D.2. The grey markers and green markers are the uncorrected and corrected data respectively. The example shown is for 230 K.

In the lower right part of fig. D.2 ΔT is shown as a function of temperature. By definition ΔT of $\circ$ is zero, this is the measurement used for the reference fits.

Once we have ΔT as a function of T we can calculate the average ΔT and use this to answer our original questions: How is the temperature inside the cryostat influence by a variety of factors.

The data from the measurement at 225 K is not used in the following analysis since the imperfect calibration of the two multimeters cause a spike in the data. This spike leads to an uncertainty in the relaxation time which translates into a wrong estimation of the differences in temperature. The data are shown in the figures nevertheless.

D.2 Changing the sample and testing the thermal contact

For these tests we measured on the liquid DC704 between 240 K and 215 K in steps of 5 K. The same protocol was used for all the experiments.

To investigate the influence of the thermal contact we have compared measurements with and without covering the wings of the stick with DC704. The idea is that the DC704 should increase the thermal contact between the stick and the copper tube inside the cryostat.

The data have been tread as describe above and the results are show in figure D.2 and D.3.

There appears to be no temperature dependence of ΔT. This is good since we are using our cryostats in a wide range of temperatures, and using a single ΔT to scale the data from different cryostats is convenient.

The average ΔT is $\approx$ 100 mK on changing the sample, see figure D.2. In principle, there is no reason why refilling the sample cell should change the absolute temperature. However, water uptake or other impurities may affect the dynamics.

Upon greasing the wings of the stick we see a ΔT of $\approx$ 50 mK.

The average difference in absolute temperature between two consecutive measurements is a couple of mili Kelvin, see figure D.3. This is consistent with what Hecksher from in her investigation of the temperature stability of the of the cooling pump cryostats.

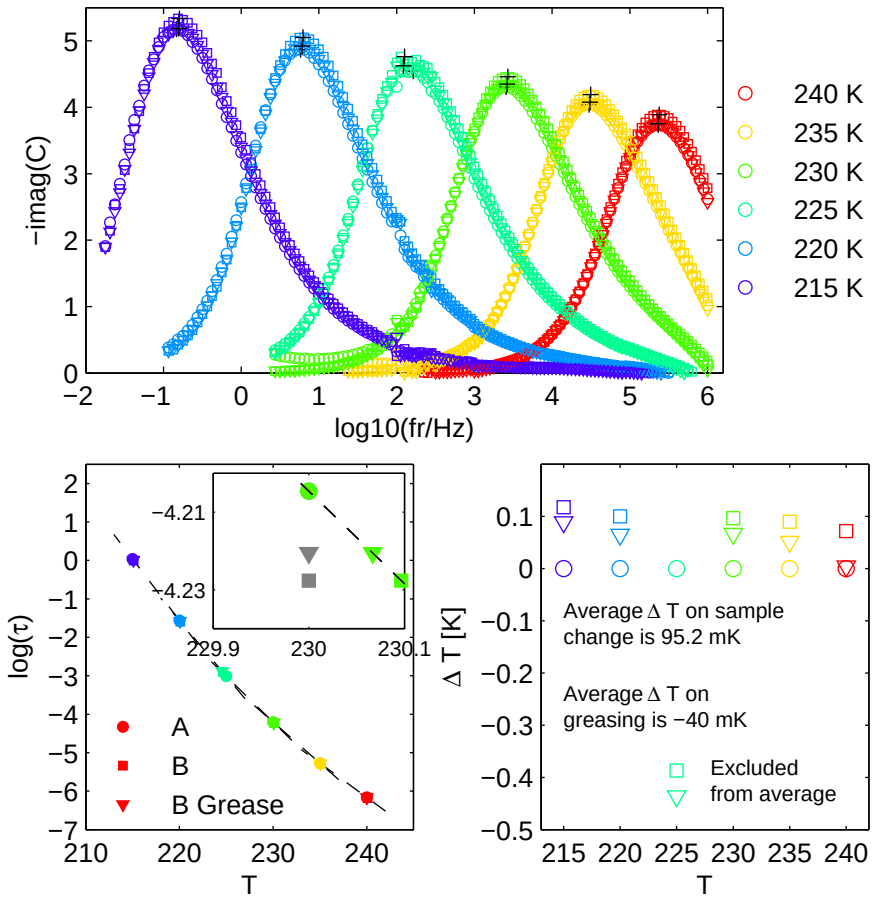

Figure D.2: CYRO 11 (Tina's). On changing the sample we see an average temperature difference from the reference measurements of of $\approx$ 100 mK. On greasing the average is changed by $\approx$ 50 mK.

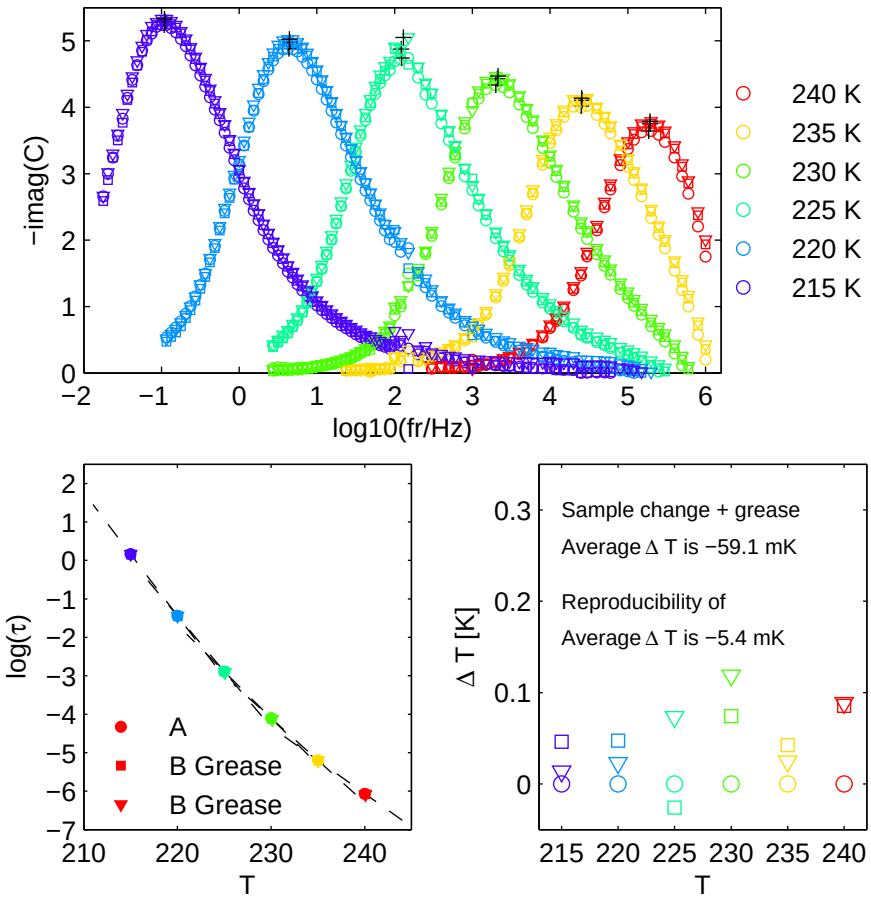

Figure D.3: CRYO 5 (Bo's). The average change in absolute change in absolute temperature by changing the sample and greasing it is ≈ 50 mK. This is consistent with what we saw in CRYO 11. The resolution in absolute temperature appears to be ≈ 50 mK, since this is the difference we get from two identical measurements.

D.3 Comparing the different cryostats

The results are shown in figure **??**. The calculation are done as described above, with the only difference being we compare cryostats rather than sample refill and cell changes. For this purpose CYRO 11 was used as a reference.

The average change in absolute temperature is ≈ 250 mK. When calculating the average I used at the absolute difference in ΔT. We have excluded CYRO 4 from this average since it is clearly an outlier.

It is unclear why the difference between CYRO 11 and 4 is so large. A difference of ≈ 1.2 K. It is much larger than we expect, and if we consider the difference between CYRO 3 and 4 is approaches 2 K.

D.4 Conclusion

In conclusion the effects on the absolute temperature in decreasing order of importance are:

Changing the cryostat: On average the differences in absolute temperature is 200 mK. However, depending on which cyrostat you are using, you may see differences in the order of kelvins.

Changing the sample: Leads to a change on the order of 100 mK. These effects must be due to impurities and/or water uptake. It should be possible to reduce this effect by being very careful with the handling of the sample.

Greasing the wings of the stick: Leads to $\Delta T \approx 50$ mK.

Precision of measurement: Repeating the same frequency-temperature-protocol without the sample leaving the cryostat leads to $\Delta T \approx 5$ mK. This then, is the precision of our measurements.

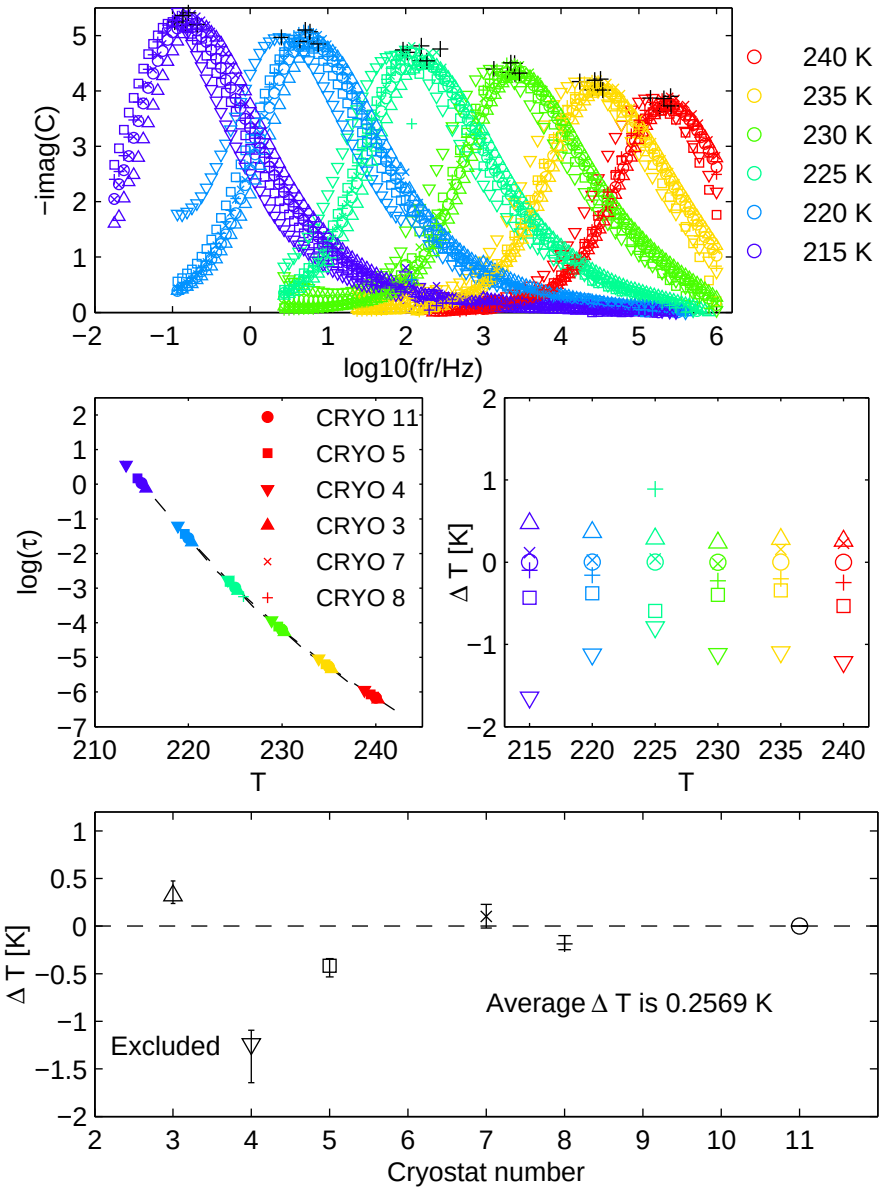

Figure D.4: The average change in absolute temperature between the cryostats is 200 mK. This is of the same order of magnitude as the difference of 350 mK Hecksher found between CYRO 3 and 5. However, depending on which cryostats you use, you may see differences on the order of 1 K.

E | Backscattering on glycerol water mixtures

In December 2015 Christiane Alba-Simionesco, Frédéric Caupin, and I had a beamtime at IN16B at ILL. The results are presented here because I did not have time to do a thorough analysis of the data.

E.1 Background and Aim

The aim of this experiment was to study the changes in the dynamics during the transformation of the glycerol/water mixture. The idea was that if the sample transformed from one liquid state to another it should give a signal in the dynamics.

E.2 Sample and Temperature Protocol

Three isotopic mixtures of glycerol-water at $c_g = 0.178$ molar concentration were used: 1) $C_3H_5(OD)_3 + D_2O$ 2) $C_3D_5(OH)_3 + H_2O$ 3) $C_3D_5(OH)_3 + H_2O$. We did three kids of experiments. The first are annealing experiments similar to what we reported for the diffraction and small angle experiments in chapter 5. The second are temperature scans, where we measure the elastic and inelastic off-sets as a function of temperature. The last experiments are full scans at a few selected temperatures.

E.3 Results

E.3.1 Annealing

We wanted to see how the spectrum changes during the crystallisation. We expected to see a change from quasi-elastic scattering in the liquid state to elastic scattering in the crystalline state with a possible transition from liquid I and liquid II in between. We followed a temperature protocol similar to the one used under the small angle scattering experiments, that is, a quick quench followed by heating to heating to the annealing temperature. The exact temperature protocols are shown together with the data in figs. E.1 and E.2. We measured the elastic peak as well as three energy off-sets: 2, 5 and 10 μeV.

In fig. E.1 I show the sum over all detectors as a function of time for both sample B and D. There is no change in the total scattered intensity of the elastic signal. For the inelastic signal the signal to noise ratio is high, which

makes small changes impossible to see. So, we see no signs of crystallisation for either of the samples in the 140-180 K range. These results are at odds with our diffraction and small-angle scattering results where we saw clear signs of crystallisation in this temperature range.

Since we are averaging over all the detectors we are averaging over a wide q-range. So some of the changes may have been averaged out. Therefore I have focused on the single detector that measured the scattering at the angle corresponding to $q \approx 0.19$ 1/Å. In the small angle scattering we saw a large increase in the scattering intensity at this q-range. In this q-range we see a 5% increase of the scattering in sample D and a 15% increase of the scattering in sample B. So we see only a very weak sign of crystallisation. This is despite the fact that we are in the temperature range of 160-170 K where we saw crystallisation in the diffraction and small-angle experiments. This just confirms the difficulty of comparing results across different experimental techniques.

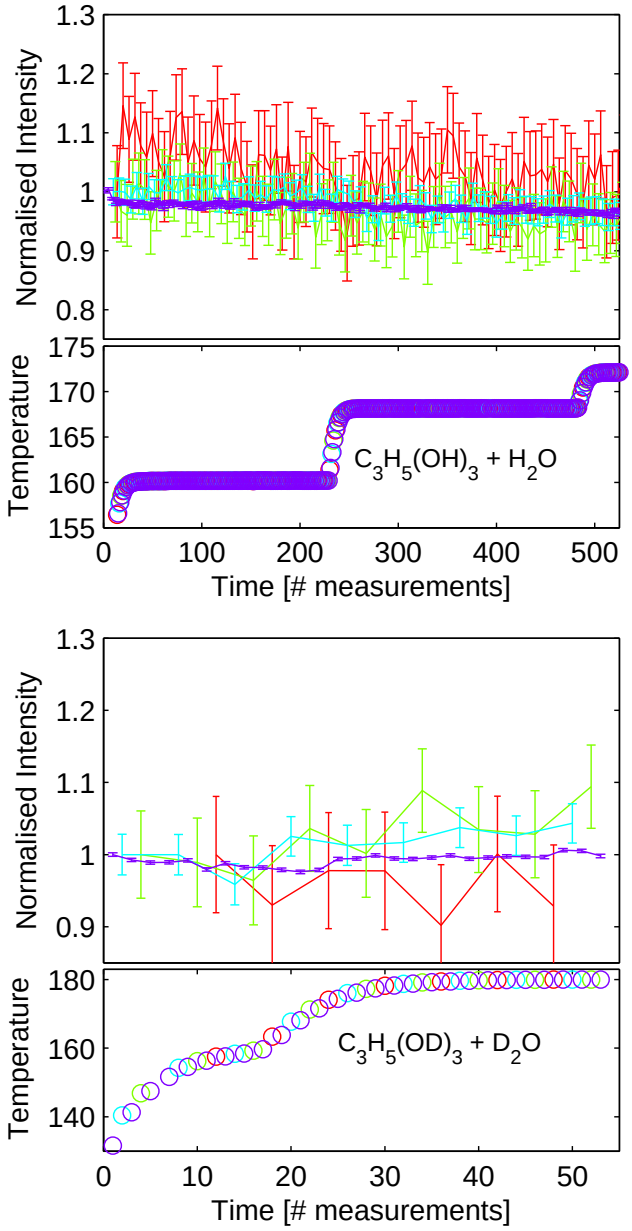

Figure E.1: Looking for signs of crystallisation. Here we are still looking at the sum of all the detectors. It is clear that the signal to noise ratio of the inelastic scans is too bad to see any systematic change.

E.3.2 Temperature scans

Because of the annealing results we decided to do temperature scans to see when changes would occur in the sample. We have performed temperature scans while

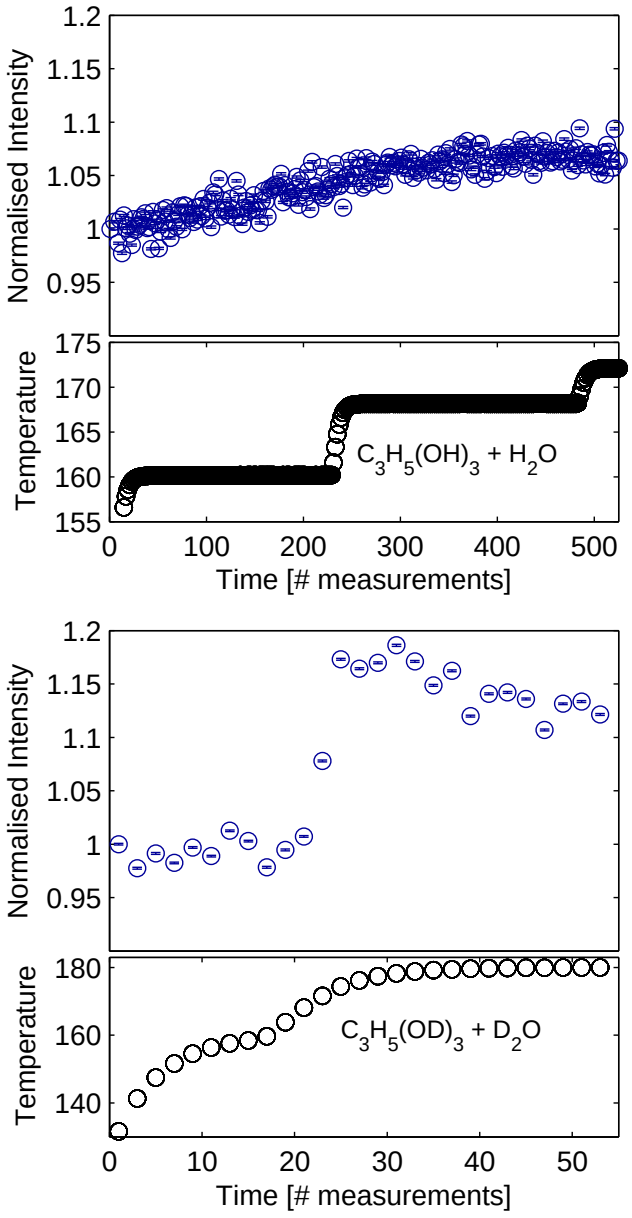

Figure E.2: Looking for signs of crystallisation at the first detector which corresponds to $q \approx 0.19$Å. In this range we see changes to the scattered intensity.

measuring the elastic peak as well as three energy off-sets (2, 5 and 10 μeV). The sample was quenched to 60 K, heated to 300 K and subsequently cooled back to 160 K before heating back to 300 K. The temperatures are are shown in the insets of fig. E.3.

As the temperature is increased the elastic scattering decreases. This is to be expected since the material becomes softer with increasing temperature. At the same time as the elastic scattering decreases the in-elastic scattering increases. So what we see is the broadening of the dynamic structure factor.

Looking at the elastic and inelastic fixed window scan summed over the entire q-range show no signs of crystallisation, see fig. E.3. This is surprising since our experience from the small-angle experiments was that a fast quench was necessary to avoid crystallisation on cooling.

What we do see in the temperature scans is a clear hysteresis effect in seen as there is a difference between the cooling and heating curves. There appear to be no difference between heating from a quench or heating from a slow cooling.

Once again we can look at just a single detector to get q-specific information about the sample. We see that in this q-range there is a difference between heating after a quench and heating after a slow cooling. However, this small bump around 180 K does not seem to be a sign of crystallisation, since the intensity quickly drops back to the level of the other curves.

Finally we can compare temperature scans for the different isotopic mixtures. This helps us understand how different parts of the molecules are reacting to the temperature changes.

The annealing experiments can be summarised in the following way: The heating curves for the total scattered intensity are identical irrespective of the cooling protocol followed. We see a difference at low q, but not a major one.

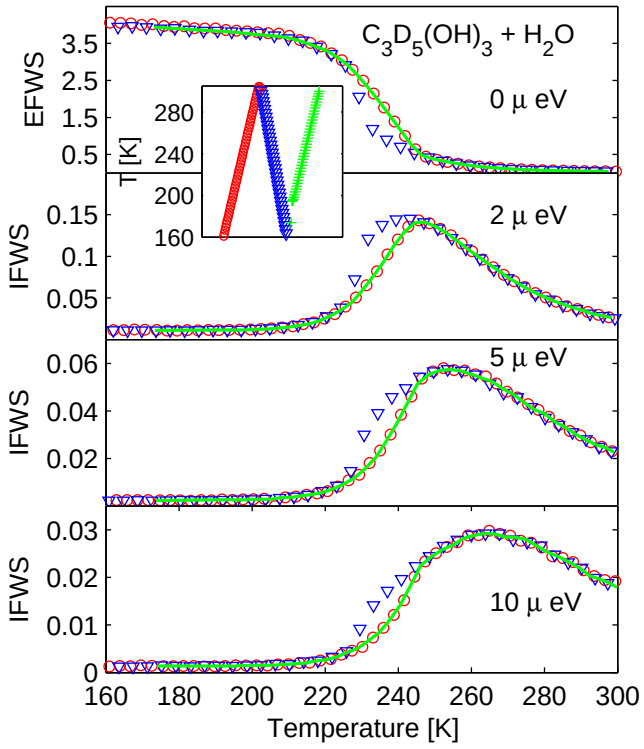

Figure E.3: Elastic and inelastic fixed window scan from IN16B where the intensity of summed over all detectors (i.e. all q-values). The inset shows the exact temperature protocol. The red curve is the measurement on heating after a quick quench. The blue curve is the slow cooling after melting and the green curve is the heating after the slow cool. Measurements on heating are the same irrespective of cooling protocol.

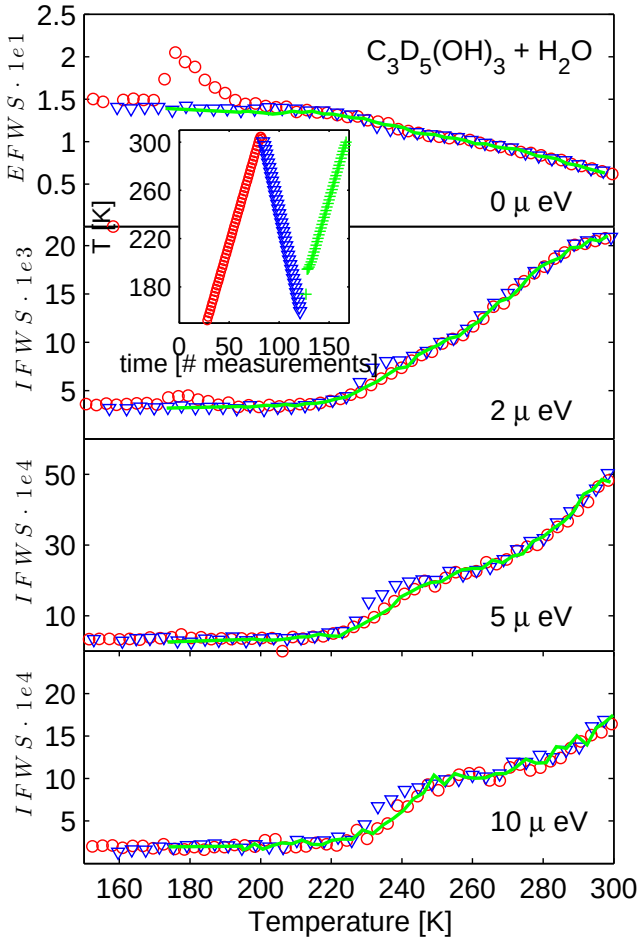

Figure E.4: Elastic and inelastic fixe d window scan from IN16B where the intensity of summed over A single detector. The inset shows the exact temperature protocol. Measurements on heating are the same irrespective of how the crystal was obtained.

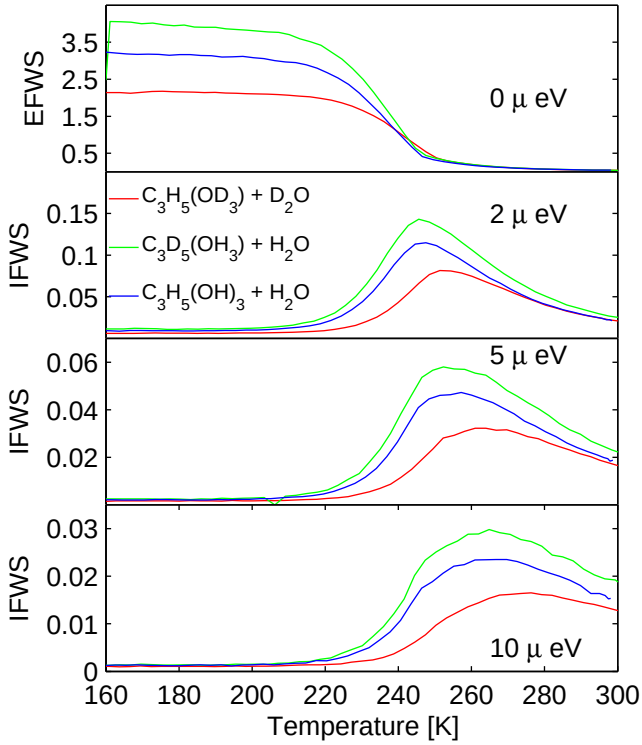

Figure E.5: Elastic and inelastic fixed window scan from IN16B where the intensity of summed over all detectors (i.e. all q-values). The samples were quenched to 70 K and the cooled further to 2 K before heating to room temperature. Comparing the temperature scans of the different samples

E.3.3 Full QENS scans

Since we hard a hard time making the sample crystallise, we decided to measure the full spectrum at a few temperatures. By doing a full scan we are measuring the dynamic structure factor $S(q, \omega)$. The following is raw data. No background has been subtracted. A broadening of $S(q, \omega)$ means a shorter relaxation time. We see a broadening with increasing temperature which is to be expected.

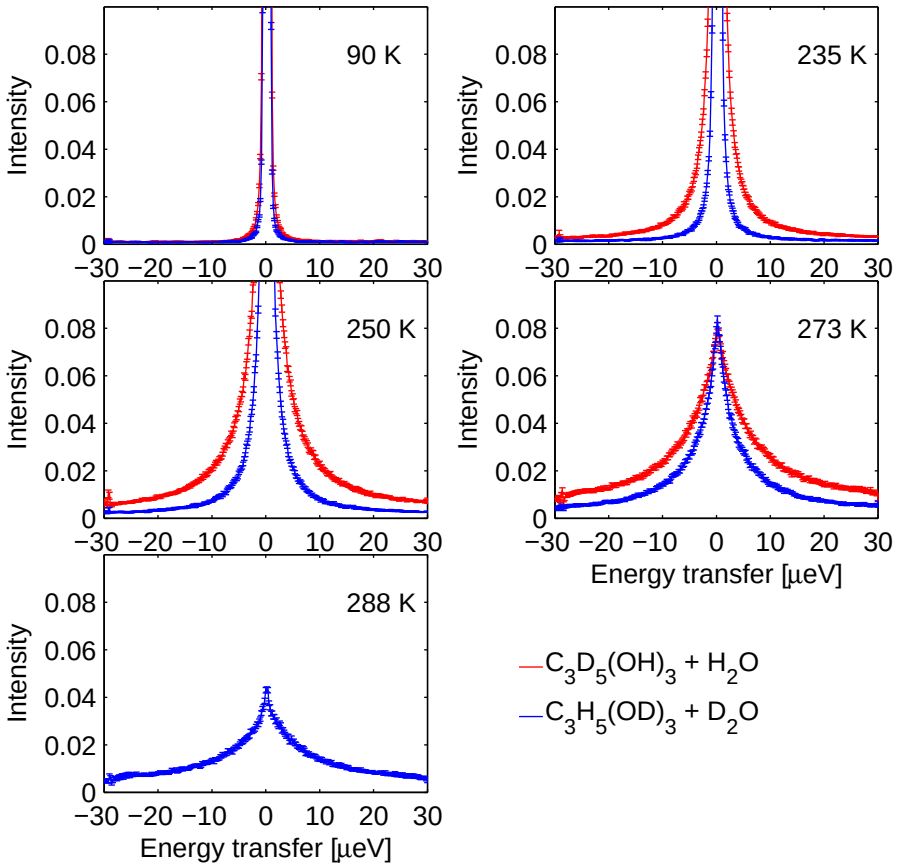

Figure E.6: For both samples a broadening with temperature is observed. The dynamic og the end-group of glycerol and the water are generally faster than the dynamics of the back-bone og glycerol.

For both samples a broadening with temperature is observed. The dynamic og the end-group of glycerol and the water are generally faster than the dynamics of the back-bone og glycerol.

Once again it is interesting that we do not see crystallisation. The melting temperature of the $c_g = 0.178$ mixture is around 250 K. Each measurement takes roughly thee hours, so in total we spend at least three hours at a temperature

for which crystallisation should occur.

E.4 Summary of IN16B experiments

The annealing experiments on the fully protonated sample showed an increase in the elastic scattering. As crystals scatter more elastically than liquids, this is consistent with crystallisation occurring in the liquid. The changes are most pronounced for the lowest q-values. The temperature scan experiments show the difference between slowly cooling and quenching the sample before heating it, but no signs of crystallisation.

F | The paper

A systematic study of the isothermal crystallization of the mono-alcohol n-butanol monitored by dielectric spectroscopy

M. H. Jensen, C. Alba-Simionesco, K. Niss, and T. Hecksher

Citation: The Journal of Chemical Physics **143**, 134501 (2015); doi: 10.1063/1.4931807
View online: http://dx.doi.org/10.1063/1.4931807
View Table of Contents: http://scitation.aip.org/content/aip/journal/jcp/143/13?ver=pdfcov
Published by the AIP Publishing

THE JOURNAL OF CHEMICAL PHYSICS **143**, 134501 (2015)

A systematic study of the isothermal crystallization of the mono-alcohol *n*-butanol monitored by dielectric spectroscopy

M. H. Jensen,[1,2] C. Alba-Simionesco,[2] K. Niss,[1] and T. Hecksher[1,a)]
[1]*Department of Sciences, DNRF Centre Glass and Time, IMFUFA, Roskilde University, P.O. Box 260, DK-4000 Roskilde, Denmark*
[2]*Laboratoire Léon Brillouin, CNRS CEA -UMR 12, DSM IRAMIS LLB CEA Saclay, 91191 Gif-sur-Yvette Cedex, France*

(Received 23 June 2015; accepted 14 September 2015; published online 2 October 2015)

Isothermal crystallization of the mono-hydroxyl alcohol *n*-butanol was studied with dielectric spectroscopy in real time. The crystallization was carried out using two different sample cells at 15 temperatures between 120 K and 134 K. Crystallization is characterized by a decrease of the dielectric intensity. In addition, a shift in relaxation times to shorter times was observed during the crystallization process for all studied temperatures. The two different sample environments induced quite different crystallization behaviors, consistent and reproducible over all studied temperatures. An explanation for the difference was proposed on the background of an Avrami analysis and a Maxwell-Wagner analysis. Both types of analysis suggest that the morphology of the crystal growth changes from a higher dimension to a lower at a point during the crystallization. More generally, we conclude that a microscopic interpretation of crystallization measurements requires multiple probes, sample cells, and protocols. © *2015 AIP Publishing LLC.* [http://dx.doi.org/10.1063/1.4931807]

I. INTRODUCTION

All liquids can be supercooled.[1–3] In fact, crystallization rarely takes place exactly at the melting temperature upon cooling, because the crystal nuclei formed dissolve before they grow to a stable size.[4] Some liquids, like water, crystallize readily at moderate supercooling and need fast quenching below the melting temperature in order to avoid crystallization.[5] In fact, water is so prone to crystallization that there is a broad range of temperatures — the "no-man's land"— where the supercooled liquid state is inaccessible for the bulk liquid.[6,7] Other liquids, like the prototype glass-former glycerol, supercool easily and require a careful protocol to crystallize.[8] But the true thermodynamic equilibrium state for all supercooled liquids and glasses is unarguably the crystal, and thus, crystallization is their eventual inevitable fate.

For many applications, the life-time of the glassy or meta-stable liquid state is a key issue and the ability to predict and control crystallization properties is desired. But understanding the crystallization process is also interesting from a fundamental point of view. Crystallization studies are however difficult to carry out in a controlled and reproducible manner, because many factors influence the initiation and course of crystallization, such as sample preparation, thermal history, presence of impurities, and container geometry.[8–10]

We present here a thorough dielectric study of the crystallization process in supercooled *n*-butanol considering a minimum of external parameters. Dielectric spectroscopy is a convenient and fairly common probe for studying crystallization kinetics in real time, see, e.g., Refs. 11–16. The sign of crystallization is a decrease in intensity of the signal, and the crystal concentration of the sample is often obtained by assuming that the relaxation strength is proportional to the volume fraction of liquid in the sample.[17–19] But the microscopic interpretation of dielectric spectra is not straightforward,[20] especially when studying a heterogeneous mixture.

Supercooled *n*-butanol has an intense low-frequency dielectric signal — the so-called Debye-process — characteristic of many monohydroxyl alcohols.[21] It also exhibits a slow crystallization process upon reheating after a rapid quench below T_g.[22,23] At 10 K above the glass transition temperature, the crystallization can take several days to finish. These two properties, a large dielectric signal and slow crystallization, make *n*-butanol an ideal candidate for monitoring isothermal crystallization in real time by dielectric spectroscopy. Crystallization of *n*-butanol has previously been studied with x-ray diffraction,[22,23] Raman spectroscopy,[24,25] calorimetric methods,[26] and phase contrast microscopy.[27] The focus of these studies was primarily on the curious "aborted crystallization" at temperatures close to the glass transition temperature. In the present study, our main focus is not the mechanism of the aborted crystallization, but rather to explore the potential of dielectric spectroscopy for monitoring crystallization on a well-studied crystallizing substance, varying only a small subset of the parameters that influence the crystallization process.

Thus, we used two different dielectric measuring cells with different geometries and different electrode materials and studied a range of temperatures close to T_g. Measurements from different cells give information about what observations are intrinsic to the sample and what effects should be ascribed to the macroscopic boundary conditions. Measurements at many different temperatures evidently give the temperature

a)tihe@ruc.dk

dependence of crystallization and relaxation times, but in addition, they serve as a consistency and reproducibility check.

II. EXPERIMENT AND MATERIALS

All measurements were carried out in the same experimental setup (described in detail in Ref. 28), including a custom-built nitrogen cryostat capable of keeping the temperature stable within 50 mK over weeks. Two different sample cells were used. Cell A is a 22-layered gold-plated parallel plate capacitor with 0.2 mm between each set of plates and a geometric capacitance of 65 pF. Each plate is a semi-circle which can be rotated to overlap each other (identical to the capacitors used in old radios). Cell B is a parallel plate capacitor with circular beryllium-copper plates separated by 50 μm sapphire spacers and a geometric capacitance of 17.6 pF. The cells are sketched in Fig. 1.

The sample *n*-butanol (T_m = 183 K, $T_g \approx$ 110 K) was purchased from Sigma Aldrich's at >99.9% purity and used without further purification.

The same protocol was followed for each crystallization measurement; a new sample was quenched to 85 K (roughly 25 K below T_g) and kept at this temperature for (at least) 120 min, then heated to the target temperature where the crystallization process was followed. The heating took less than 5 min. Frequency scans were made continuously as soon as heating from 85 K initiated and until no further changes in the spectrum occurred. The frequency range of the scans was adjusted for each temperature to keep the scan as short — and thereby as fast — as possible, while still keeping both ϵ_∞ and ϵ_s in the frequency window. The sample cells were emptied and cleaned between each measurement.

Isothermal crystallization was followed at 15 different temperatures between 134 and 120 K. The exact temperatures in Kelvin are 134, 133, 132, 131, 130, 129, 128.5, 127.5, 126, 125, 124, 123, 122.5, 121, and 120. The 133 K measurement has only been done with cell A, while the 132 K measurement has only been done with cell B. For reference, a fully crystallized sample was made by quenching to 85 K and reheating to 170 K, and a spectrum of the crystal was measured at all temperatures included in the study.

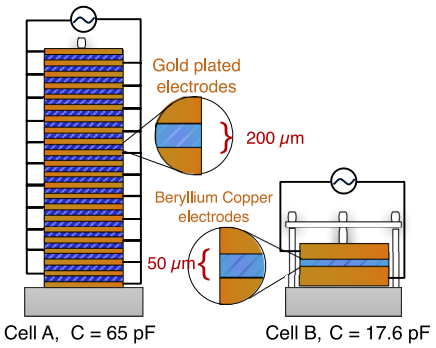

FIG. 1. Schematic drawings of the two cells used for the crystallization studies. Cell A is a multi-layer capacitor with gold plated electrodes (variable capacitor type used in old fashioned radios) with a geometric capacitance of 65 pF. Cell B is a two-plate capacitor with beryllium copper electrodes and 50 μm sapphire spacers. Cell B has a geometric capacitance of 17.6 pF.

III. EXPERIMENTAL RESULTS AND DATA ANALYSIS

A. Phenomenological fits of the spectra

In *n*-butanol, there are three visible processes — Debye, alpha, and beta processes — in the measured frequency window, see Fig. 2(a). The crystallization, signaled by a decrease of relaxation strength, also induces a shift in the loss peak for the three processes. To quantify how the crystallization influences each of these processes, we fitted

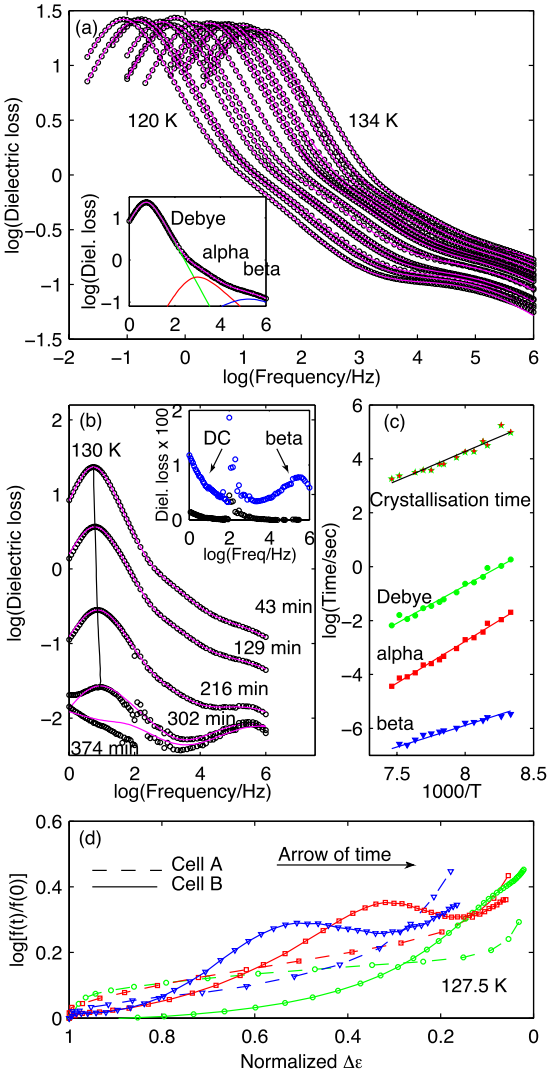

FIG. 2. Fitted spectra and time and temperature dependence of the fitting parameters. (a) The first measurement at every temperature, presumably before crystallization initiates. The magenta lines are fits described in the text. The inset shows the three relaxation processes constituting the fit: the Debye (green), alpha (red), and beta (blue) processes. (b) Selected spectra during crystallization at 130 K, using cell B. Again, magenta lines are fits. The inset shows the dielectric loss of the last measurement (blue), together with the measurement of the full crystal (black), on a linear scale. The "spike" at 100 Hz is an experimental artifact deriving from a non-perfect match between two voltmeters. (c) The fitted relaxation times together with the crystallization time. The lines are linear fits. (d) Parameterised plot of the logarithm of the normalized relaxation frequency ($\log\{f(t)/f(0)\}$ with $f = 1/\tau$), against the normalized relaxation strength $\Delta\epsilon$, for each of the three processes. The two cells display quite different behavior during crystallization.

the spectra to a sum of three relaxation processes. Since the processes are not well separated, we aimed at limiting the number of free fitting parameters by the following procedure: First, the Debye process is fitted by a Cole-Cole function. The Debye process broadens during the crystallization, and thus, a pure exponential function would not give a good fit. The result of the Debye fit is then subtracted from the data and the alpha and beta processes are fitted simultaneously as a sum. The beta process is fitted to a Cole-Cole function with a fixed shape parameter, $\beta = 0.45$. The alpha process is fitted to a dielectric version of the Extended Bell (EB) model (see Ref. 29) in which the dielectric constant is given by

$$\epsilon_{\mathrm{EB}} = \epsilon_\infty + \frac{\Delta\epsilon}{1 + \frac{1}{(1+i\omega\tau_\alpha)^{-1} + k_\alpha (i\omega\tau_\alpha)^{-\alpha}}}, \quad (1)$$

where ϵ_∞ is the high-frequency plateau of the real part, $\Delta\epsilon$ is the relaxation strength, τ_α is the relaxation time, k_α controls the width of the peak, and α gives the high-frequency power law behavior of the alpha peak. This model for the alpha relaxation gives good fits even when the shape parameters are fixed such that only the relaxation strength and relaxation time are fitted. The slope parameter was fixed to $\alpha = 0.5$[30] and the width parameter to $k_\alpha = 1$. The Cole-Davidson function resulted in poorer fits, even with the shape parameter varying freely. In total, we fitted the imaginary part with seven parameters: a relaxation time, τ_x, and a relaxation strength, $\Delta\epsilon_x$, for each process (x denoting Debye, alpha, or beta), and a broadening parameter for the Debye process.

The procedure gives excellent fits over the frequency range explored as shown in Fig. 2(a), where the first dielectric spectrum at every annealing temperature is shown as well as the fits resulting from the described fitting procedure. The inset shows a spectrum at 130 K with each of the individual fitted relaxation processes.

The same fitting procedure was applied to the isothermal crystallization spectra to study the temporal evolution of the three processes during crystallization. The resulting fits are illustrated in Fig. 2(b) showing a subset of the measured spectra at 130 K using cell B. As the crystallization proceeds, the strength of the Debye and alpha relaxation processes decreases continuously to disappear entirely by the termination of the crystallization process. This is also to be expected, since there should be no large-scale rearrangement of the molecules in the crystal. The beta relaxation process, however, remains active at the termination of the crystallization process. The inset of Fig. 2(b) shows the last scan at 130 K (where no further changes in the spectrum occurred) together with the spectrum of the fully crystallized sample at the same temperature. For the full crystal, the signal has virtually vanished, while the last scan of 130 K still displays dynamical features, thus clearly demonstrating that the crystallization process stops before the sample is fully crystallized and that there is still some molecular mobility left, as reported in Refs. 22–27. The results from the fitting routine establish the general behavior of the spectra during the crystallization, but we refrain from analyzing the finer details, especially towards the end of the crystallization process, where Debye and alpha processes have vanished and the fits become unreliable (see, e.g., the lowest curve in Fig. 2(b)).

Using the relaxation strength, $\Delta\epsilon$, as an indicator of the degree of crystallinity, we define a characteristic crystallization time as the time for $\Delta\epsilon$ to decay to half of its initial value. Figure 2(c) shows the crystallization time derived from both Debye and alpha relaxation strengths as a function of inverse temperature, and it is evident that the two measures are identical within the accuracy of our measurements.

Along with the crystallization time, we show the relaxation times obtained from the fits to the first (uncrystallized) spectrum. Clearly, the Debye, alpha, and beta processes as well as the crystallization process are all slowed down with decreasing temperature, and consequently, the different characteristic time scales would all appear to be correlated (at least in this temperature range), but it does not necessarily imply any causation. For the studied temperature span, all the shown time scales are Arrhenius within the noise, although with very different pre-factors.

Focusing now on how the two sample environments influence the crystallization process, we define the relaxation frequency as the inverse of the fitted relaxation times, $f = 1/\tau$. The evolution of both the relaxation strength and relaxation frequency differs for the two cells. Fig. 2(d) shows a parameterised plot of the logarithm of the fitted relaxation frequency (normalized to the initial value) as a function of the fitted normalized relaxation strength for each of the three processes from measurements at 127.5 K with both cells A and B. In cell A, there is a shift in the relaxation frequency, f, quite early in the crystallization process, then it remains relatively unchanged for all three relaxation processes until an increase sets in again towards the end of the crystallization. In cell B, the shift in relaxation frequency is more gradual. For the Debye process, the shift is monotonous, but for the alpha and the beta processes, the shift displays a non-monotonous behavior. The curve peaks in Fig. 2(d) occur roughly the same waiting time for the alpha and beta processes.

The different progresses of the crystallization process for the two cells suggest a macroscopic/mesoscopic rather than microscopic explanation since a slight difference in sample geometries is not expected to affect the behavior of individual molecules.

The full set of fitted parameters normalized to the initial value is shown as a function of waiting time in Fig. 3. The colors of the curves indicate the temperature with blue being the lowest (120 K) and red being the highest (134 K). In both cells, lower temperatures lead to longer crystallization times, as was shown in Fig. 2(c).

For cell A (Fig. 3(a)), the temporal evolution of the relaxation strengths for each of the three processes appears similar, except at long waiting times, where the beta relaxation strength levels off at ~0.08 instead of decaying all the way to zero. The final level for the beta relaxation is marked by a dashed line in the third panel of Fig. 3(a). For cell B (Fig. 3(e)), the Debye and alpha relaxation strengths follow each other until roughly halfway through the crystallization, where a shoulder emerges in the alpha relaxation strength curve, which then proceeds like a two-step relaxation. As in cell A, the beta relaxation strength does not decay to zero and levels off at the same value as for cell A. Comparing Figs. 3(a) and 3(e), we see that the curves for cell B are significantly less

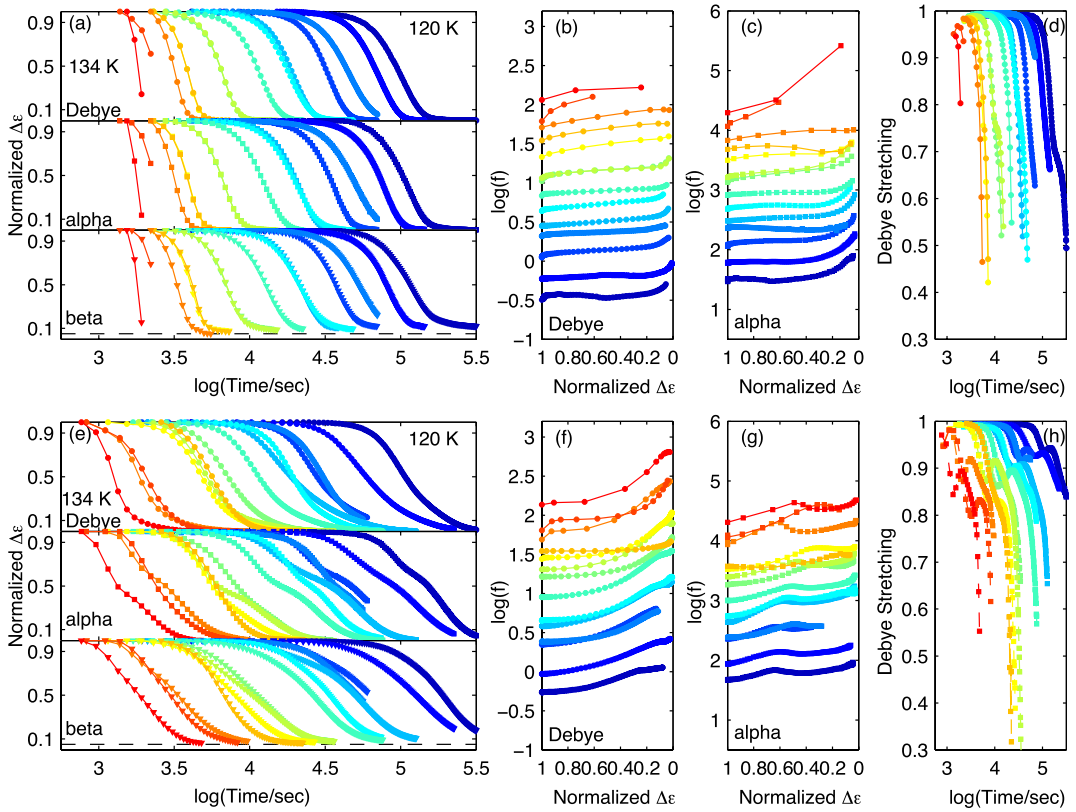

FIG. 3. Parameters for the fitted isothermal crystallization spectra of *n*-butanol for temperatures between 120 K and 134 K. The colors of the curves indicate the temperatures with blue being the lowest temperature and red the highest. 133 K has only been done with cell A while 132 K has only been done with cell B. Notice that the crystallization process takes longer to finish in cell B. (a), (e) The normalized relaxation strengths defined as $\Delta\epsilon(t)/\Delta\epsilon(0)$ of the Debye, alpha, and beta processes for cells A (a) and B (e) as a function of logarithmic time. (b), (c), (f), (g) The logarithm of the relaxation frequency ($f = 1/\tau$) as a function of the normalized relaxation strength for cell A (b), (c) and cell B (f), (g). (d), (h) The broadening parameter of the Debye process. All fitted values start at 1 (corresponding to a pure exponential) and then gradually drop to ~0.5. For cell A (d), the broadening is monotonous while for cell B (h), there is a local minimum followed by a maximum for all studied temperatures.

compressed than the corresponding curves for cell A, which means that crystallization proceeds at a consistently slower rate in cell B compared to cell A. Consequently, our definition of crystallization time may give roughly the same for the two cells, but the time it takes before crystallization stops is much longer in cell B.

Figures 3(b), 3(c), 3(f), and 3(g) show the logarithm of relaxation frequencies as a function of normalized relaxation strength. The relaxation frequency of the beta process is not shown, because it does not vary in a systematic way, making further interpretation unjustified. In cell A, the general behavior is that the relaxation frequencies have a slight shift to higher frequencies at the onset of the crystallization, but only increase a little during the remainder of the crystallization. In cell B, the relaxation frequency of Debye and alpha processes does not change in the beginning of the crystallization process, but shifts gradually to higher frequencies. A "bump" occurs in alpha relaxation strength around a normalized relaxation strength of 0.5, showing that the behavior observed in Fig. 2(d) is general.

Last, Figs. 3(d) and 3(h) show the broadening parameter of the Debye process as a function of time. All curves start at the value 1 (corresponding to a pure exponential) and then decay to around 0.5 by the end of the crystallization. Again, we see curve shapes that are similar for measurements in the same cell at all temperatures, but differences between the two cells: in cell A, the gradual broadening is monotonous, while in cell B, we first see a broadening, then narrowing and finally a broadening again. A non-monotonous behavior was also seen in the time evolution of the relaxation frequency of the alpha process.

The differences between the two cells are thus reproduced for all the studied temperatures. One possible mesoscopic explanation for the observed difference in the evolution of the relaxation strength and relaxation times for the two cells could be that the two cells induce different kinds of crystal growth.

B. Maxwell-Wagner (MW) analysis

For heterogeneous material, one can normally assume additivity in signal from different domains in the sample. However, for dielectric spectroscopy, this is in general not the case.[31] A difference in the conductivity of the different domains in the material leads to build-up of charges at the interfaces between domains. This gives rise to a polarization effect known as MW polarization.[20,32]

In the present case, the heterogeneity is caused by the formation of crystallites in the sample. As domains of crystal grow in the liquid, the dielectric constant for the composite will change. The details of the change will depend on the difference between the dielectric constant of the liquid (ϵ_l), and that of the crystal (ϵ_c), the shape of the crystal domain, and the volume fraction taken up by the crystal.

The two simplest cases of crystal domains growing in the liquid are that of a crystal layer growing from one (or both) of the electrodes, a heterogeneous nucleation picture, and the case of crystal spheres in a liquid matrix, a homogeneous nucleation picture.

In the first case, no approximation is involved in deriving the expression for the composite dielectric constant. The two materials (liquid and crystal) in a layered construction are simply modeled by two capacitors connected in series, $C_{\text{tot}} = (1/C_1 + 1/C_2)^{-1}$. Thus, the resulting composite dielectric constant is given by[31]

$$\epsilon_{\text{comp}} = \frac{d_c + d_l}{d_c/\epsilon_c + d_l/\epsilon_l} = \frac{\epsilon_c \epsilon_l}{(1-\phi_{\text{slab}})\epsilon_c + \phi_{\text{slab}}\epsilon_l}, \tag{2}$$

where $\phi_{\text{slab}} = d_c/(d_c + d_l)$ is the relative thickness of the crystal layer. Since ϵ_l and ϵ_c can be measured independently, this model has one free parameter (assuming the distance between the electrodes is fixed, or equivalently that total thickness of crystal and liquid layer is unchanged during crystallization).

Inserting the measured spectrum of ϵ_l (at time $t = 0$ before crystallization initiates) and ϵ_c (the spectrum of the fully crystallized sample), this model produces a shift in the peak frequency, but it overestimates the corresponding decrease in relaxation strength. Thus, the model is unable to capture the observed crystallization behavior; so, this scenario alone is not sufficient to explain what we observe.

In the case of crystal domains dispersed in a liquid, a mean-field approximation is used to arrive at the composite dielectric constant[33]

$$\epsilon_{\text{comp}} = \epsilon_l \frac{2\epsilon_l + \epsilon_c - 2\phi(\epsilon_l - \epsilon_c)}{2\epsilon_l + \epsilon_c + \phi(\epsilon_l - \epsilon_c)}, \tag{3}$$

where ϕ is the concentration of the crystal domains. This model also contains a single fitting parameter, ϕ. Inserting the measured spectra of ϵ_c and ϵ_l in Eq. (3) does not produce a frequency shift. Consequently, this model cannot account for what we observe either.

Instead, we propose to combine the two models such that a crystal layer is growing from the electrodes, while spherical crystallites are forming in the remaining liquid, see Fig. 4. This is modeled by combining Eqs. (2) and (3) such that ϵ_l in Eq. (2) is given by the composite dielectric constant from Eq. (3). This model has two parameters: the relative thickness of the crystal layer, ϕ_{slab}, and the concentration of crystal spheres in the liquid, ϕ.

The mean field approximation (Eq. (3)) is only accurate up to $\phi \approx 0.2$,[20] but we allow ϕ to go somewhat higher. Accuracy is lost when pushing the limits of the mean field approximation, but it could still give an indication of the overall behavior,

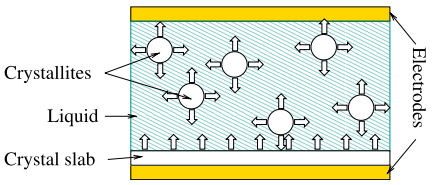

FIG. 4. Cartoon of the combined heterogeneous and homogeneous crystallization. The growth is indicated by the arrows.

especially when it is used in combination with Eq. (2), which is exact. In the combined model, the volume fraction of spheres in the total volume never gets close to 1 (see Fig. 5).

Examples of fits to isothermal crystallization spectra for cell A and cell B are shown in Figs. 5(a) and 5(b), respectively. The fits are focused on the Debye process by only fitting to the points within the two dotted lines. Having two fitting parameters gives sufficient flexibility to account for both the decrease in relaxation strength as well as the change in peak frequency of the Debye peak. However, the combined model does not adequately explain the behavior of the entire spectrum; it does not capture the behavior of the alpha and beta relaxation processes during the crystallization or the broadening of the Debye process. Despite these limitations, the models ability to describe the behavior of the Debye relaxation

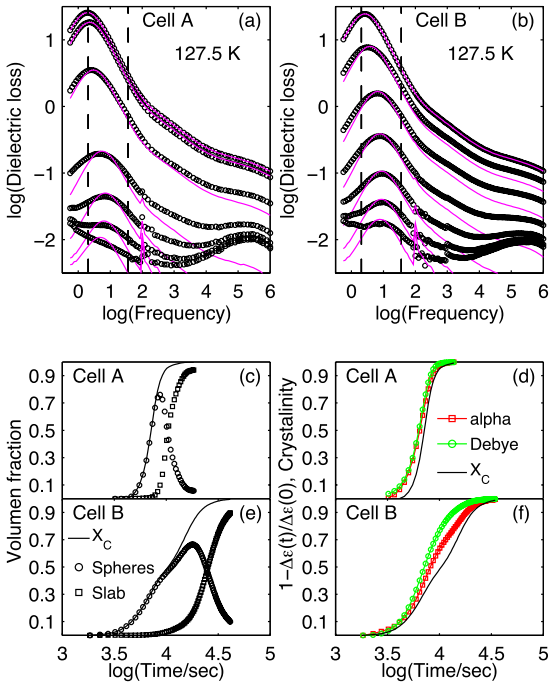

FIG. 5. The measurements shown in Fig. 2 analyzed using the Maxwell-Wagner (MW) approach described in Section III B. (a) and (b) show a selection of curves together with fits (magenta lines) for cell A (a) and cell B (b). The dashed vertical lines mark the frequency interval used for the fit. (c) and (e) show the volume fraction taken up by the spherical crystallites (circles) and the crystal slab (squares) as a function of time for cell A (c) and cell B (e). The solid line is the total crystal volume fraction. (d) and (f) Total crystal volume fraction from the MW fit (black line) as well as the normalized relaxation strength of the Debye process (in green) and alpha process (in red) as a function of time for cell A (d) and cell B (f).

strength and peak position may be used to shed some light on the observed phenomena.

The total crystallized volume fraction according to the model can be calculated as $X_c = (1 - \phi_{\text{slab}})\phi + \phi_{\text{slab}}$ and the volume fraction taken up by the spheres alone as $X_{\text{sphere}} = (1 - \phi_{\text{slab}})\phi$. Figures 5(c) and 5(e) show the volume fraction of the crystal layer and the spherical crystallites as well as the total crystal volume fraction. For both cells, it seems that the onset of crystallization is dominated by nucleation and growth of crystal spheres, and when a large fraction of the sample has crystallized ($X_c \sim 70\%$-80%), the slab growth takes over. However, the growth of crystal spheres starts earlier but proceeds at a slower rate in cell B compared to cell A. This difference in crystallization behavior in the two cells is reproduced at all temperatures (see Fig. 6).

The total degree of crystallinity as calculated from the MW fits is plotted together with the normalized Debye and alpha relaxation strengths for cell A in Fig. 5(d) and for cell B in Fig. 5(f). Again, the curves are clearly different for the two cells; in cell A, Debye and alpha relaxation strengths give almost identical curves that agree qualitatively with crystal fraction obtained in the MW fit, although the relaxation strength decreases faster than crystal fraction initially. In cell B, all three curves start out in the same way but separate later in the process, where both Debye and alpha relaxation strengths overestimate the degree of crystallinity. The MW crystallinity curve has a kink occurring approximately when there is a bump in the alpha relaxation strength, while this two-step behavior is not clearly seen in the Debye relaxation strength. The behavior of the crystallization process at 127.5 K and the MW analysis demonstrated in Fig. 5 are general for all the studied temperatures as can be seen in Fig. 6.

The proposed MW analysis qualitatively and quantitatively agrees with using the decrease of the alpha relaxation strength rather than the Debye relaxation strength as a measure of the crystallinity of the sample. However, neither reflect the fact that sample does not crystallize fully. This is because both the Debye and the alpha processes vanish during crystallization, while only the beta process survives. The analysis does not account for that, a fact that is already clear from the fits in Figs. 5(a) and 5(b).

C. Avrami analysis

Another independent — and more routinely used — way of evaluating the crystal growth is through the Johnson-Mehl-Avrami-Kolmogorov (JMAK) equation originally developed by Avrami.[34–36] In this analysis, the volume fraction taken

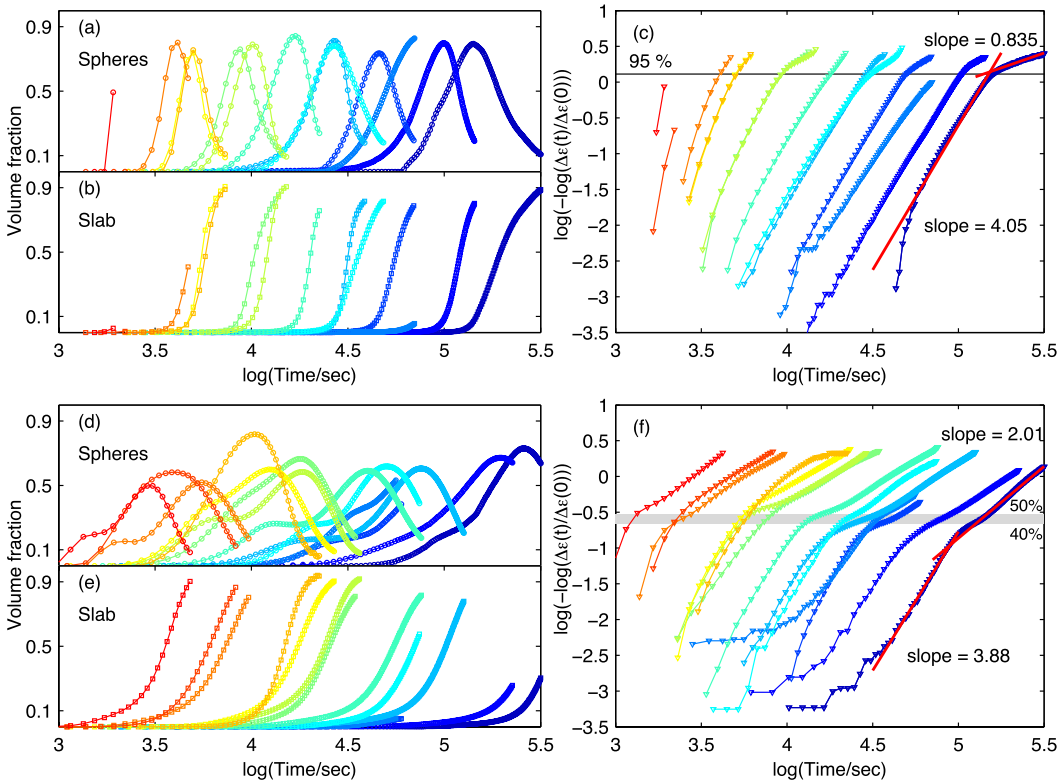

FIG. 6. Results from MW and Avrami analyses for all temperatures. (a), (b), (d), and (e) Volume fraction of crystal spheres (a) and (d) and volume fraction of a slab (b) and (d) based on the proposed combination of Eqs. (2) and (3). The differences for the two measuring cells outlined in Figs. 5(c) and 5(e) are general; cell A (a) and (b) display a single peak in the "sphere growth" and the "slab growth" set in early, while in cell B (d) and (e), there is a clear double peak in the "sphere growth." (c) and (f) show the JMAK plot which is a linearisation of the JMAK equation (Eq. (4) in the text). For both cells A (c) and B (f), the data clearly show a crossover from one linear behavior with a steep slope (~4) at short times to another linear behavior with a smaller slope (~1-2). But the transition from one to the other occurs at different crystallization degrees for the two cells: for cell A, the transition happens when the alpha relaxation strength has decayed more than 95% and for cell B, when $\Delta\epsilon(t)/\Delta\epsilon(0) \sim 40\%$-$50\%$ (marked by the gray bars in the figure).

up by crystallites, X_c is expressed in terms of a growth rate constant k, an induction time t_0, and the Avrami parameter n as follows:

$$X_c(t) = 1 - \exp\left[-k(t - t_0)^n\right] . \quad (4)$$

The value of n depends on the crystal morphology and crystallization mechanism, but it is not straightforward to interpret the meaning of this parameter. Originally, it was a number between 1 and 4 such that $n = d + r$ with d being the dimensionality of the growth and r being a number that represents the nucleation rate. For a constant nucleation rate, $r = 1$ and $r = 0$ if nucleation stops when the crystallization starts. More recently, n has been found to be a number between 1 and 7.[14,18]

When dielectric spectroscopy is used to study crystallization, the common practice is to assume that the alpha relaxation strength roughly corresponds to the degree of crystallinity, X_c, and then use that for the Avrami analysis. Since the MW model also gives some support for the alpha rather than the Debye relaxation strength is expressing the degree of crystallinity in the sample, we will adopt this approach.

One way to obtain an estimate of the parameter n is through the JMAK plot, which plots $\ln[-\ln(1 - X_c(t))]$ versus $\ln(t)$. This procedure avoids fitting Eq. (4) to data and n is directly obtained as the slope of the curve. The JMAK plots for cells A and B are shown in Fig. 6. In both cases, we see a transition from a relatively high value $n \approx 4$–5 to a low value $n \approx 1$–2. This observation suggests a change from higher dimensionality of growth to lower, which is consistent with the MW analysis indicating a change from spherical to slab growth. Moreover, the data suggest that this transition happens earlier in the crystallization process for cell B compared to cell A, which could explain why the crystallization slows down and takes much longer in cell B.

IV. DISCUSSION

Both the Debye and the alpha processes vanish during the crystallization, while the beta process survives. Thus, we confirm earlier findings that the crystallization process at temperatures near T_g stops before the sample is completely crystallized. Hedoux *et al.* report signs of an aborted or frustrated crystallization process, signaled by an amorphous halo persisting in the x-ray spectra.[25] This slow and frustrated crystallization process has also been interpreted as a polyamorph transformation between two meta-stable liquid phases.[27,37–39] Based on the dielectric spectra presented here, it is perhaps difficult to distinguish between the two scenarios, but the fact that the structural relaxation peaks disappear entirely combined with the emergence of Bragg peaks as documented in Ref. 25 point to a non-trivial crystallization process as the most obvious explanation for the observations.

It is however interesting that the aborted crystallization is seen in the dielectric spectra as the survival of the beta-process. If we envision the end product as a frustrated crystal, unable to tile space, then the liquid signal — in our case the beta relaxation — could originate from small pockets of liquids between crystal grains. This picture supports the idea of the beta relaxation being a local phenomenon, in favor of the "islands of mobility" suggested by Johari and co-workers.[40,41]

The mono-hydroxyl alcohols in general are interesting because of their anomalous (and usually intense) relaxation process at frequencies lower than the structural alpha relaxation — the so called Debye relaxation — which is believed to be due to supra-molecular hydrogen bonded structures in the liquid.[21,42] We observe that the Debye process vanishes faster than the alpha during crystallization, and that the alpha intensity seems to give a better measure for the degree of crystallinity. Sanz *et al.*[43] made similar observations for another monohydroxyl alcohol. They studied crystallization of isopropanol in real time by simultaneous dielectric spectroscopy and neutron diffraction measurements and thus had a direct measure of the degree of crystallinity that could be correlated with the relaxation strength of the Debye and alpha processes. They observed that the Debye intensity dropped rapidly at the onset of crystallization, while the alpha intensity followed the crystallization. Their intuitive and appealing interpretation was that the breakage of the hydrogen-bonded network is a precursor of the crystallization, and that the molecules leaving the network did not immediately go into a crystalline structure. The MW polarization effects lend itself to a different — macroscopic — interpretation of the observations. Irrespective of how the crystal growth is modeled in the MW framework, there cannot be proportionality between dielectric intensity and liquid fraction in the sample. The deviation from linearity depends on the specific model for the growth morphology and on the intensity of the process: the higher intensity, the stronger the deviation from linearity. Thus, the MW analysis provides a simple explanation for why the most intense process vanishes before the less intense one. The MW analysis does at the same account for the observed frequency shifts of the relaxation processes.

On the basis of MW fits, we suggested that the observed difference in crystallization behavior between the two cells could be rationalized by a transition from having primarily a growth of crystal spheres, a homogeneous nucleation and growth, to a growth of a crystal slab. This could be a slab growing from the electrodes but could also be a certain point in the process where crystal grains percolate and effectively create a crystal layer in the liquid-crystal mixture. The difference between the cells would then be explained by a difference in the degree of crystallization when this transition takes place. The idea that the crystal growth changes from a higher dimensional growth to a low dimensional growth was supported by the JMAK analysis that also points to such a transition taking place at different crystallization degrees in the two sample cells. The overall validity of JMAK equation (Eq. (4)) has been questioned, see, e.g., Refs. 44 and 45, and of course, we need to be cautious when making conclusions, based on the MW analysis where the limits of applicability of the mean-field approximations were pushed. But since both types of analyses point to this picture, we believe that the proposed conception of a change in morphology of the crystal growth is consistent and sound. It remains to be shown how general this behavior is. It would be interesting to apply this procedure to a simpler sample to study the influence of sample cell geometry on the crystallization process.

Irrespective of the generality of the particular behavior found here, our study shows that one needs to be very cautious about making detailed microscopic interpretations of the crystallization mechanisms based on dielectric spectroscopy alone, because MW polarization effects of the mixed phase require knowledge about the crystal growth morphology. In addition, we have also shown that the crystallization is extremely sensitive to the specific sample environment. Thus, it would require extensive investigations of different environments and perhaps even different probes to disentangle microscopic from macroscopic effects.

V. CONCLUSION

We have studied the isothermal crystallization process in the deeply supercooled region of the mono-alcohol *n*-butanol in real time at 15 different temperatures using dielectric spectroscopy. Two different sample cells have been used to look for the effects of the sample environment on the crystallization process. We found that the time evolution of the relaxation strengths differs for the two cells in a consistent and reproducible way for all temperatures.

On the basis of the Maxwell-Wagner analysis, we suggest that the crystallization behavior can be explained by a transition from primarily growth of crystal spheres to growth of a crystal layer. The difference between the cells in this framework is the difference in when in the crystallization process this transition takes place. This picture was supported by an Avrami–Mehl–Johnson–Kolmogorov analysis that also suggests a transition from higher dimensional growth to a lower one.

The Maxwell-Wagner analysis can also account for the shift in peak frequency observed for the Debye process during the course of crystallization, and thus, a microscopic interpretation of the peak shift is not needed. In general, our study shows that any microscopic interpretation of crystallization measurements requires multiple probes, sample environments, and careful protocols.

ACKNOWLEDGMENTS

Tina Hecksher is sponsored by DNRF Grant No. 61. The authors thank Ranko Richert for useful discussions and valuable comments.

[1]G. Tammann, J. Soc. Glass Technol. **9**, 166 (1925).
[2]W. Kauzmann, Chem. Rev. **43**, 219 (1948).
[3]P. G. Debenedetti, *Metastable Liquids : Concepts and Principles* (Princeton University Press, Princeton, NJ, 1996).
[4]R. Becker and W. Döring, Ann. Phys. **416**, 719 (1935).
[5]S. N. Bhat, A. Sharma, and S. V. Bhat, Phys. Rev. Lett. **95**, 235702 (2005).
[6]O. Mishima and H. E. Stanley, Nature **396**, 329 (1998).
[7]P. G. Debenedetti, J. Phys.: Condens. Matter **15**, R1669 (2003).
[8]H.-F. Yuan, T. Xia, M. Plazanet, B. Deme, and M. Orrit, J. Chem. Phys. **136**, 041102 (2012).
[9]J. Rabesiaka and A. J. Kovacs, J. Appl. Phys. **32**, 2314 (1961).
[10]S. Napolitano and M. Wübbenhorst, Macromolecules **39**, 5967 (2006).
[11]M. Massalska-Arodz, G. Williams, D. K. Thomas, W. J. Jones, and R. Dabrowski, J. Phys. Chem. B **103**, 4197 (1999).
[12]J. Alie, J. Menegotto, P. Cardon, H. Duplaa, A. Caron, C. Lacabanne, and M. Bauer, J. Pharm. Sci. **93**, 218 (2003).
[13]K. Adrjanowicz, K. Kaminski, Z. Wojnarowska, M. Dulski, L. Hawelek, S. Pawlus, M. Paluch, and W. Sawicki, J. Phys. Chem. B **114**, 6579 (2010).
[14]A. K. R. Dantuluri, A. Amin, V. Puri, and A. K. Bansal, Mol. Pharm. **8**, 814 (2011).
[15]K. Kothari, V. Ragoonanan, and R. Suryanarayanan, Mol. Pharm. **11**, 3048 (2014).
[16]J. Sibik, M. J. Sargent, M. Franklin, and J. A. Zeitler, Mol. Pharm. **11**, 1326 (2014).
[17]T. A. Ezquerra, J. Majszczyk, F. J. Balta-Calleja, L.-C. E., K. H. Gardner, and B. S. Hsiao, Phys. Rev. B **50**, 6023 (1994).
[18]M. T. Viciosa, N. T. Correia, M. S. Sanchez, A. L. Carvalho, M. J. Romão, J. L. Gómez Ribelles, and M. Dionísio, J. Phys. Chem. B **113**, 14209 (2009).
[19]K. Adrjanowicz, A. Grzybowski, K. Grzybowska, J. Pionteck, and M. Paluch, Cryst. Growth Des. **14**, 2097 (2014).
[20]*Broadband Dielectric Spectroscopy*, edited by F. Kremer (Springer Science & Business Media, 2003).
[21]R. Böhmer, C. Gainaru, and R. Richert, Phys. Rep. **545**, 125 (2014).
[22]I. M. Shmyt'ko, R. J. Jiménez-Rioboó, M. Hassaine, and M. A. Ramos, J. Phys.: Condens. Matter **22**, 195102 (2010).
[23]P. Derollez, A. Hedoux, Y. Guinet, F. Danede, and L. Paccou, Acta Crystallogr., Sect. B: Struct. Sci., Cryst. Eng. Mater. **69**, 195 (2013).
[24]A. Wypych, Y. Guinet, and A. Hedoux, Phys. Rev. B **76**, 144202 (2007).
[25]A. Hedoux, Y. Guinet, L. Paccou, P. Derollez, and F. Danede, J. Chem. Phys. **138**, 214506 (2013).
[26]M. Hassaine and M. A. Ramos, Phys. Status Solidi A **208**, 2245 (2011).
[27]R. Kurita and H. Tanaka, J. Phys.: Condens. Matter **17**, L293 (2005).
[28]B. Igarashi, T. Christensen, E. H. Larsen, N. B. Olsen, I. H. Pedersen, T. Rasmussen, and J. C. Dyre, Rev. Sci. Instrum. **79**, 045105 (2008).
[29]N. Saglanmak, A. I. Nielsen, N. B. Olsen, J. C. Dyre, and K. Niss, J. Chem. Phys. **132**, 024503 (2010).
[30]A. I. Nielsen, B. Jakobsen, K. Niss, N. B. Olsen, R. Richert, and J. C. Dyre, J. Chem. Phys. **130**, 154508 (2009).
[31]R. Richert, Eur. Phys. J.: Spec. Top. **189**, 37 (2010).
[32]J. Schüller, R. Richert, and E. W. Fischer, Phys. Rev. B **52**, 15232 (1995).
[33]K. W. Wagner, Arch. Elektrotech. **8**, 371 (1914).
[34]M. Avrami, J. Chem. Phys. **7**, 1103 (1939).
[35]M. Avrami, J. Chem. Phys. **8**, 212 (1940).
[36]M. Avrami, J. Chem. Phys. **9**, 177 (1941).
[37]A. G. Dzhonson and B. V. Bol'shakov, Dokl. Phys. Chem. **393**, 318 (2003).
[38]B. V. Bol'shakov and A. G. Dzhonson, J. Non-Cryst. Solids **351**, 444 (2005).
[39]B. Zgardzinska, M. Paluch, and T. Goworek, Chem. Phys. Lett. **491**, 160 (2010).
[40]G. P. Johari and M. Goldstein, J. Chem. Phys. **53**, 2372 (1970).
[41]G. P. Johari, J. Non-Cryst. Solids **307-310**, 317 (2002).
[42]C. Gainaru, R. Figuli, T. Hecksher, B. Jakobsen, J. C. Dyre, and M. A. B. Wilhelm, Phys. Rev. Lett. **112**, 098301 (2014).
[43]A. Sanz, M. Jiménez-Ruiz, A. Nogales, D. Martín y Marero, and T. A. Ezquerra, Phys. Rev. Lett. **93**, 015503 (2004).
[44]M. T. Todinov, Acta Mater. **48**, 4217 (2000).
[45]M. Fanfoni and M. Tomellini, Il Nuovo Cimento D **20**, 1171 (1998).

Bibliography

[1] *Physical Properties of Glycerine and Its Solutions*. Glycerine Producers' Association, November 1963.

[2] K Adrjanowicz, B Jakobsen, T Hecksher, K Kaminski, M Dulski, M Paluch, and K Niss. Communication: Slow supramolecular mode in amine and thiol derivatives of 2-ethyl-1-hexanol revealed by combined dielectric and shear-mechanical studies. *The Journal of Chemical Physics*, 143(18):181102–6, November 2015.

[3] H Alice, I Cohen, X Zhao, M Lee, and D Kicelson. Supercooled Liquids and Polyamorphism. *The Journal of Chemical Physics*, 100, January 1996.

[4] Katrin Amann-Winkel, R Böhmer, Franz Fujara, C Gainaru, Burkhard Geil, and Thomas Loerting. Colloquium: Water's controversial glass transitions. *Reviews of Modern Physics*, 88(1):011002–20, February 2016.

[5] C A Angell. Insights into Phases of Liquid Water from Study of Its Unusual Glass-Forming Properties. *Science*, 319(5863):582–587, February 2008.

[6] Melvin Avrami. Kinetics of Phase Change. I. General Theory. *The Journal of Chemical Physics*, 7(12):1103, 1939.

[7] Melvin Avrami. Kinetics of Phase Change. II. Transformation-Time Relations for Random Distribution of Nuclei. *The Journal of Chemical Physics*, 8(2):212, 1940.

[8] Melvin Avrami. Granulation, Phase Change, and Microstructure Kinetics of Phase Change. III. *The Journal of Chemical Physics*, 9(2):177, 1941.

[9] I Avramov, K Avramova, and C Rüssel. New method to analyze data on overall crystallization kinetics. *Journal of Crystal Growth*, 285(3):394–399, December 2005.

[10] Johannes Bachler, Violeta Fuentes-Landete, David A Jahn, Jessina Wong, Nicolas Giovambattista, and Thomas Loerting. Glass polymorphism in glycero-;water mixtures: II. Experimental studies. *Physical Chemistry Chemical Physics*, 18:11058–11068, April 2016.

[11] S Bauer, K Burlafinger, C Gainaru, P Lunkenheimer, W Hiller, A Loidl, and R Böhmer. Debye relaxation and 250 K anomaly in glass forming

monohydroxy alcohols. *The Journal of Chemical Physics*, 138(9):094505, 2013.

[12] S Bauer, H Wittkamp, S Schildmann, M Frey, W Hiller, T Hecksher, N B Olsen, C Gainaru, and R Böhmer. Broadband dynamics in neat 4-methyl-3-heptanol and in mixtures with 2-ethyl-1-hexanol. *The Journal of Chemical Physics*, 139(13):134503, 2013.

[13] F J Bermejo, F J Mompeán, M García-Hernández, J L Martínez, D Martin-Marero, A Chahid, G Senger, and M L Ristig. Collective excitations in liquid deuterium: Neutron-scattering and correlated-density-matrix results. *Physical Review B*, 47:15097–15112, June 1993.

[14] Thorsten Bertels-Rausch and Nevin Uras-Aytemiz. Ice structures, pattern, and processes: A view across the ice fields. *arXiv.org*, pages 1–62, July 2012.

[15] R Böhmer, C Gainaru, and Ranko Richert. Structure and dynamics of monohydroxy alcohols. *Physics Reports*, 545(4):125–195, December 2014.

[16] Frédéric Caupin. Escaping the no man's land: Recent experiments on metastable liquid water. *Journal of Non-Crystalline Solids*, 407(C):441–448, November 2014.

[17] T Christensen and N B Olsen. A rheometer for the measurement of a high shear modulus covering more than seven decades of frequency below 50 kHz. *Review of Scientific Instruments*, 66:5019–5031, May 1995.

[18] J R D Copley and J M Rowe. Density fluctuations in liquid rubidium. I. Neutron-scattering measurements. *physical review A*, 9:1656–1666, April 1974.

[19] G J Cuello, V Cristiglio, M A González, and C Cabrillo. Structure factor of liquid n-butanol at room temperature. *Journal of Physics: Conference Series*, 549(1):012015, November 2014.

[20] P G De Gennes. Liquid Dynamics and inelastic scattering of neutrons. *Physica*, 25:825–839, January 1959.

[21] P Derollez, A Hedoux, Y Guinet, F Danede, and L Paccou. Structure determination of the crystalline phase of-butanol by powder X-ray diffraction and study of intermolecular associations by Raman spectroscopy. *Acta Cryst (2013). B69, 195-202 [doi:10.1107/S2052519213004843]*, 69(2):1–8, March 2013.

[22] M Descamps, V Legrand, Y Guinet, A Amanzzal, C Alba, and J Dore. "Pre-Peak" in the structure Factor of Simple Molecular Glass Formers. *Progress of Theoretical Physics Supplement*, pages 207–212, January 1997.

[23] A G Dzhonson and B V Bol'shakov. On the Number of Amorphous Phases in n-Butanol. *Chemical Physics*, pages 1–3, November 2003.

[24] J T Edward. Molecular Volumes and the Stokes-Einstein Equation. *Journal of Chemical Education*, 47:261–270, April 1970.

[25] Andrei V Egorov, Alexander P Lyubartsev, and Aatto Laaksonen. Molecular Dynamics Simulation Study of Glycerol–Water Liquid Mixtures. *The Journal of Physical Chemistry B*, 115(49):14572–14581, December 2011.

[26] Gennadiy I Egorov, Dmitriy M Makarov, and Arkadiy M Kolker. Volume properties of liquid mixture of water+glycerol over the temperature range from 278.15 to 348.15K at atmospheric pressure. *Thermochimica Acta*, 570:16–26, October 2013.

[27] E P Favvas and A C Mitropoulos. What is spinodal decomposition. pages 25–27, June 2008.

[28] B Frick, J Combet, and L van Eijck. New possibilities with inelastic fixed window scans and linear motor Doppler drives on high resolution neutron backscattering spectrometers. *Nuclear Inst. and Methods in Physics Research, A*, 669(C):7–13, March 2012.

[29] C Gainaru, R Figuli, T Hecksher, B Jakobsen, J C Dyre, M Wilhelm, and R Böhmer. Shear-Modulus Investigations of Monohydroxy Alcohols: Evidence for a Short-Chain-Polymer Rheological Response. *Physical Review Letters*, 112(9):098301, March 2014.

[30] C Gainaru, R Meier, S Schildmann, C Lederle, W Hiller, E A Rössler, and R Böhmer. Nuclear-Magnetic-Resonance Measurements Reveal the Origin of the Debye Process in Monohydroxy Alcohols. *Physical Review Letters*, 105(25):258303, December 2010.

[31] C Gainaru, M Wikarek, S Pawlus, M Paluch, R Figuli, M Wilhelm, T Hecksher, B Jakobsen, J C Dyre, and R Böhmer. Oscillatory shear and high-pressure dielectric study of 5-methyl-3-heptanol. *Colloid and Polymer Science*, 292(8):1913–1921, June 2014.

[32] David J Griffiths. *Introduction to Electrodynamics*. Addison-Wesley Professional, 3rd edition, December 1989.

[33] Yoshihito Hayashi, Alexander Puzenko, Igal Balin, Yaroslav E Ryabov, and Yuri Feldman. Relaxation Dynamics in GlycerolWater Mixtures. 2. Mesoscopic Feature in Water Rich Mixtures. *The Journal of Physical Chemistry B*, 109(18):9174–9177, May 2005.

[34] T Hecksher. *Relaxation in Supercooled Liquids*. PhD thesis, May 2011.

[35] Tina Hecksher and Jeppe C Dyre. A review of experiments testing the shoving model. *Journal of Non-Crystalline Solids*, 407(C):14–22, January 2015.

[36] Alain Hédoux, Yannick Guinet, L Paccou, P Derollez, and F Danede. Vibrational and structural properties of amorphous n-butanol: A complementary Raman spectroscopy and X-ray diffraction study. *The Journal of Chemical Physics*, 138(21):214506, 2013.

[37] Brian Igarashi, Tage Christensen, Ebbe H Larsen, Niels Boye Olsen, Ib H Pedersen, Torben Rasmussen, and Jeppe C Dyre. A cryostat and temperature control system optimized for measuring relaxations of glass-forming liquids. *Review of Scientific Instruments*, 79(4):045105, 2008.

[38] B Jakobsen, K Niss, Claudio Maggi, N B Olsen, T Christensen, and J C Dyre. Beta relaxation in the shear mechanics of equilibrium viscous liquids: Phenomenology and network modeling of the alpha-beta merging region. *arXiv.org*, pages 1–8, May 2010.

[39] Bo Jakobsen, Tina Hecksher, Tage Christensen, Niels Boye Olsen, Jeppe C Dyre, and Kristine Niss. Communication: Identical temperature dependence of the time scales of several linear-response functions of two glass-forming liquids. *The Journal of Chemical Physics*, 136(8):081102, 2012.

[40] Bo Jakobsen, Alejandro Sanz, Kristine Niss, Tina Hecksher, Ib H Pedersen, Torben Rasmussen, Tage Christensen, Niels Boye Olsen, and Jeppe C Dyre. Thermalization calorimetry: A simple method for investigating glass transition and crystallization of supercooled liquids. *AIP Advances*, 6(5):055019–16, May 2016.

[41] Ken F Kenton and A L Greer. *Nucleation in Condensed Matter*, volume 15 of *Applications in Materials and Biology*. 1 edition, March 2010.

[42] Friedrich Kremer and Andreas Schönhals, editors. *Broadband Dielectric Spectroscopy*. Springer Berlin Heidelberg, Berlin, Heidelberg, 2003.

[43] Rei Kurita. Critical-like phenomena associated with liquid-liquid transition in a molecular liquid. *Science*, 306(5697):845–848, October 2004.

[44] Rei Kurita. On the abundance and general nature of the liquid–liquid phase transition in molecular systems. *Journal of Physics: Condensed Matter*, 17(27):L293–L302, June 2005.

[45] Rei Kurita and Hiroshi Mataki. Liquid-Liquid Transition in the Molecular Liquid Triphenyl Phosphite. *Physical Review Letters*, 92(2):025701, January 2004.

[46] Ruep E Lechner and Stéphane Longeville. Quasielastic Neutron Scattering in Biology Part I: Methods. pages 1–47, June 2005.

[47] C. Lederle, W Hiller, C Gainaru, and R Böhmer. Diluting the hydrogen bonds in viscous solutions of n-butanol with n-bromobutane: II. A comparison of rotational and translational motions. *The Journal of Chemical Physics*, 134(6):064512, 2011.

[48] David T Limmer and David Chandler. The putative liquid-liquid transition is a liquid-solid transition in atomistic models of water. *The Journal of Chemical Physics*, 135(13):134503, 2011.

[49] David T Limmer and David Chandler. The putative liquid-liquid transition is a liquid-solid transition in atomistic models of water. II. *The Journal of Chemical Physics*, 138(21):214504, 2013.

[50] Thomas Loerting and Nicolas Giovambattista. Amorphous ices: experiments and numerical simulations. *Journal of Physics: Condensed Matter*, 18(50):R919–R977, November 2006.

[51] Thomas Loerting, Katrin Winkel, Markus Seidl, Marion Bauer, Christian Mitterdorfer, Philip H Handle, Christoph G Salzmann, Erwin Mayer, John L Finney, and Daniel T Bowron. How many amorphous ices are there? *Physical Chemistry Chemical Physics*, 13(19):8783–12, 2011.

[52] R Meier, D Kruk, J Gmeiner, and E A Rössler. Intermolecular relaxation in glycerol as revealed by field cycling 1H NMR relaxometry dilution experiments. *The Journal of Chemical Physics*, 136(3):034508–9, 2012.

[53] F Mezei. Neutron Spin Echo: A New Concept in Polarized Thermal Neutron Techniques. *Z. Physik*, 255:146–160, February 1972.

[54] F Mezei, W Knaak, and B Fargo. Neutron Spin Echo Study of Dynamic Correlations Near Liquid-Glass Transition. *Physica Scripta*, T19(3):363–368, January 1987.

[55] Anoma Mudalige and Jeanne E Pemberton. Raman spectroscopy of glycerol/D2O solutions. *Vibrational Spectroscopy*, 45(1):27–35, October 2007.

[56] Ken-ichiro Murata and Hajime Tanaka. Liquid–liquid transition without macroscopic phase separation in a water–glycerol mixture. *Nature Materials*, 11(5):436–443, March 2012.

[57] Y M NAZIEV, Shakhverdiev A N, T S Abdullaev, and G R Mekhtieva. Viscosity of normal-butanol at low-temperatures and various pressures. *JOURNAL OF APPLIED CHEMISTRY OF THE USSR*, 64(7):1443–1443, July 1991.

[58] Albena I Nielsen, Tage Christensen, Bo Jakobsen, Kristine Niss, Niels Boye Olsen, Ranko Richert, and Jeppe C Dyre. Prevalence of approximate t relaxation for the dielectric α process in viscous organic liquids. *The Journal of Chemical Physics*, 130(15):154508–16, 2009.

[59] K Niss and Bo Jakobsen. *Dielectric and Shear Mechanical Relaxation in Glass Forming Liquids*. PhD thesis, September 2003.

[60] Ulf R Pedersen, Felix Hummel, and Christoph Dellago. Computing the crystal growth rate by the interface pinning method. *The Journal of Chemical Physics*, 142(4):044104–10, January 2015.

[61] Robert Piccirelli. Ultrasonic Shear and Compressional Relaxation in Liquid Glycerol. *The Journal of the Acoustical Society of America*, 29(9):1009–13, 1957.

[62] Peter H Poole, Richard K Bowles, Ivan Saika-Voivod, and Francesco Sciortino. Free energy surface of ST2 water near the liquid-liquid phase transition. *The Journal of Chemical Physics*, 138(3):034505, 2013.

[63] Peter H Poole, Francesco Sciortino, Ulrich Essmann, and H Eugene Stanley. Phase behaviour of metastable water. *Nature*, 360:324–328, January 1992.

[64] Ivan Popov, Anna Greenbaum Gutina, Alexei P Sokolov, and Yuri Feldman. The puzzling first-order phase transition in water-glycerol mixtures. *Physical Chemistry Chemical Physics*, 17(27):1–9, June 2015.

[65] Alexander Puzenko, Yoshihito Hayashi, Yaroslav E Ryabov, Igal Balin, Yuri Feldman, Udo Kaatze, and Ralph Behrends. Relaxation Dynamics in GlycerolWater Mixtures: I. Glycerol-Rich Mixtures. *The Journal of Physical Chemistry B*, 109(12):6031–6035, March 2005.

[66] A Sanz, M Jiménez-Ruiz, A Nogales, D Martín y Marero, and T A Ezquerra. Hydrogen-Bond Network Breakage as a First Step to Isopropanol Crystallization. *Physical Review Letters*, 93(1):015503–4, July 2004.

[67] A Sanz and K Niss. Liquid dynamics in partially crystalline glycerol. *arXiv.org*, pages 1–9, October 2016.

[68] Filippo Scarponi, Lucia Comez, Daniele Fioretto, and Luciano Palmieri. Brillouin light scattering from transverse and longitudinal acoustic waves in glycerol. *Physical Review B*, 70(5):054203–7, August 2004.

[69] U Schneider, P Lunkenheimer, R Brand, and A Loidl. Dielectric and far-infrared spectroscopy of glycerol. *Journal of Non-Crystalline Solids*, pages 173–179, July 1998.

[70] K Schröter and E Donth. Viscosity and shear response at the dynamic glass transition of glycerol. *The Journal of Chemical Physics*, 113(20):9101–9, 2000.

[71] K Schröter, S A Hutcheson, X Shi, A Mandanici, and G B McKenna. Dynamic shear modulus of glycerol: Corrections due to instrument compliance. *The Journal of Chemical Physics*, 125(21):214507–5, 2006.

[72] J E Shelby. *Introduction to Glass Science and Technology*. Royal Society of Chemistry, Cambridge, 2 edition, 2005.

[73] I M Shmyt'ko, R J Jiménez-Riobóo, M Hassaine, and M A Ramos. Structural and thermodynamic studies of n-butanol. *Journal of Physics: Condensed Matter*, 22(19):195102–10, April 2010.

[74] R W Sillars. The properties of a dielectric containing semi-conducting particles of various shapes. *The journal of the Institution of Electrical Engineers*, 12(35):139–155, November 1937.

[75] Per Sillrén, A Matic, M Karlsson, M Koza, M Maccarini, P Fouquet, M Götz, Th Bauer, R Gulich, P Lunkenheimer, A Loidl, J Mattsson, C Gainaru, E Vynokur, S Schildmann, S Bauer, and R Böhmer. Liquid 1-propanol studied by neutron scattering, near-infrared, and dielectric spectroscopy. *The Journal of Chemical Physics*, 140(12):124501, March 2014.

[76] Lokendra P Singh and Ranko Richert. Watching Hydrogen-Bonded Structures in an Alcohol Convert from Rings to Chains. *Physical Review Letters*, 109(16):167802, October 2012.

[77] S K Sinha, E B Sirota, S Garofl, and H B Stanley. X-ray and neutron scattering from rough surfaces. *Physical Review B*, 38:2297–2311, August 1988.

[78] K Sköld, J M Rowe, and G Ostrowski. Coherent- and Incoherent-Scatting Laws of Liquid Argon. *physical review A*, 6:1107–1131, September 1972.

[79] O Söderström, U Dahlborg, and M Davidovic. Dynamic scattering function for high-temperature liquid lead. *physical review A*, 27:470–477, January 1983.

[80] S Sudo, M Shimomura, N Shinyashiki, and S Yagihara. Broadband dielectric study of a–b separation for supercooled glycerol–water mixtures. *Journal of Non-Crystalline Solids*, pages 356–363, August 2002.

[81] Yoshiharu Suzuki and Osamu Mishima. Experimentally proven liquid-liquid critical point of dilute glycerol-water solution at 150 K. *The Journal of Chemical Physics*, 141(9):094505–8, September 2014.

[82] A Tölle, J Wuttke, Helmut Schober, O G Randl, and F Fujara. Wavenumber dependence of structural α relaxation in a molecular liquid. *The European Physical Journal B*, 5:231–236, September 1998.

[83] J J Towey and L Dougan. Structural Examination of the Impact of Glycerol on Water Structure. *The Journal of Physical Chemistry B*, 116(5):1633–1641, February 2012.

[84] J J Towey, A K Soper, and L Dougan. Preference for Isolated Water Molecules in a Concentrated Glycerol–Water Mixture. *The Journal of Physical Chemistry B*, 115(24):7799–7807, June 2011.

[85] J J Towey, A K Soper, and L Dougan. The structure of glycerol in the liquid state: a neutron diffraction study. *Physical Chemistry Chemical Physics*, 13(20):9397–10, 2011.

[86] J J Towey, A K Soper, and L Dougan. Molecular Insight Into the Hydrogen Bonding and Micro-Segregation of a Cryoprotectant Molecule. *The Journal of Physical Chemistry B*, 116(47):13898–13904, November 2012.

[87] Kaarlo Sakari Vahvaselkä, Ritva Serimaa, and Mika Torkkeli. Determination of liquid structures of the primary alcohols methanol, ethanol, 1-propanol, 1-butanol and 1-octanol by x-ray scattering. *Journal of Applied Crystallography*, 28:189–195, March 1994.

[88] A A van Well and L A de Graaf. Density fluctuations in liquid argon. II. Coherent dynamic structure factor at large weve numbers. *physical review A*, 32:2384–2395, April 1985.

[89] A A van Well, P Verkerk, L A de Graaf, J B Suck, and J R D Copley. Density fluctuations in liquid argon: Coherent dynamic structure factor along the 120-K isotherm obtained by neutron scattering. *physical review A*, 31:3391–3414, April 1985.

[90] Karl Willy Wagner. Erklärung der dielektrischen Nachwirkungsvorgange auf Grund Maxwellscher Vorstellungen. *Archiv für Elektrotechnik*, 2:371, January 1914.

[91] Aleksandra Wypych, Yannick Guinet, and Alain Hédoux. Isothermal transformation of supercooled liquid n-butanol near the glass transition: Polyamorphic transitions in molecular liquids investigated using Raman scattering. *Physical Review B*, 76(14):144202, October 2007.

[92] Ekaterina A Zheligovskaya and Georgii G Malenkov. Crystalline water ices. *Russian Chemical Reviews*, 75(1):57–76, October 2007.